UNIVERSITY OF LIVERPOOL

Porous Titanium Structures Manufactured by Selective Laser Melting for Heat Pipe Applications

Thesis submitted in accordance with the requirements of the University of Liverpool for the Degree of Doctor in Philosophy

by

Zhining Wu

March 2020

Abstract

A heat pipe is an excellent heat transfer device that can be used in many applications such as space, terrestrial industries and electronic and energy conservation. The selection of used metal and working fluid varies depending on the operating environment. The appropriate wick structure used can make it work in any orientations even against gravity. However, conventional manufacturing processes have difficulty in producing heat pipe with complex shape and controllable wick structure, and the capillary lift height is limited for the current types of the wick structure if the against-gravity operating situation is necessary. In this study, Selective Laser Melting (SLM) is used to manufacture full-length heat pipes used in a space application with the wick structure designed and developed by the University of Liverpool based on a unit cell approach. The results show that the SLM process is capable of producing heat pipes with considerable length and the designed octahedral unit cells can provide sufficient capillary force and permeability to make the heat pipe work in space applications. In addition, the relationship between the fluid and thermal properties and characteristics (unit cell size, porosity, and pore size) have been investigated to understand the principle of the heat pipe better. Commercially pure titanium grade 2 (CpTi) and Ti-6Al-4V (Ti64) are used as the materials because their excellent machining properties and lightweight are suitable for space application. The capillary lift height is measured using a weight-change method and a height-change method simultaneously to get a more accurate result. The findings of this study indicate that the fluid and thermal performances of the heat pipe are highly dependent on the morphology of the porous structure and the porous structures manufactured by the SLM process can provide bigger capillary force compared with other typical porous structures used in heat pipes.

Contents

List of Figures

List of Tables

Glossary

3DP	3D printing
AM	Additive manufacturing
CAD	Computer aided design
CpTi	Commercially pure titanium
DMD	Direct metal deposition
EBM	Electron beam melting
FDM	Fused deposition modelling
IR	Infrared
LENS	Laser engineering net shaping
LMD	Laser metal deposition
LOM	Laminated object manufacturing
NCG	Non-condensable gas
SEM	Scanning electron microscopy
SL	Stereolithography
SLM	Selective laser melting
SLS	Selective laser sintering
Ti64	Ti-6Al-4V
VED	Volumetric Laser Energy Density

Nomenclatures

A	Cross sectional area	m^2
A_r	Relative area	-
C	Form drag coefficient	m^{-1}
D	Diameter	mm
d	Pore size	µm
d_a	Average pore diameter	µm
E_ρ	Laser energy density	J/mm^2
g	Gravitational acceleration	m/s^2
H	Mean curvature	1/mm
h	Height	mm
K	Permeability	m^2
M	Mass	g
P	Laser power	W
q	Flux	L/min
Q	Heat flux	W/m^2
r	Radius	mm
s	Strut thickness	µm
T	Temperature	°C
t	Laser exposure time	µs
U	Unit cell size	µm
V	Volume	cm^3
v	velocity	m/s

ΔP/Δx	Pressure drop along the flow direction	Pa/m
θ	Contact angle	°
Ɣ	Surface tension	N/m
φ	Porosity	-
μ	Viscosity	Pa.s
ρ	Density	g/cm^3
δ	Volume fraction of solid	-

Chapter 1

Introduction

A heat pipe is a specific heat exchanger, the concept of which was first suggested by Gaugler in 1942. It is used as a heat transfer device in many applications, such as CPU cooling, high power electronics cooling, and spaceship thermal management. It has excellent thermal properties due to the conduction of the metal material and the phase transition of the working fluid in the pipe. Different geometries, such as cylindrical heat pipes and loop heat pipes, can be designed or assembled for various applications. The selection of material and working fluid is flexible, depending on the operation temperature and compatibility. It is possible to construct heat pipes for use at temperatures ranging from 4 K to over 2300 K (Reay et al., 2013).

Compared with thermosyphon, which is a “simplified” heat pipe using gravity to make the fluid circulate into the chamber, heat pipe can work against gravity because the wick structure inside the pipe can provide sufficient capillary force to pump the fluid from the bottom. The capillary force makes heat pipe possible to be used where the heat source is higher than the condenser part. The achievable lift height, which is driven by capillary force, usually increases when the pore size of the wick structure decreases, and the ability to conduct large heat fluxes usually increases when the porosity increases. Therefore, it becomes essential to find out the optimum wick structure that can balance the capillary force and the corresponding fluid and thermal properties.

There are three typical categories of traditional wick in heat pipes: sintered metal powder, screen mesh, and grooved wick. Generally, mesh and grooved wick heat pipes

are only used if the hot spot is below the cold section as the capillary force that can be applied by the structure cannot maintain effective function against gravity. The structure of a sintered wick heat pipe can efficiently handle higher heat densities than the others and can work in all orientations, including against gravity because of the increased capillary force provided by the small pore size.

Recently, greater emphasis has been placed on manufacturing porous structures with controllable porosity and pore size and with varying geometries tailored for different applications. The conventional manufacturing methods can manufacture heat pipes with simply flat or cylindrical geometries. It is almost impossible to manufacture a complex geometry heat pipe with a wick structure at the same time.

Selective Laser Melting (SLM), which is a method of Additive Manufacturing (AM), is proposed as a solution. A novel porous structure created and developed by the University of Liverpool for orthopaedic applications is used as a potential wick structure in heat pipe applications in this work. Based on the defined 'unit cell size' approach, an octahedral porous structure with high pore interconnectivity is generated. Commercially pure titanium (CpTi) and Ti-6Al-4V (Ti64) are chosen to be the materials because of their excellent mechanical properties, high strength-to-weight ratio, and compatibility with many working fluids in a heat pipe. Densities of solid part approaching 100% are already achievable for both powder types. This is very important for the solid wall of a heat pipe because the vapour pressure can change rapidly due to the phase transition of the working fluid, which may crack the pipe during operation.

This study is associated with a project proposed by the European Space Agency to design and manufacture specialised heat pipes on telecommunications satellites. The heat pipes are to be deployed vertically within the chassis to reduce the thermal

resistance of the chassis wall and enhance the cooling performance of the electronics box. Although there is no gravity in space, the heat pipes are still required to function in the ground test of the satellite, both aiding and against gravity. The specification of heat pipes is defined by the dimensions of a typical electronics box, which has a height of approximately 200 mm. Conventional wick structures failed to pass the ground test against gravity because they either cannot provide sufficient capillary pressure to support the head of working fluid or are unsuccessful in producing parts with a sufficient length of about 200 mm with controllable porosity and pore size.

The main requirements for wick structures manufactured by SLM for the project are:

(1) lift height of 200 mm against gravity.

(2) high permeability in the range of 10^{-10} to 10^{-12} m^2.

Based on the above requirements, this study aims to develop, design and manufacture appropriate porous structures using the SLM method, which can be used as wick structures in heat pipes with low freezing temperature working against gravity, especially for use on telecommunications satellites. In order to achieve this aim, several objectives are developed as follows:

(1) To investigate the relationships between the laser parameters and laser strategies and the porosity and pore size of the as-manufactured porous structures.

(2) To investigate the permeability and capillary force of each structure, the specific performance per unit mass, and their relationships with the characteristics of the porous structures.

(3) To investigate the heat transfer performance of each structure and its relationship with characteristics of the porous structures.

(4) To develop prototypes of heat pipes that can satisfy all the requirements in the project, in collaboration with Aavid Thermacore (Aavid, USA).

An appropriate SLM manufacturing process needs to be developed since a small pore size may require a different laser energy input, which may cause insufficient fusion of the metal powder. It is essential to find out a right balance between the characteristics of the porous structure and the quality of the struts. This thesis investigates the metallic porous structures made by SLM and the relationships between the fluid, especially the capillary action, and thermal properties and the characteristics of the porous structures. There are eight chapters in this thesis. Chapter 1 gives a general description of the background and the significance of this study. Chapter 2 is about the literature related to this study, including the background about heat pipes, laser powder interaction and the relevant theories about fluid and thermal properties of porous structures. Chapter 3 presents a detailed description of the way the study was conducted, including measurements of porosity, pore size, permeability, lift capillary height and heat transfer coefficient. Chapter 4 presents the relationship between the characteristics of the generated porous structures and the laser parameters used in the manufacturing process. Porosity and pore size results for both CpTi and Ti64 are given as well. The laser powder interaction and the different qualities of struts caused by varying manufacturing strategies are discussed. Chapter 5 shows the results of permeability, lift capillary height and heat transfer coefficient measurements. The factors that can have a significant influence on these properties are discussed. Chapter 6 presents the design and development of full-length heat pipes, followed by the compatibility and thermal test results of the charged heat pipes. Chapter 7 gives the major findings in this study and makes suggestions for future research.

Chapter 2

Literature Review

This chapter provides the background for the research area relevant to this study. Firstly, a brief history of the heat pipe is given, followed by an introduction of the wick structures and different combinations of wall materials and working fluids in varying operation situations. Secondly, the SLM and its process parameters which can affect the quality of the manufactured parts are introduced. Finally, the relevant knowledge about fluid and thermal properties of porous structures is presented.

2.1 Heat Pipe

A heat pipe is usually used as a heat-transfer device that combines the principles of both thermal conduction and phase transition. It can be used to transfer heat over distances and its effective thermal conductivity can be very high compared with the conventional metal heat conductors. The relatively low-cost and straightforward manufacturing process also make it a remarkable mode of heat transfer (Chi, 1976). The concept of the heat pipe was first suggested by Gaugler in 1942, in the US Patent No. 2350348 and the heat pipe was applied to a refrigeration system with crushed ice and melted water as the working fluid (Gaugler, 1944). At the time, the heat pipe was also called thermosyphon, which can achieve phase transition and self-circulation when the lower end of the thermosyphon is heated to make the working fluid vaporise and the vapour moves up to the cold end where it is condensed and goes back to the bottom due to gravity (Reay et al., 2013).

Since then, more and more attention has been attracted to this area, and various applications began to emerge in the space and terrestrial industries due to the excellent

heat transfer coefficient (Seidenberg and Swanson, 1989, Faghri and Thomas, 1989, Noie-Baghban and Majideian, 2000, Reay, 1981).

In 1981 the 4th International Heat Pipe Conference was held in London, and almost 70 papers were published. The areas of applications of heat pipes have since expanded, especially in electronics and energy conservation (Zuo et al., 2001, Singh et al., 2011). Although the technological landscape has changed a lot, the general purpose of heat pipes in each industrial sector has largely remained the same. Adaptations to cater to new designs and technologies, as well as more thorough and accurate modelling due to increased computational power, have been the main advancements since this period. By the early twenty-first century, the heat pipe has become a mass-produced item necessary in consumer electronics products such as lap-top computers that are made by the tens of millions per annum (Reay et al., 2013).

2.1.1 Operation of Heat Pipes

Heat pipes have been produced in a variety of designs, each suited to their application and manufacturing method (Vidal and Cooper, 1969, Faghri, 2012). The simple construction of the heat pipe enables utilisation of both heating and cooling cycles and can have a heat transportation capacity of 10 – 500 W (Vasiliev, 2008). In addition to the standard, constant conductance heat pipe, there are many specialized heat pipes: variable conductance heat pipe can maintain the evaporator temperature over varying power by adding a non-condensable gas (Marcus, 1972); pressure-controlled heat pipe is a variation of a variable conductance heat pipe, the main difference being that the reservoir volume is modulated actively (Zohuri, 2016); diode heat pipe allows heat flow only in one direction (thermosyphon can be considered as a type of diode heat pipe) (Faghri, 1995).

The general principle behind all the heat pipes remains the same throughout. In terms

of function, it usually consists of three parts: evaporator section, adiabatic section and condenser section. In terms of structure, it is composed of a wall and a wick as shown in Figure 2-1.

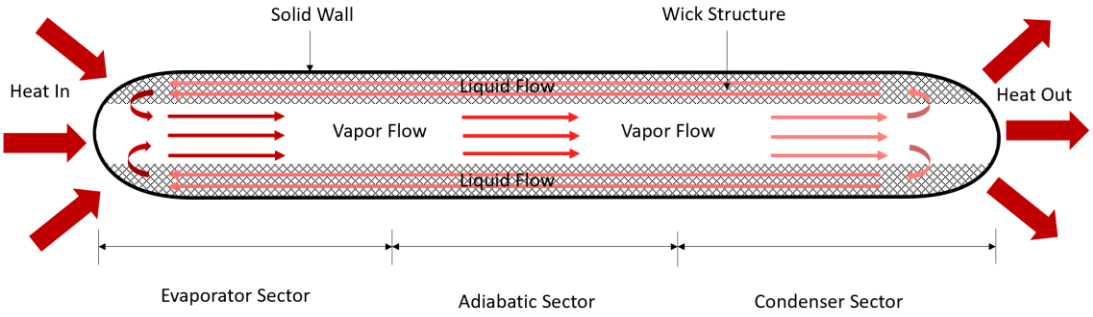

Figure 2- 1 Working principle of the heat pipe

The working fluid is vaporized by absorbing the heat from the hot end, which is called the evaporator section. The vapour moves to the cooler end driven by the pressure differential caused by the vapour influx and condenses back into a liquid by releasing its latent heat (Udell, 1985). The liquid can return to the evaporator section in many ways, such as by gravity, capillary action or centrifugal force (Daniels and Al-Jumaily, 1975).

The heat transfer capacity of the heat pipe is mainly defined by the thermal conductivity of the metal material and the phase transition in the pipe (Nemec et al., 2011). In order to understand the heat transport capacity of a heat pipe, the operating limits for a heat pipe need to be understood. The functionality of the fluid is determined by a set of limits as described in Figure 2-2. Each of these limits can be considered in isolation. In order for the heat pipe to operate, the maximum capillary pumping pressure, ΔP, should satisfy Equation 2.1 (Reay et al., 2013).

$$\Delta P \geq \Delta P_1 + \Delta P_2 + \Delta P_3 \qquad \text{(Equation 2-1)}$$

where ΔP is the maximum capillary pumping pressure, ΔP_1 is the pressure drop required to return the liquid from the condenser to the evaporator, ΔP_2 is the pressure

drop necessary to cause the vapour to flow from the evaporator to the condenser, and ΔP_3 is the pressure due to the gravitational head, which can be positive, negative or zero depending on the inclination of the heat pipe.

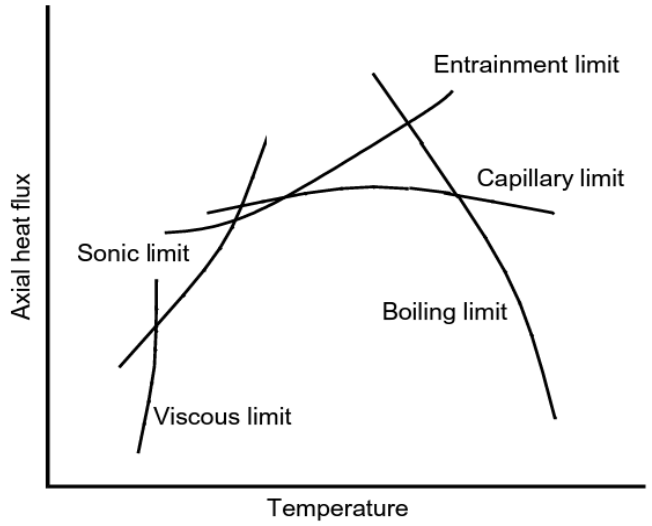

Figure 2- 2 Limits to heat transport in heat pipe (Reay et al., 2013)

When the heat pipe operates at a low temperature or startup, the vapour pressure is minimal, and the required pumping pressure is mainly affected by the viscous force in the vapour channel. Thus, the total vapour pressure within the vapour region may be insufficient to sustain an increased flow (Cao and Faghri, 1992). This condition is referred to as the viscous limit. Once the temperature is high enough so that viscous forces are no longer dominant, the heat flux can be increased, making the evaporated vapour to reach sonic velocities, which may cause choking at the evaporator exit. In this case, the inertial effects of the vapour flow are significant, resulting in a significant increase in temperature gradient along the heat pipe (Nemec et al., 2013). As the vapour velocity keeps increasing, the boundaries between liquid and vapour may create turbulence due to the shearing effect of vapour flow against the liquid. The liquid begins to entrain into the vapour flow when the shear force increases, which will lead to dry out in the evaporator (Nemec et al., 2013). The capillary limit relates

to the essential requirement for a heat pipe to operate. If the capillary pumping pressure is insufficient to provide sufficient liquid flow from the condenser to the evaporator, the wick in the evaporator will dry out (Faghri and Thomas, 1989). The boiling limit occurs when the temperature is very high and the applied evaporator heat flux is sufficient to cause nucleation boiling in the evaporator wick, which causes bubble forming and inhibits the liquid returning to the evaporator, leading to the evaporator dry out.

2.1.2 Wick Structures

For heat pipes in which the position of the evaporator is higher than the position of the condenser, wick structure is indispensable for providing enough capillary force to lift working fluid (Iverson et al., 2007). The selection of the wicks for a heat pipe depends on many factors, such as the compatibility with the working fluid (to avoid non-condensable gas generated into the pipe), the optimum pore size and porosity (to generate capillary action and keep permeability high), and acceptable manufacturing methods. Some typical wick sections are shown in Figure 2-3.

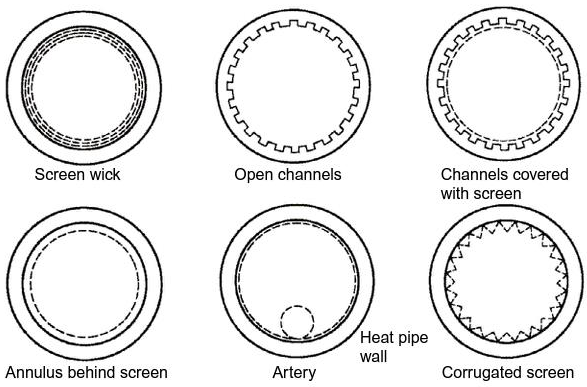

Figure 2- 3 A selection of wick sections (Dunn and Reay, 2012)

The wick structures can generally be classified into three types:

1. Grooved wick, where groves are employed to transport the condensed liquid
2. Screen mesh, where the woven metal mesh is deployed as a capillary mesh

3. Sintered metal powder, where the powder is sintered together to produce an open porous structure

Both grooved wick structure and screen mesh wick structures are shown in Figure 2-4. The grooved wick structure usually consists of axial or circumferential grooves on the inner radius of the pipe (Riehl and dos Santos, 2008). The cross-sectional shape of the grooves can be circular, rectangle, or trapezoidal (Jiao et al., 2007). The "effective pores" of the structure are relatively large compared with that of sintered and mesh structures, so it is difficult to operate against gravity due to the weak capillary action inside the pipes. The maximum heat fluxes for grooved heat pipes can typically be up to 40 W/cm^2 (Staver, 2015). The screen mesh structure is woven from metal threads and is characterised by the mesh number and the wire diameter (Manikandan and Senthilkumar, 2016). Its potential applications are limited because it is difficult and costly to manufacture bent and flat-screen mesh, and it is not able to function against gravity. Screen mesh wicks can typically handle heat fluxes between 10 and 15 W/cm^2 (Groll et al., 1998).

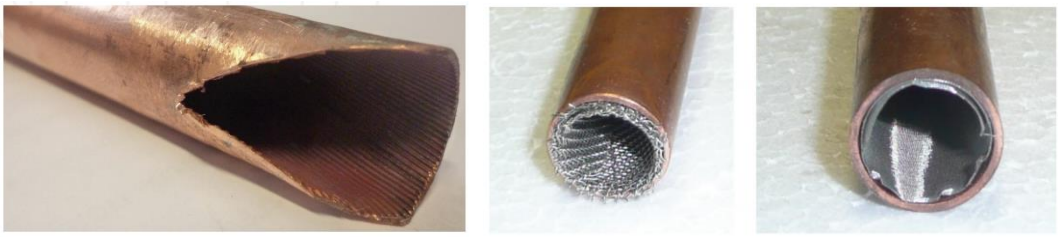

Figure 2- 4 Grooved wick heat pipe (left) and screen mesh heat pipes (middle and right) (Nemec, 2018)

The sintered powder is the most widely used wick structure in the heat pipe applications, and among these, the sintered copper wick is the most common type. Sintering is a process where metal powder is heated at a temperature below its melting point (German, 1996). The powder can be fused and bonded, and a porous structure is

finally formed. Sintering occurs in stages, as illustrated in Figure 2-5. For heat pipes, the initial or intermediate stage is required since the pores can be formed and connected to the external surface. The available ranges of heat flux for high performance sintered heat pipes can be between 50 and 100 W/cm^2 (Groll et al., 1998). Compared with the grooved structure and mesh structure, smaller pores are achievable, which makes it possible to operate against gravity (Jiang et al., 2014).

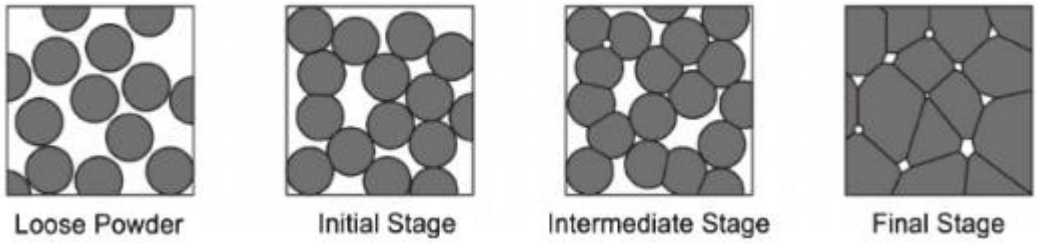

Figure 2- 5 Different stages of sintering (Van Nguyen et al., 2016)

Andreas (2008) predicted the capillary lift height for six different wick structures using Jurin's Law, and the results are presented in Table 2-1. It can be seen that screen mesh wicks provide a lifting height and screen mesh heat pipes work without gravitational support as long as 1) the pipe is reasonably short and 2) its vertical length/height when tilted is below the lifting/ capillary height for the particular mesh deployed.

Table 2- 1 Calculated porosity, effective pore radius and lifting height based on copper/water heat pipe (Andreas, 2008)

	Screen Mesh				Sintered Powder	
Mesh Type	Coarse Mesh 100	Standard Mesh 150	Fine Mesh 200	V. Fine Mesh 250	Powder Type 1	Powder Type 2
Calculated Porosity	0.690	0.709	0.690	0.691	n.a.	n.a.
Effective Pore Radius (μm)	79.3	54.6	39.6	31.9	n.a.	n.a.
Calculated Lifting / Capillary Height (mm)	112	162	223	277	326	366

In order to achieve both high capillarity and high permeability, more and more research has focused on composite wick structures. Li et al. (2013) designed a copper sintered-grooved composite wick that can provide an optimum combination of capillary pressure by the sintered powder and permeability by the grooves, and the thermal resistance of the heat pipe ranged from 0.02 K/W to 0.56 K/W. Tang et al. (2010) sintered copper powder on micro V-grooves and found that the composite structure had a more significant capillary force than grooved and sintered ones. Mwaba et al. (2006) used both screen mesh and sintered copper in heat pipes and found that heat pipes with a composite wick structure provided the best performance.

2.1.3 Research on Various Types of Heat Pipes

Bruce et al. (1979) investigated heat pipes having wicks that were optimally graded in pore size in an axial direction, which is shown in Figure 2-6. The pore size is decreasing from the condenser end to the evaporator end. The porous wick was constructed from a wire mesh. It was observed that heat pipes containing graded porous, non-arterial wick demonstrated substantially improved reliability when

compared with those using arteries. These graded pore size wicks yielded more than twice the heat transfer capacity of axially uniform pore size wick having similar geometries.

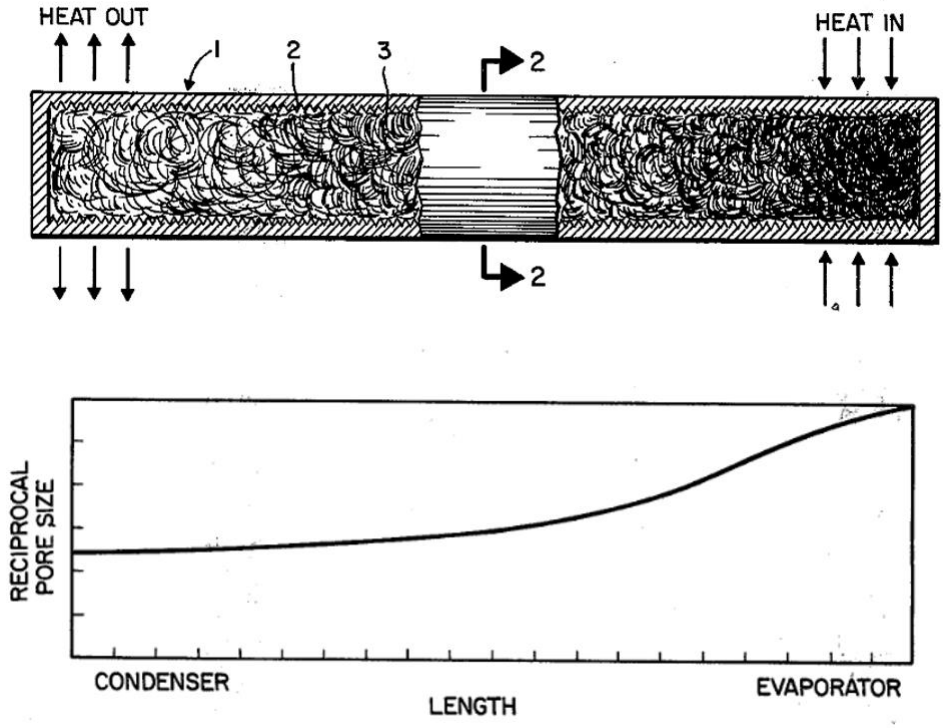

Figure 2- 6 Graded pore size wick in heat pipe (Bruce et al., 1979)

In order to obtain an optimised cross-section along the length of the heat pipe, a novel approach of using a chemical etching technique was undertaken for graded–grooved heat pipe (Michael et al., 1991). The longitudinally extending capillary grooves manufactured by this approach for variable cross-sectional dimensions on the interior surface of the heat pipe were considered as a trade-off between acceptable flow resistance and an acceptable capillary pressure head for the particular application.

A flexible heat pipe was successfully developed for transferring heat from an electronic heat-generating component to a heat sink (Wen-Chen, 2003). The middle segment of the heat pipe consisted of a flexible hose with a capillary structure deposited on the inner tube wall and connected with metal tubes at two ends using

lashing rings. The flexible heat pipe could be adjusted toward any direction, placed over various parts inside a computer, and assembled to the heat-generating component as well as mounted in a ventilating area for evenly and rapidly diffusing the heat to achieve the effect of space utilisation and best heat dissipation.

Hul-Chun (2006) studied a wick structure that was attached to the inner side of heat pipe walls. The wick structure consisted of orthogonal woven thin fibres, extended along the longitudinal direction of the heat pipe. The wick structure could provide an enhanced capillary action and proper attachment to the inner wall of the heat pipe.

2.2 Additive Manufacturing

ASTM has defined additive manufacturing (AM) as "a process of joining materials to make objects from 3D model data, usually layer upon layer, as opposed to subtractive manufacturing methodologies (Frazier, 2014). Once the CAD geometry of a part is designed, and the file is imported into the AM machine, the 3-D part is built by laying down or adding successive layers of liquid, sheet material or powder.

Although AM has attracted much attention over the past two decades, it became involved in commercial productions recently (Frazier, 2014). The advantages of AM are many: it eliminates the shape limit of the products, which makes it flexible to many applications (Thijs et al., 2013); a lower time-to-market and a high material utilization rate (Thijs et al., 2010); excellent repeatability of the manufacturing process (Levy et al., 2003). All the advantages make AM a competitive manufacturing method in many applications.

2.2.1 History of Additive Manufacturing

The origin of AM can be traced back to the 1890s. Blanther tried to use a series of wax plates to impress topographical contour lines (Lanthbr, 1892). The 3-D surface was formed by stacking and smoothing wax plates. Matsubara proposed an actual layer

manufacturing technique by using photopolymer resin-coated refractory particles, which were then selectively cured by visible light (Matsubara, 1974). In 1981, Hideo Kodama of Nagoya Municipal Industrial Research Institute invented two AM photopolymer rapid prototyping systems, where a mask pattern or the scanning fibre transmitter controlled the UV exposure area (Kocovic, 2017). In 1983, StereoLithography (SL) was first invented by Charles W. Hull (Mohammed et al., 2015), where layers were added by curing photopolymers with UV lights and commercialised by a 3D system three years later. Hull defined the process as a "system for generating three–dimensional objects by creating a cross-sectional pattern of the object to be formed." It established the foundation for many AM processes today, including the stereolithography files and digital slicing. Since then AM methods have grown in number such that there are now more than 30 different processes with a large number of system manufacturers generating production-ready machines (Wohlers and Gornet, 2014), including fused deposition modelling (FDM), laminated object manufacturing (LOM), selective laser sintering (SLS), selective laser melting (SLM), direct metal deposition (DMD), laser metal deposition (LMD), inkjet printing, and others. Recent innovations in materials and processes are transforming 3D printing from rapid prototyping to rapid manufacturing. It allows manufacturing near the point of use, enabling "on-demand" manufacturing and drastically reducing inventories and wait times, which has contributed significantly to the fast growth of the AM market since its early beginning (Huang et al., 2015).

2.2.2 Selective Laser Sintering (SLS) and Selective Laser Melting (SLM)

SLS is a powder-based additive manufacturing process, as shown in Figure 2-7. The powder is spread on the platform, and focused laser is used to selectively fuse the surface of powder depending on the embedded CAD files. Once the initial layer is

formed, the platform of the SLS machine drops, usually by less than 0.1 mm, exposing a new layer of powder for the laser to trace and fuse (Palermo, 2013).

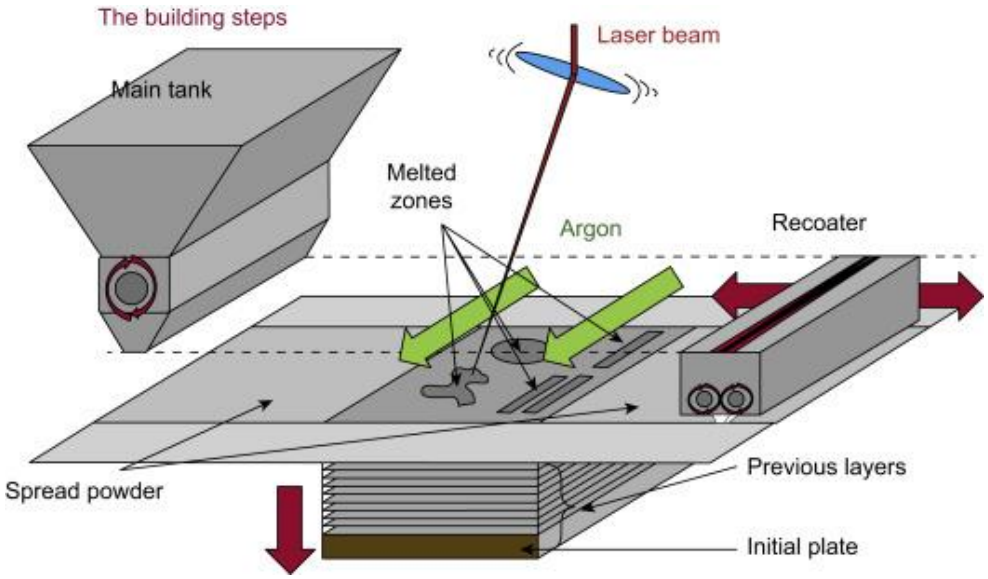

Figure 2- 7 Powder-bed fusion process (sun et al., 2017)

Theoretically, SLS can be used to build parts with any shape in almost any material. Considering powder that has low fusion or sintering properties, a sacrificial binder material can be added in the basic powder. After sintering the full part, the sacrificial binder can be removed by debinding the "green" part in a thermal furnace (Kruth et al., 2003). The available laser types for SLS are various from laser wavelength and laser energy. The selection of laser type and powder characteristics is very critical since it has a significant influence on the surface quality and density of the part (Laoui et al., 1998). The laser wavelength largely depends on the material of sintered powder because laser absorption changes significantly with the material and the frequency or wavelength of the laser light (Tolochko et al., 2000). CO_2 lasers with a wavelength of 10.6 μm are more suitable for polymer materials because polymer materials show high absorption using a long-wavelength laser, whereas Nd: YAG wavelength of 1.06 μm is typically used when metal powder is

used because metals absorb much better at short wavelength.

The SLS technique can be further classified according to the binding mechanism: solid-state sintering, chemically induced binding, liquid phase sintering, full melting (Kruth et al., 2005).

Solid-state sintering occurs at a temperature between 0.5-1 of the melting temperatures of the material. In the sintering stage, the neck is formed between adjacent powder particles due to free energy reduction (Tolochko et al., 2003). The main advantage of solid-state sintering is that a large number of materials can be processed as long as the kinetic energy required for transportation of vacancies across boundaries can be provided by the temperature (Kruth et al., 2005). However, this process is time-consuming due to the slow diffusion of atoms and is therefore not ideal for the long laser scan speed process.

For some materials, binder materials are not added during the manufacturing process, but the disintegration of the material and reaction with the atmosphere can form an induced binder. As an example, SiO_2 is formed during the direct production of SiC ceramic parts (Klocke and Wirtz, 1997). It acts as a binder between the particles and afterwards, an infiltration step using Si yields full dense parts.

Liquid phase sintering can be considered in two ways: whether the structural materials and binder materials are the same or not. Figure 2-8 shows the mechanism of liquid phase sintering with different structural and binder materials schematically. The solid line shows the traditional furnace sintering process, which consists of three stages: rearrangement, solution reprecipitation, and solid-state sintering. Once the low melting-point binder material is liquefied and the high melting-point structure material stays stable, the liquid binder can spread through the

pores by capillary forces and causes a rearrangement of the particles. Furthermore, the liquid improves transport rates responsible for grain coarsening and densification due to the solid solubility in the liquid (German et al., 2009)

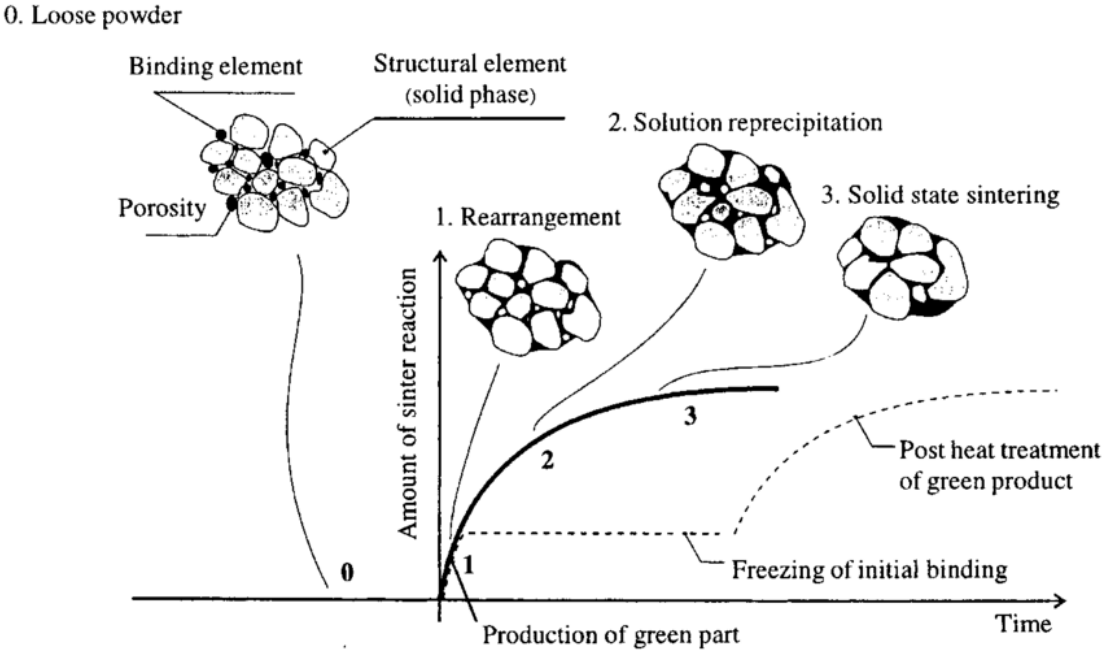

Figure 2- 8 Mechanism of liquid phase sintering (Wang et al., 2002)

However, in the SLS process, the laser beam is used to heat the materials quickly and moved away, which causes the melted area cooling rapidly, and only the rearrangement phase takes place (as shown by the dashed line in Figure 2-9). Generally, a green part is produced, which is porous and brittle. Therefore a post-heat treatment includes infiltration, furnace post-sintering, or hot isostatic pressing is necessary for decreasing the inherent porosities and the occurrence of residual stresses (Mercelis and Kruth, 2006).

When the binder material and structural material are the same, usually, the core of the grain is usually solid throughout and only a shell at the grain border is melted (Kruth et al., 2007). It can be called partial melting, and the melted portion acts as the binder material.

However, if nearly full dense parts with comparable mechanical properties are necessary, full melting, which is also called Selective Laser Melting as well, is proposed as a suitable method without long manufacturing period and complex post processes. SLM is an AM process that can be used to produce highly complex parts for a variety of industries (Thijs et al., 2010, Kruth et al., 2005). It uses high power laser to melt and fuse metal powder fully and builds the parts layer by layer. A CAD model generates the shape of the parts, and specific machine code files can control the laser scanning strategy. Eventually, the parts can be created after removing all the un-fused powder. In order to manufacture parts, SLM requires the use of fine powder of reactive metals, which typically has significant handling problems for both safety and materials quality perspectives. The industrialisation of SLM has gradually overcome these issues with the powders, which can now be stored and used under protective atmospheres, minimising contact with air and moisture during production. These changes have resulted in an improved flowability of the powder, reduced fire and health hazards and minimized the formation of oxides and hydrates affecting part integrity. This approach has worked well with stainless steel, titanium alloys, and other reactive materials. It is relatively easy to produce 100% dense stainless steel and titanium parts and these parts can reliably reproduce the properties of bulk materials.

2.2.3 Process Parameter in SLM

It is well known that the laser parameters such as laser wavelength, laser power, laser scan speed, laser spot diameter, hatch distance, layer thickness, scan strategy and powder properties, as shown in Figure 2-9, significantly affect the rapid melting and solidification process and therefore to the printed sample's properties.

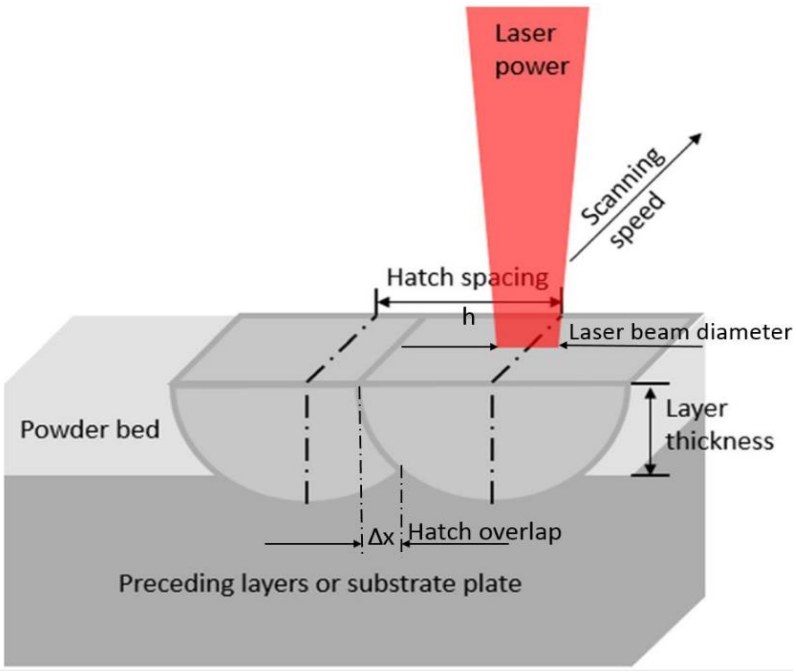

Figure 2- 9 Schematic diagram of SLM process parameters (Kasuma and Chandrakanth, 2016)

Laser Source

In the SLM process, there usually are three types of laser: CO_2 laser, Nd: YAG laser, and Yb-fibre laser. The CO_2 laser is one of the earliest gas lasers, developed in 1964 (Patel et al., 1964). In CO_2 lasers, the gas state gain medium, CO2, fills the discharge tube and is electrically pumped by a DC or AC to induce the population inversion of lasing (Hyub et al., 2017). It has many advantages such as low cost, high power output with relatively high efficiency. Usually, CO_2 generates an infrared output wavelength of about 10.6 um, which is not suitable for manufacturing metal part due to the low light absorption coefficient in this infrared region. Nd: YAG lasers (neodymium-doped yttrium aluminium garnet laser; Nd3+: Y3Al5O12 laser) are one of the most commonly used high-power lasers in the industry. In Nd: YAG lasers, rod-shaped Nd: YAG crystal is optically pumped by a flash tube or a laser diode, and it can be used both in the continuous mode and in the pulsed mode. Nd: YAG typically generates an

infrared output wavelength of 1064 nm and it can be used in many applications that need high power density and a high repetition rate (Bass and Michael, 2012). Yb-doped fibre lasers are a type of rare-earth-doped gain-fibres, which is pumped by the laser diode. It provides infrared laser beams about 1064 nm output wavelength. In recent years, Yb-doped fibre lasers become the most promising laser source because of high electrical-to-optical efficiency, excellent beam quality, robustness against environmental disturbances, and system compactness. (Majumdar et al., 2012)

Hatch Distance

Hatch distance is another important parameter associated with the SLM process. During the SLM process, in order to selectively melt the deposited powder on the substrate plate, the laser usually melts the entire area of the powder in the form of a series of tracks. The width of the tracks is affected by many factors such as laser power, scan speed, laser spot diameter. The specific distance between adjacent tracks is defined as hatch distance, as shown in Figure 2-8. To get better quality samples, usually there is an overlap between two hatches, which is called hatch overlap. It is necessary, especially for the samples required to be solid without pores. In most of the SLM processes, an overlap of at least 20% is maintained to have better quality samples (Prashanth and Konda, 2014).

Laser Energy and Laser Energy Density

Laser energy is a function of the laser power, the mode of the laser, the laser spot size, and the laser scanning speed. High laser power means more heat input, and the deeper the laser can penetrate the layer, which provides a stabilizing effect for forming continuous individual tracks. However, excessively high laser power can cause metal powder vaporization, spatter, and keyhole porosity (Thanki et al., 2019). Also, instabilities appear at low scanning speed in the form of distortions and irregularities

attributed to a capillary instability or Plateau-Rayleigh instability. On the contrary, excessively high speed gives rise to the balling effect (Yadroitsev et al., 2010). Matthews et al. (2016) investigated the denudation phenomenon of titanium alloy and steel alloy powders under varying laser conditions and ambient Ar pressure extensively. According to them, the denudation can mostly be due to intense metallic vaporization near the laser spot, provoking entrainment of powder particles.

Furthermore, to evaluate the combined effect of laser power, scanning speed, hatching space and layer thickness, an advanced parameter called volumetric laser energy density (VED) is used as follows: (Gu, 2015)

$$VED = \frac{P}{v.h.t} \qquad \text{(Equation 2-2)}$$

where P is laser power, v is laser scan speed, h is hatch spacing, and t is layer thickness. The increasing laser power allows melting at faster speeds and greater depths of heat penetration. The faster the scan speed, the less time there is for heating and, therefore, with given laser power, less time for the heat to diffuse sideways, causing a narrowing melt of the melt region and heat-affected zone (Kasuma and Chandrakanth, 2016). In terms of the layer thickness, it should always be larger than the powder size and cannot be too thick because the laser beam cannot penetrate the whole layer of the powder causing insufficient bonding with the previous layer. The lower the layer thickness, the denser layer and higher dimensional accuracy are achieved, and higher mechanical properties and microhardness can be obtained (Nguyen et al., 2018).

Powder Properties

The shape, size and distribution of powder particles have a significant impact on the parts manufactured by SLM. One of the essential properties for powder is the flowability, which is dictated by the ratio of the larger to the smaller particles in the powder (Zhu, 2007). In the SLM process, the powder is deposited by gravity through

a system of valves, so the used powder must be spherical because the irregular shaped of the powder shows poor flowability as their particle tend to lock into each other impeding their movement as shown in Figure 2-10.

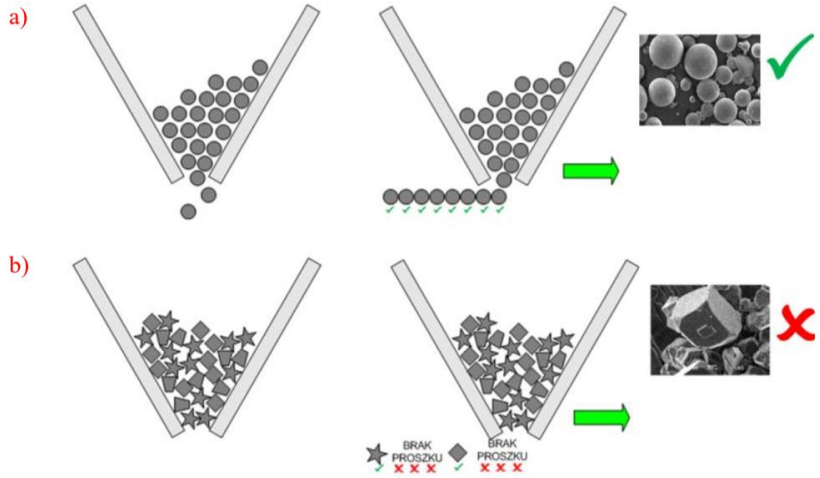

Figure 2- 10 Layer deposition: a) spherical powder, b) irregular powder (Kurzynowski et al., 2012)

The powder suitable for SLM is typically in the particle size range from 15 µm to 45 µm, suitable for SLM. This typical narrow size distribution range is good for the laser to melt all the powder particles at once during the laser exposure (Choi et al., 2017). Also, particle size and particle size distribution have a significant influence on the surface roughness. Large particle size and wide particle distribution can lead to increased layer thickness, which means the laser beam has to diverge by a more considerable distance to form a melt pool and results in an asymmetry in the pool width, which can increase the surface roughness (Mazumder et al., 2000).

Scanning Strategy

There are many types of laser scanning strategy in the SLM process, depending on the design of the user and the specific requirement of the final parts. Figure 2-10 indicates three basic scanning strategies with distinct different hatch styles between each other. These scanning patterns can be repeated every layer with or without the presence of

scanning pattern rotations between the layers. Many reports have studied the relationship between the residual stress and scanning strategy, and it is found that strategies with shorter scan vector and the rotation of the scanning pattern between layers can generate less residual stress (Cheng et al., 2016; Mercelis et al., 2006).

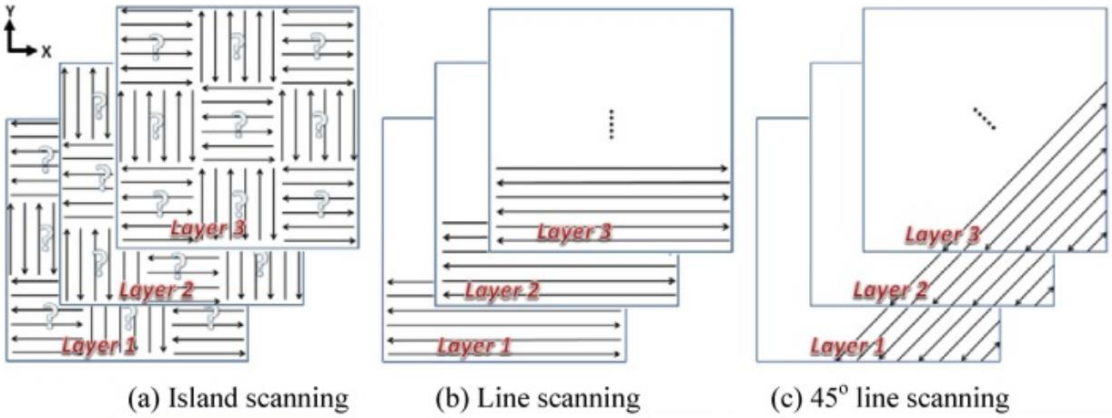

Figure 2- 11 Different types of scanning strategy (Cheng et al., 2016)

2.2.4 Porous Structure Produced by SLM

In the past, SLM is ordinarily used to produce solid metal components because a complex 3D problem can be decomposed into a series of 2D ones. It is a beneficial method to produce complex engineering structures. In recent years, the method has also shown excellent performance in the production of open-celled porous structures. These open-celled porous structures have shown utility in the production of light-weight high mechanical performance sandwich structures (Brenne et al., 2013); high strength and stiffness to weight ratio gyroid structures (Challis et al., 2014); and osseointegration medical implants described in (Stamp et al., 2009).

Heinl et al. (2008) developed a diamond structure and a hatched structure in Ti-6Al-4V for bone implants, as shown in Figure 2-12. These two porous structures are fully interconnected with a porosity of 80.5% and 61.3%, respectively and with a pore size of 1.23 mm and 0.45 mm, respectively. It has been proven that the mechanical properties of these cellular structures are similar to those of human bone.

A program was undertaken at the UoL to develop an industrial process to produce orthopaedic components with porous surfaces. The initial work, using beam overlap principles (US 7537664 and EP1418013 patents), involved developing a standard scanning strategy to produce parts using SLM, as shown in Figure 2-13.

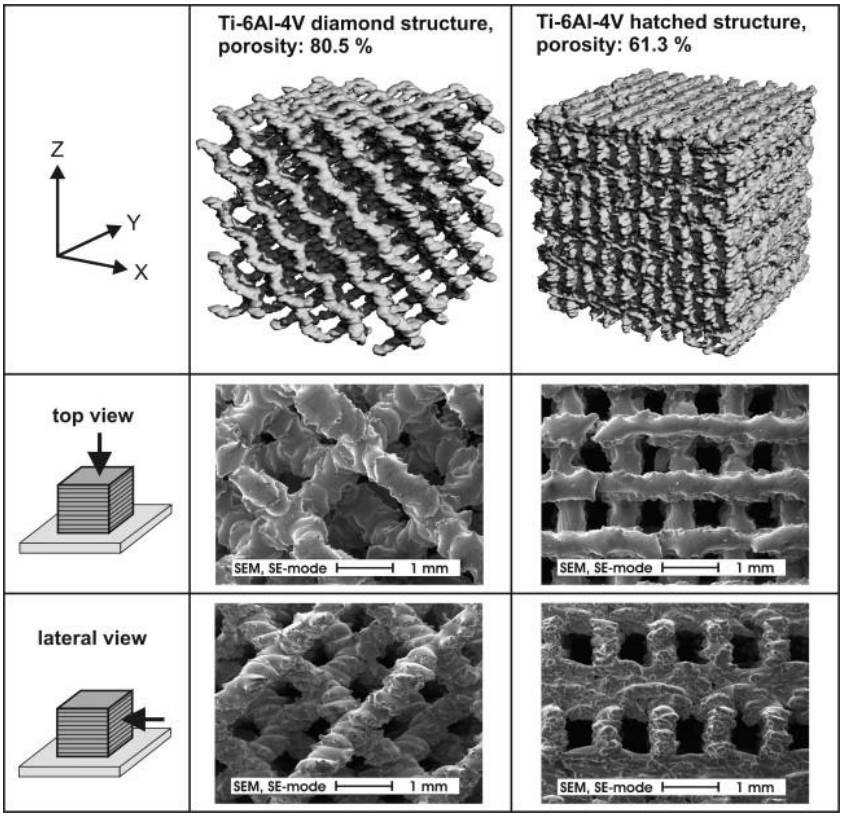

Figure 2- 12 3D Image from µCT measurement of Ti–6Al–4V structures with the corresponding SEM micrographs in top and lateral views (Heinl et al., 2008)

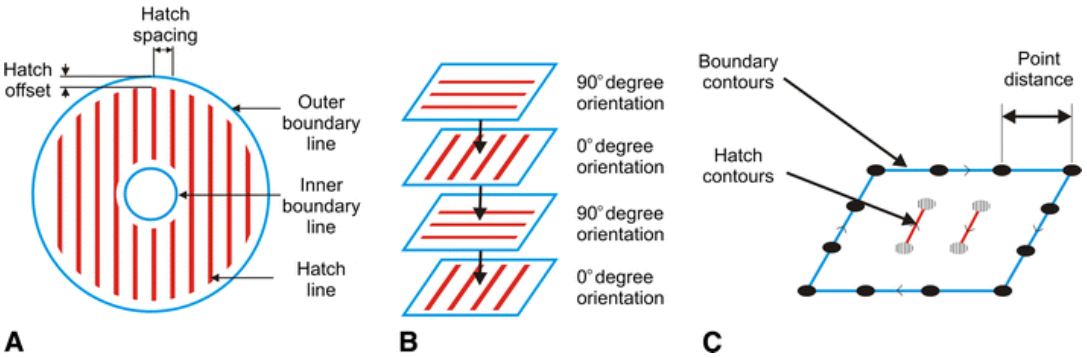

Figure 2- 13 The SLM laser scanning strategy for melting layer geometries (Stamp et al., 2009)

The scanning strategy consists of scan lines separated by a spacing measured from the centres of adjacent lines. A boundary contour surrounds the geometry to improve surface finish, and in each subsequent layer, the lines are orientated at 90° to the previous ones. The laser scans lines, which consist of a sequence of points. The laser scans each point for a specified time.

Porous parts have been manufactured using the above-modified scanning strategy, and these parts were created by selecting laser processing parameters to produce walls of such thickness and hatch spacing that there was no overlap between the individual scan lines. An acetabular cup model produced by this strategy is shown in Figure 2-14. This structure exhibits controllable pore size and porosity while simultaneously possesses excellent mechanical strength.

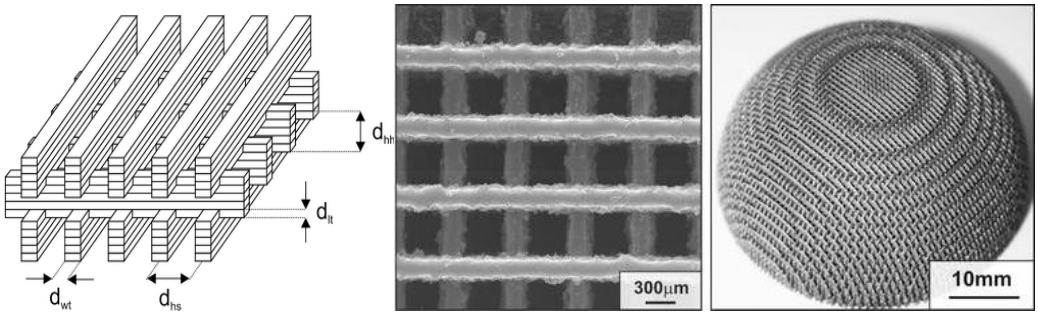

Figure 2- 14 The beam overlap structure applied to an acetabular cup (Stamp et al., 2009)

Thompson et al. (2015) developed a compact flat-plate oscillating heat pipe in Ti6Al4V using the SLM process. It has been proven that the heat pipe can operate successfully with an effective thermal conductivity of approximately 11 W/mK. The quality of the surface inside the pipe is not satisfactory, as shown in Figure 2-15, and it is gravity dependent. High surface roughness and the balling phenomenon can be the most significant issues in the SLM manufacturing process. However, the ability of capillary force and heat transfer performance can benefit from the rough surface

because it provides extra channels with small pores into the structure.

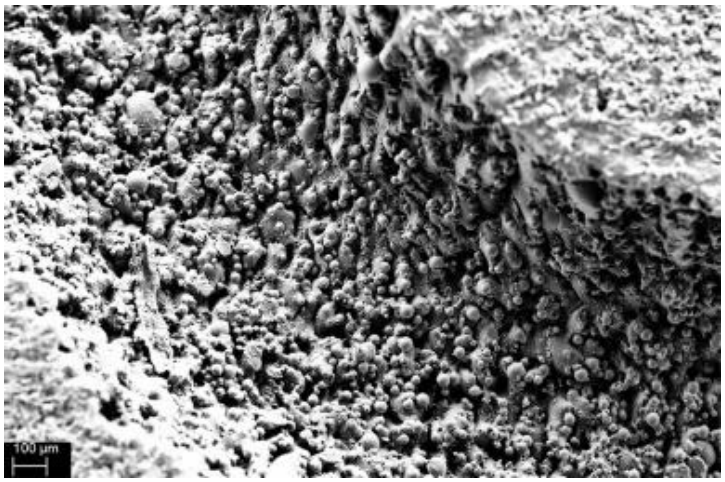

Figure 2- 15 Scanning electron microscope image along the channel within the heat pipe manufactured by SLM (Thompson et al., 2015)

However, according to the research by Wang et al. (2013), there are several processing restrictions for SLM fabrication of porous structure, including overhanging structure, fabricating resolution and powder adhesion. It has been proven that when the strut of the porous structure has a small inclined angle, it would be difficult to achieve better control of the quality of the porous structure when the struts of the porous structure have a small inclined angle.

A porous structure has also been designed by the unit cell approach (Mullen et al., 2009b). The approach can be summarised as follows: the CAD geometry is populated with cuboids of a defined unit cell size, and the cuboids are individually populated with nodes and struts. It is also possible to introduce a more random appearance by perturbing the individual links by pre-defined amounts. In fact, they are pseudo-random, i.e., they appear random but are based on the underlying regular structure (Figure 2-16).

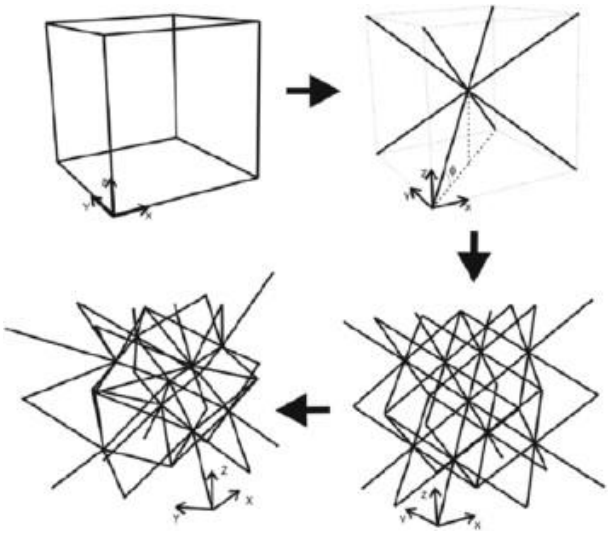

Figure 2- 16 Transformation from the regular unit cell to randomized unit cell (Ameli et al., 2013)

This approach has been devised and implemented for the manufacture of porous bone in-growth structure. It can be optimized for a specific location within the body with predefined physical and mechanical properties (Mullen et al., 2009b). This structure possesses its unique advantages, such as strong systematicness, good coherence, wide-coverage, simple deduction and practical convenience (Liu et al., 2020). By adjusting the inclined angle of the pore's strut, the octahedral structure can theoretically avoid the overhanging surface with a small inclined angle, thus can avoid the defects of hanging dross and jamming pore. In practical applications, the controllable porous structure shows much better permeability and wettability which makes it perfect for a heat pipe application.

The manufacture of the porous structure of internal wick for the heat pipe has been developed at the University of Liverpool by following the protocol currently established to produce porous surfaces for the manufacture of orthopaedic components (Stamp et al., 2009). In order to assess the feasibility of manufacturing the proposed designs, various designs shown in Figure 2-17 and Figure 2-18 were proposed as

preliminary prototypes for heat pipes, manufactured in aluminium alloy.

Based on the preliminary investigation for the development of heat pipes by SLM, it was successfully demonstrated that a sophisticated design with porous wick could be seamlessly integrated. The unit cell approach mentioned above was used to manufacture the capillary wick structure.

The experimental results of the 300 and 500 μm unit cell sizes show that the porosity was in the range of 17-58%, and the pore size was in the range of 60-140 μm, while the permeability varied between 10^{-13} to 10^{-10} m^2 (Ameli et al., 2013).

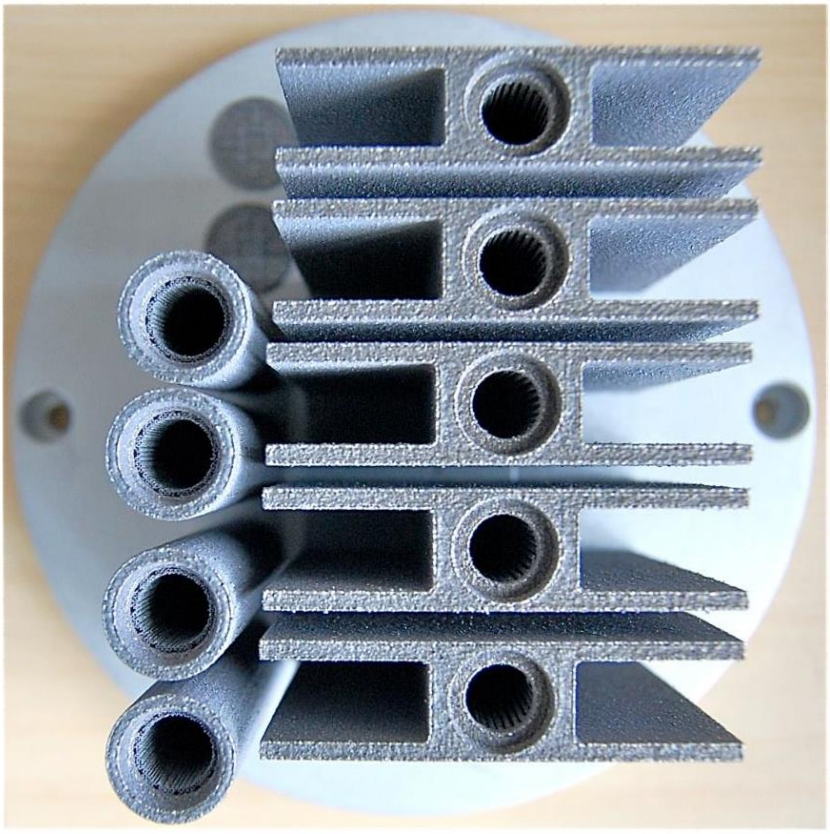

Figure 2- 17 Arterial and grove structures manufactured from AlSi12

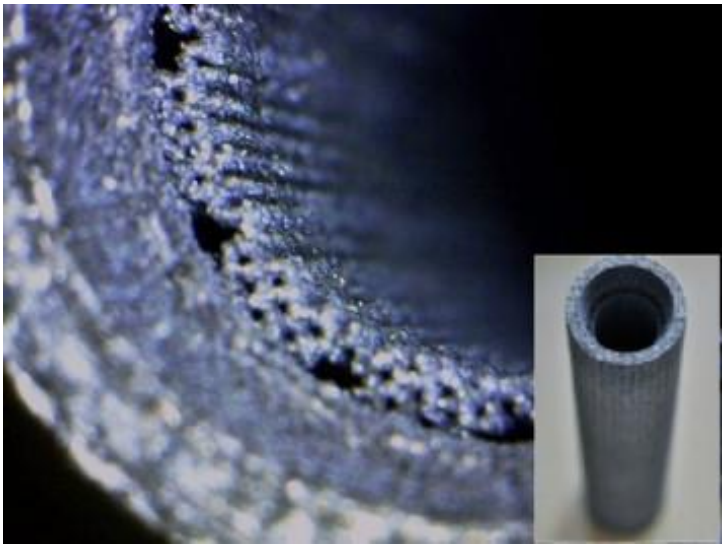

Figure 2- 18 Arterial wick heat pipe made by SLM (Ameli et al., 2013)

However, the challenge comes from the solid wall, as shown in Figure 2-19. It was found that the density of the SLM solid structures was only between 74.0% and 89.3% (Ameli et al., 2013), and the pores were not evenly distributed across the structure but randomly located. This is very critical problem because the pipe may fail during operation due to leakage or breakage by the high vapour pressure of the working fluid. Moreover, aluminium and its alloys are not compatible with the most potential low temperature working fluids, which means new alternative materials need to be developed. Also, the capillary action inside the wick structure needs to be further investigated.

Figure 2- 19 Pores in an SLM solid structure (Ameli et al., 2013)

2.3 Fluid and Thermal Properties of Porous Structures

The characteristics of porous structures manufactured by the SLM process can be varied with different laser strategies. The transport phenomenon in porous structures is especially important in heat transfer applications. There is much research on the role played by pore structure in determining transport phenomena in pore space and on the relationship between fluid or thermal properties and integral porous structure (Dullien, 2012). However, the best suitable geometrical structure for heat pipes should demonstrate the maximum capillary force needed for efficient performance of the heat pipes.

2.3.1 Characterisation of Porous Structure

The porous structure can be typically be defined by its porosity and pore size. Porosity refers to the fraction of void volume to total volume in the structure. High porosity means fluids can move through the structure with more ease and less resistance. There are many methods for determining porosity. Most measurements are conducted for the measurement of open porosity and are based on the Archimedes methods. Various absorption methods, using different fluid or gases, are used to make the apparent porosity measurements (Anovitz and Cole, 2015). Gros and Panneton (2004) measured the porosity of an aluminium foam by measuring the "missing mass" of the porous structure in air and vacuum. Salissou and Panneton (2007) measured four masses at four static pressures to deduce the open porosity of porous solids used in sound-absorbing liners. Panneton and Gros (2005) measured the open porosity of air-saturated porous materials by measuring the weight of the sample in air and under vacuum conditions and calculated the porosity by:

$$\varphi = 1 - \frac{M_1 - M_1'}{\rho_f V_t} \qquad \text{(Equation 2-3)}$$

where φ is the open porosity; M_1 is the weight measured under vacuum condition; M_1' is the weight measured in the air; ρ_f is the density of saturated air in the porous aggregate; V_t is the total volume of the structure.

Pore size is a more complex term to be defined because the "pores" in different porous structures can be varying from the shape, size, and distribution. In most cases, the average pore size is adopted for calculation or prediction. With the development of digital images and computer software, image processing, including 2D and 3D techniques, provides several methods to determine the pore size (Lawrence and Jiang, 2017). Images taken by optical light microscopy, scanning electron microscopy and X-ray tomography were used to give the pore distribution inside the structure directly, and the pore size was analysed using image processing software (Yang et al., 2014). Howard and Kenyon (1992) determined the pore size in sedimentary rocks by measuring nuclear magnetic resonance relaxation time in water-saturated rock. The relaxation distribution curve can be scaled to pore size distribution by a phenomenological parameter that describes the strength of the proton interaction between the fluid and the pore wall.

In some cases, the hydraulic diameter is used to replace the pore size (Shin, 2017). Hydraulic diameter is used for a pore or a conduit of non-circular shape. It is usually expressed as:

$$D_h = 4\frac{A}{P_w} \qquad \text{(Equation 2-4)}$$

where D_h is the hydraulic diameter; A is the cross-sectional area of the flow; P_w is the wetted perimeter.

The hydraulic diameter may be used to determine the flow regime of a flowing fluid by calculating the Reynolds number (Neutrium, 2012). Most of the porous structures

manufactured by SLM are not real "pores" existing in the components, so hydraulic diameter becomes an alternative parameter when considering the relationship between fluid properties and the structures.

2.3.2 Permeability

Permeability, which is used to denote how easy a fluid can pass through, is one of the most critical properties of open porous structures. It has been considered in many experimental and simulation studies (Kumar et al., 2010, Zuo et al., 2012, Eshghinejadfard et al., 2016) and it is typically attempted to find functional correlation between the permeability and some other macro properties of the porous medium such as porosity (Koponen et al., 1997). Permeability can be expressed in different ways according to the flow regime. It appears in Darcy's law, which governs flow through the porous structure in the creeping flow regime and laminar flow regime, expressed as follows:

$$\frac{\Delta P}{\Delta x} = -\frac{\mu}{K} v_d \qquad \text{(Equation 2-5)}$$

where $\Delta P/\Delta x$ is the pressure drop along the flow direction; μ is the viscosity of the fluid; K is the permeability of the structure; v_d is Darcy velocity.

Darcy velocity is not the actual velocity of the fluid passing through the pore structure. It is defined as Darcy flux, which is volume flow rate divided by the cross sectional area of the porous medium, divided by the porosity as Equation 2.6. It needs to be considered that only a fraction of volume in the structure is available for flow.

$$v_d = \frac{q}{\varphi} \qquad \text{(Equation 2-6)}$$

where q is the flux; φ is the porosity of the structure.

Laminar flow occurs when the fluid flows in parallel layers with no disruption between them (SimWiki). The Reynolds number for laminar flow is very small, usually less

than 1. According to (Bear, 2013), the upper limit for Darcy's law can be extended to 10 (shown in Figure 2-20), where the velocity is very slow, and no eddies and swirls are existing in the flow, such that the flow is ruled by momentum diffusion and viscous resistance is higher than inertial resistance.

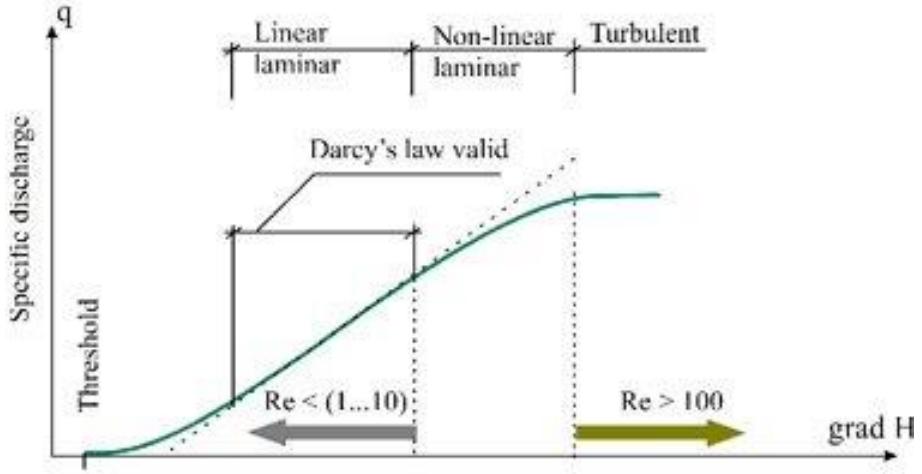

Figure 2- 20 Range of validity of Darcy's law (DROBOT)

An application of Darcy's law is to water flow through the aquifer. It is also applicable to seepage flow in sandy or clay soils. Vincent et al. (2014) used Darcy's law to determine which medium was able to hold water rather than supporting percolation. Ridgway et al. (2003) used Darcy's Equation to compare the liquid permeability coefficient with the air permeability coefficient and found a close agreement between the two values.

The flow transits to turbulent, with velocity increasing. In this regime, the Reynold number can be very high, more than 100. The dominant mechanism is that the drag force on the wall impedes fluid causing irregular fluctuation and chaotic eddies and swirls. The existence of spontaneous eddies and swirls can cause the dissipation of the kinetic energy of fluid motion as heat and hence increases the resistance to flow. This resistance can be described as the inertial resistance. The inertial force for the fluid

flow is larger than the viscous force which is contrary to the laminar flow. The pressure driving flow through porous media must be equal to the viscous resistance plus the inertial resistance (Barr, 2001). Therefore, Darcy's equation is modified to the Forcheheimer equation (Forchheimer, 1901):

$$\frac{\Delta P}{\Delta x} = -\frac{\mu}{K} v_d - \rho C v_d^2 \qquad \text{(Equation 2-7)}$$

where ρ is the density of the fluid; C is the form drag coefficient of the porous structure. In some research (Belforte et al., 2007), the inertial term can be expressed using an inertial coefficient C_f.

$$C_f = C\sqrt{K} \qquad \text{(Equation 2-8)}$$

The inertial coefficient is a property of the porous medium. The correlation between the inertial coefficient and structural properties generally could be divided into empirical correlations and theoretical predictions (Li and Engler, 2001). Li and Engler (2001) compared the non-linear laminar flow equation with the Forcheheimer equation and found that the inertial coefficient is a function of pore size distribution, tortuosity, permeability, and porosity of the porous medium. The results of empirical correlations can be varying because of various porous structures and fluids.

Estimation of permeability is essential for the description of different physical processes. Typically, permeability is expressed as a function of structural properties such as porosity and tortuosity (Costa, 2006). However, it is very complicated to formulate a universal model for permeability since the structures for different porous media can be varying. Two porous structures with the same porosity and average pore size can possess different permeabilities. One of the most widely accepted models for permeability-porosity relationship is the Kozeny-Carman equation (Kozeny, 1927), but it has many limitations. Many researchers have modified the Kozeny-Carman

equation to make it more accurate for specific porous media. Costa (2006) obtained a new permeability-porosity relationship based on a fractal pore space geometry assumption for a reasonable estimation of different non-granular systems such as fibre mats and vesicular rocks. Kaviany (2012) modified the Equation by introducing tortuosity and specific surface area, and the empirical Kozeny constant of approximately five was given for bed packed with spherical particles. The effective porosity and percolation were taken into consideration for the modification applied for reservoir rocks (Mavko and Nur, 1997)

2.3.3 Capillary Action in Porous Structures

In a tube or porous medium, if the diameter or pore size is small enough, a liquid can pass through pores without the assistance of external force. This phenomenon is called capillary action, and the driving force pushing the fluid movement is a capillary force. Capillary action is common in nature and daily life, such as candle wick, sponge, and for plants absorbing water from roots. Liquid flow driven by capillary forces has attracted much attention in many applications in science and industry. For example, in technical applications such as heat pipes or the spacecraft Propellant Management Device capillarity is of high importance (Fries and Quéré, 2010). For heat pipes working against gravity, as shown in Equation 2.1, the necessary capillary pressure provided by the wick structure should be more than the sum of the pressure drop required to return the liquid from the condenser to the evaporator and the pressure drop necessary to cause the vapour to flow from the evaporator to the condenser and the pressure due to the gravitational head, as shown in Equation 2.1.

The capillary force can be obtained by the Young and Laplace equation (Pujado et al., 1972) as described below:

$$\Delta P = 2\gamma H \qquad \text{(Equation 2-9)}$$

where ΔP is the pressure difference across the fluid interface; γ is the surface tension; H is the mean curvature of the channel.

Two experimental methods are usually employed to study liquid penetration in porous structure: one is to measure the height change of the advance liquid front over time, and another is to measure the weight change of the working fluid absorbed by the porous structure. Chen et al. (2007) used an optical microscope and a couple-charged camera to capture the liquid fronts of micro-grooved samples. Tang et al. (2010) used an infrared camera to measure the capillary force of a sintered-grooved composite wick structure. The infrared thermal images showed different colours between dry and wet materials because of the different infrared emissivity. Tang et al. (2010) also derived an equation where the pressure difference existing in the porous structure is divided into two parts, friction pressure loss and hydrostatic pressure loss, as described below:

$$\Delta P = \frac{\mu\varphi}{K} h \frac{dh}{dt} + \rho g h \qquad \text{(Equation 2-10)}$$

where h is the wetted height, $\frac{dh}{dt}$ is the wetting rate, which is related to the mass flow rate. It illustrates that a sample with a higher lifting height has a more significant capillary force. Therefore, the capillary action of different samples can be compared by comparing the lifting height in opposition to gravity.

Theoretically, one of the most used models for predicting the lift height for a narrow tube in opposition to gravity is Jurin's Law (Batchelor, 2000).

$$h = \frac{2\gamma cos\theta}{\rho g r} \qquad \text{(Equation 2-11)}$$

where γ is the surface tension; θ is the contact angle; g is the local acceleration due to gravity; r is the radius of the tube. It has been widely accepted that capillary action occurs because of intermolecular forces between the liquid and surrounding solid

surfaces, and it is mainly decided by two factors: cohesive force and adhesive force. Cohesive forces are the intermolecular forces that cause a tendency in liquids to resist separation and maintain a specific shape. Adhesive forces are attractive forces between different molecules. Capillary action in H_2O and mercury is different, as shown in Figure 2-21. The cohesive force is smaller than the adhesive force with gas so a concave meniscus is formed and rises for water, whereas the cohesive force is larger than the adhesive force with glass, so a convex meniscus is formed and declines for mercury. Ellison et al. (1967) studied the contact angle between mercury and different solid surfaces under temperatures of 25-150 ℃ and the range of contact angle was from 110-180°.

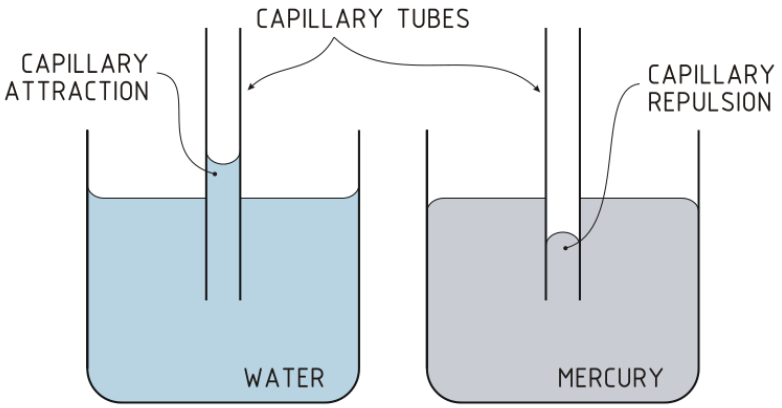

Figure 2- 21 Capillary actions in water and mercury (CHEMISTRY, 2017)

The situation becomes complicated in porous structure because the path of liquid is tortuous and unpredictable. Equation 2.11 is not an ideal rule anymore because the contact angles on an individual particles or granules are hard to be determined. Some researchers have measured the contact angles by putting a liquid droplet on a flat surfcae made by compressed powder or granules (Zografi and Tam, 1976, Lerk et al., 1977). The biggest problem is that the compressed flat surface is not real solid

approaching 100% density, and pores are existing inside the structure. “Spontaneous” liquid penetration might occur if the actual contact angle between the liquid and the solid is lower than 90°. Moreover, the actual rate of penetration might vary largely depending on the actual wettability and the porous structure (Yuan and Lee, 2013). The experimental results can also be influenced by several factors, such as surface roughness and porosity (Buckton and Newton, 1986, Buckton and Newton, 1985).

There is little research on the effect of surface roughness on the capillary pressure in heat pipe applications. The increasing surface roughness of the solid wall can enhance wettability by changing the wetting angle between the wall and the fluid (Kalmikov, 2010). The geometric disorder caused by surface roughness increase can lead to increases in fluid trapping due to capillary action (ayaz et al., 2019). The relationship between the surface roughness of parts manufactured by SLM and the capillary lift height was first investigated in this study.

2.3.4 Heat Transfer Performance of Porous Structures

The porous structure has attracted many interests for use in heat exchangers because it can enhance convective thermal transport and maximize heat transfer. Typically, high conductivity materials such as copper and aluminium are used. Ko and Anand (2003) measured the heat transfer coefficient in a uniformly heated rectangular channel with wall mounted porous aluminium baffles. The results were compared with a straight channel with no baffles, and they showed that the use of porous baffles could enhance the heat transfer as much as 300%. Boomsma et al. (2003) used an open-cell aluminium alloy foam with an average cell diameter of 2.3 mm in a forced convection arrangement using water as the coolant. They found that the thermal resistance of aluminium foam heat exchangers was two or three times lower than the best commercially available heat exchanger. Ding et al. (2011) measured the

comprehensive heat transfer coefficient for heat exchangers with four kinds of porous structures: copper wire mesh, metal foam, copper fibre sintered felts and cross-connected micro-channel plates. It was found that all the porous structures could enhance the heat transfer performance, and the heat exchanger with copper metal foam had the most significant comprehensive heat transfer coefficient, which was 2.5 times as high as the heat exchanger without any porous structure. Zhang et al. (2009) investigated the heat transfer performance of porous copper manufactured by the Lost Carbonate Sintering process with porosity range from 57% to 82% and pore size range from 150 to 1500 μm and found that porous copper can increase the heat transfer coefficient by 2 to 3 times compared to an open channel.

Many factors can influence the heat transfer performance of the porous structures. Zhang et al. (2009) found that porosity is one of the most critical factors affecting the heat transfer performance because of its significant influence on the permeability and the thermal conductivity of the sample, whereas pore size shows much less effect. Kim et al. (2000) investigated the heat transfer performance of high porosity aluminium alloy foam with three pore densities (10, 20 and 40 pores per inch), and found that the heat transfer performance can be enhanced by increasing the pore density. Liu et al. (2017) measured the heat transfer performance of porous titanium fibre materials made by the vacuum sintering method with different structural parameters. Better heat transfer performance was observed when overheating was less than 10℃, or smaller wire diameter was used.

Many researchers have investigated the overall heat transfer performance of heat pipes. Sintered powder or metal mesh porous structures can affect the heat transfer performance of heat pipes. Ren et al. (2007) found out that the total heat transfer coefficient of sintered nickel powder loop heat pipe is a function of permeability. The

primary heat transfer mode changed from conductive heat transfer to convective heat transfer when the heat flux increased. Singh et al. (2009) studied the influences of wick characteristics on loop heat pipe and found that larger porosity, smaller pore size and higher permeability of the wick can result in better heat transfer performance. Celata et al. (2010) investigated the thermal characteristics of a loop heat pipe with stainless steel mesh wick. Nishikawara and Nagano (2014) fabricated a miniature loop heat pipe with PTFE wicks, and a maximum heat load of 40 W and an applied heat flux of 4 W/cm^2 was achieved with ethanol as the working fluid. Liu et al. (2012) developed a novel loop heat pipe with two different wick structures: sintered nickel powder as the primary wick and stainless-steel mesh as the secondary wick. They showed that the thermal resistance of the heat pipe lied between 0.46 to 2.28 ℃/W with methanol as the working fluid.

2.4 Knowledge Gap in Titanium Heat Pipes

Titanium and its alloys have been widely used as bone-implants. However, there is little research on their use in heat pipes, especially for space applications. Ti shows excellent compatibility with low temperature working fluids such as ammonia, which makes the material perfect to be used in outer space.

The unit cell approach in SLM is an advanced method to design porous structures since it can design the porosity and pore size before manufacturing. However, there is little research on the manufacturing of porous structures with pore size less than 60 μm, because of either the limit of the current achievable manufacturing parameters or the trade-off between the characteristics of the porous structure and the quality of the parts and the corresponding fluid and thermal properties. Capillary action becomes significant in the porous structure with such small pore size. In the meantime, it hinders the increase of permeability due to the increasing flow resistance. The factors

which have an influence on performance improvement have rarely been discussed. The influence of the characteristics of porous structures on the relevant fluid and thermal properties also needs to be further analysed.

Chapter 3

Methodology

This chapter describes the materials and methods employed to carry out the research project. The manufacturing equipment and the hardware used to create the porous structures are introduced first, followed by a detailed description of the porous octahedral structure. Finally, the equipment and methods used to characterise the structures and the permeability, capillary action, heat transfer coefficient of the porous structures are introduced.

3.1 Manufacturing Facilities

An MCP Realizer 250 (Realizer GmbH, Germany) machine based in The University of Liverpool and a Renishaw AM 250 (Renishaw, UK) based in Renishaw plc in Stone were used for commercially pure titanium (CpTi) and Ti-6Al-4V (Ti64) in this study, respectively. Both machines are equipped with the ytterbium fibre laser with a maximum laser output of 200 W and a continuous wavelength of 1.071 μm. The nominal beam diameter is 50 μm for Realizer 250 and 70 μm for AM 250. The thickness of each powder layer was controlled to be 50 μm for Realizer 250 and 30 μm for AM 250.

A schematic of the concept of the MCP Realizer 250 system is shown in Figure 3-1. The build area is 250x250 mm, and the optical configuration consists of a beam expander, scanning galvanometer, and F-theta assembly, allowing the movement of focussed laser spot with an accuracy of +/- 5 μm. The processing chamber operates in positive argon with low oxygen levels. The atmosphere within the chamber is circulated and filtered to remove process by-products such as particles formed from

condensed metal vapour and recycled gas. The operating software used is the bespoke MCP Realizers software.

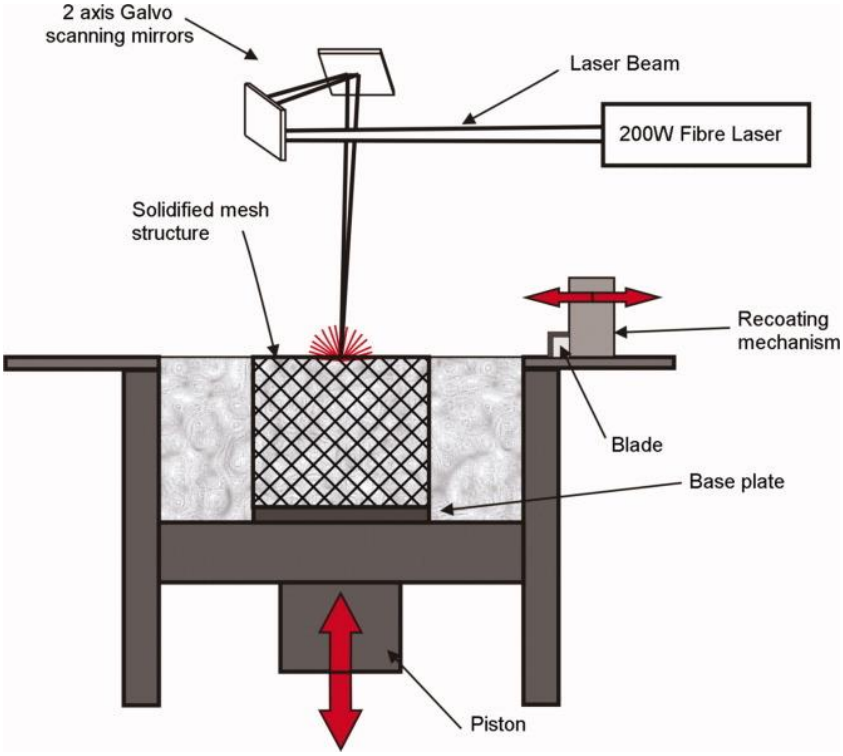

Figure 3- 1 Schematic of SLM system (Mullen et al., 2009a)

For both machines, there are external powder hoppers with valve interlocks to allow additional material to be added when the process is running. The main difference is the achievable height of sample, which is increased from 200 for MCP Realizer 250 to 300 mm for Renishaw AM 250. Once the first layer of powder is put onto the substrate, the laser beam scans the representative area described in a CAD file, and the wiper blade traverses the build area to produce a flat building plane and remove the excess powder. This process repeats until the final components are manufactured. The laser parameters used for the parts are controllable by the operator.

3.2 Operating procedures

A schematic of the operating procedure for the SLM process is displayed in Figure 3-2. It illustrates a complete process from a CAD drawing to the parts manufactured.

The details of the procedure are described as follows:

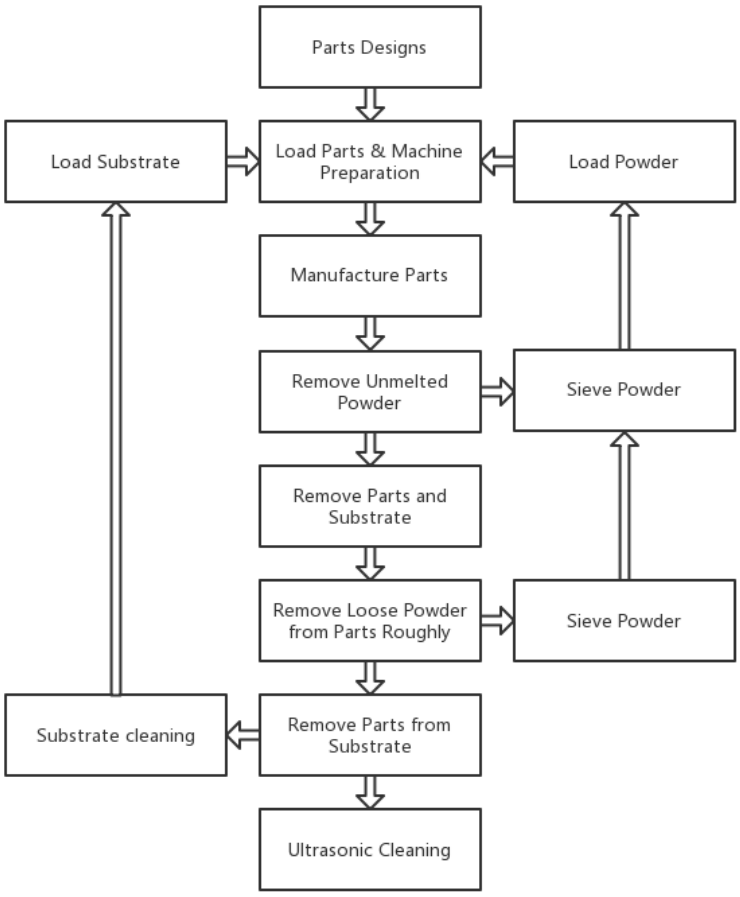

Figure 3- 2 Operating procedure for SLM process

Create Part Designs

PTC Creo Parametric (PTC, USA) was used to create and design the CAD models in this project. All surfaces were represented as a network of triangles to convert the CAD file to the STL file (Figure 3-3).

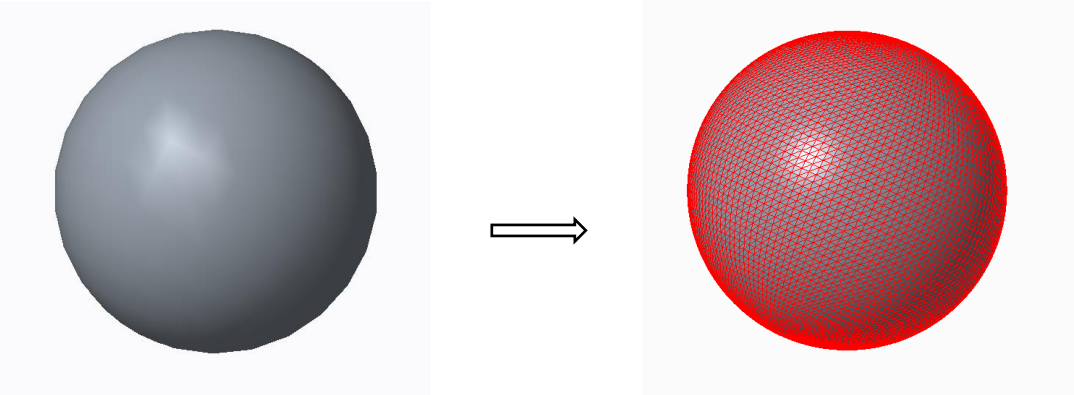

Figure 3- 3 Conversion of CAD model to STL format

Magics (Materialise, Belgium) was used for the preparation of CAD geometries before manufacturing. It was capable of adding support and slice files for the parts. If a porous structure was to be manufactured, the software Conformal Surface developed at the University of Liverpool was used to generate the porous structure with a defined unit cell size.

Load Parts and Machine Preparation

For the MCP Realizer 250 system, the part designs were loaded into the operating software in the STL file format. The files were then sliced in Realizer using an operator defined layer thickness. The laser parameters such as laser power and laser exposure time were also adjusted for different parts in the operating software. For the Renishaw AM 250 system, the software QuantAM (Renishaw, UK), which was designed specifically for Renishaw AM platforms, was used. It allows tighter integration into the machine control software and can accurately and rapidly review all build files for the Renishaw AM system. The laser parameters for each part can also be changed in this software.

The machine was evacuated to vacuum and then filled with argon. For the MCP Realizer 250, the processing chamber operated in a positive argon pressure of 14 mbar with oxygen levels kept between 0.1% - 0.2%. For the Renishaw AM 250 machine, a

vacuum of 35-50 mbar was created, and the chamber was then filled with 600 litres of high purity argon. The oxygen level was kept below 0.1%.

Load Substrate and Powder

Different substrates were selected for different materials. In order to ensure a strong bond between the substrate and the manufactured parts, the substrate was of the same or similar material to the powder being processed. The substrates need to have a smooth surface and uniform thickness, ensuring that an even powder layer thickness can be achieved for the first layers and a strong bond established between the part and the substrate.

All the powders were sieved and then loaded into the primary powder hopper. The powders had spherical metal particles with diameters less than 50 μm for the MCP Realizer 250 and less than 30μm for the Renishaw AM 250, respectively.

Manufacture Parts

The manufacturing process occurred under an argon environment to prevent any oxidation of the metal. The melting regime and the melt pool stability depend on the presence of oxides formed during the manufacturing process. The oxide films can be formed because the temperature of the melt pool is very high (Das, 2003). A thin oxide layer can be found on titanium alloy particles. It can be broken up and enters the melt pool. During melting both the titanium and its oxide are under the laser beam and liquid titanium oxide is not a barrier to liquid metal wetting of surrounding solid area.

Remove Unmelted Powder

The unmelted powder was removed by the wipe blade and collected by the powder hopper beneath the substrate. The powder was always under argon conditions, minimising the possibility of environmental contamination of the powder.

Remove Parts and Substrate

The parts, together with the substrate, were removed from the chamber once the manufacturing process was finished.

Remove Loose Powder from Parts

When porous structures are manufactured, it is important to remove loose powder from the parts since it affects further experimental results. The primary method used to remove most of the loose powder was using an impact vibration system, as shown in Figure 3-4. The substrate was held upon the powder container, and the loose powder was forced to fall by the vibration. The impact vibrator was attached to the underside of the substrate and moved clockwise to ensure as much powder as possible was removed. The removed powder was collected in the container for further sieving.

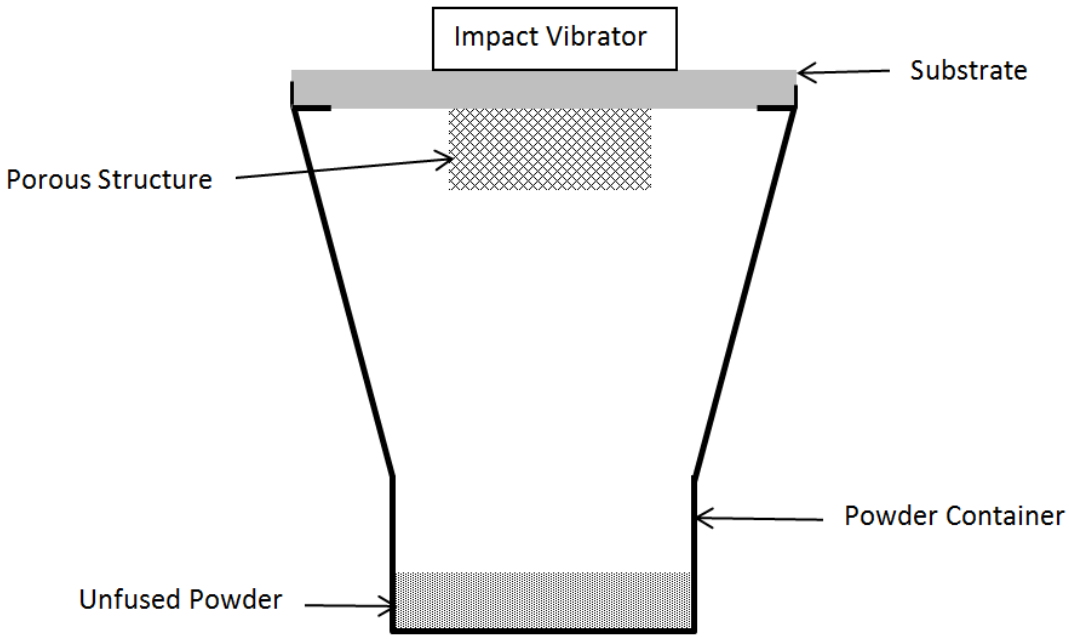

Figure 3- 4 Impact vibration system for removing loose powder in porous parts

Sieve Powder

Both the unfused powders collected from the manufacturing process and the impact vibration system were sieved again to remove any oversized powder particles or production debris. The sieved powder went into the hopper systems for the next manufacturing cycle, which helped to maintain powder consistency as it was repeatedly recycled.

Remove Parts from Substrate

Manufactured parts were removed from the substrate for further examinations. Typically, parts were built with supports so that the parts could be removed manually. Sometimes the parts were manufactured directly on the substrate, and Electrical Discharge Machine (EDM) wire cutting was used. EDM uses an electric discharge to erode conductive materials. A tiny amount of work material is melted and vaporized, which is then ejected and flushed away by the dielectric (Spedding and Wang, 1997). It is ideal for machining fragile metal materials, and high surface quality can be achieved from this process.

Substrate Cleaning

After the parts and supports were removed from the substrate, the substrate was reground before it was reused. Residual particles were cleaned carefully with ethanol.

Ultrasonic Cleaning

Although the impact vibrator removed the majority of powder particles, there might be residual unfused particles or contaminants introduced during EDM wire cutting or parts removal processes. Ultrasonic cleaning was performed in a VWR Ultrasonic bath USC-TH system (VWR, USA). The parts were immersed and cleaned in distilled water. For parts of similar or small sizes, they were separately put into different beakers for easier differentiation.

Usually, the process occurred at a temperature up to 60℃ to enhance the cleaning effect. The cleansing process lasted for 1 hour, and the cleaned parts were then dried naturally.

3.3 The Unit Cell Approach

A mathematical heat pipe model was developed to test the performance of porous structures. The model allows for the calculation of the height the fluid is lifted to under static conditions. Since the force and mass of fluid are known it is possible to find the mass flow rate of the fluid at any given time from Newton's second law. Steady state in a heat pipe occurs when the second time-derivative of the heat transfer is zero and as the heat transfer is dependent on the mass flow of fluid, the heat pipe is in equilibrium when the second time-derivative of fluid mass flow is zero.

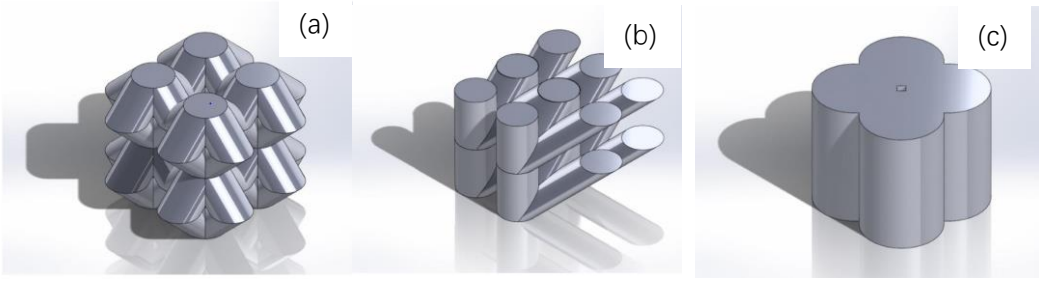

Figure 3- 5 (a) Octahedral wick structure; (b) bespoke wick structure; (c) rod wick structure

This model was used to analyse the octahedral, capillary and rod unit cell structures as shown in Figure 3-5. In order to measure the lift area and lift height of these unit cell structures, a 3D model was developed whereby the structure can be cut at any height to calculate the values. Examples of these cut sections are shown in Figure 3-6, where the solid material, the fluid channel and the border of the adjacent unit cells are represented by black, white and blue, respectively. The lift height can be predicted and calculated using Equation 2.11 based on the following hypotheses:

1. The capillary lift height equation applies to any combination of liquid and solid materials.
2. The force that a small collection of capillary section exhibits can be used to calculate a general bulk force for a larger number of similar capillary sections.
3. The capillary lift height equation can be applied to any type of section. From a geometric point of view, the total volume of a slanted cylinder of the same radius and vertical height as a non-slanted cylinder is equal to that of the non-slanted cylinder. It must be noted here that the height of the slanted cylinder is not the length of the cylinder as is typically applicable, but the vertical distance from base to top. It is beneficial to define a slanted cylinder as one in which the top and bottom are not perpendicular to the length of the cylinder. It is, however, clear that a slanted cylinder will have a longer liquid surface-solid interface and hence experience a higher lift force.

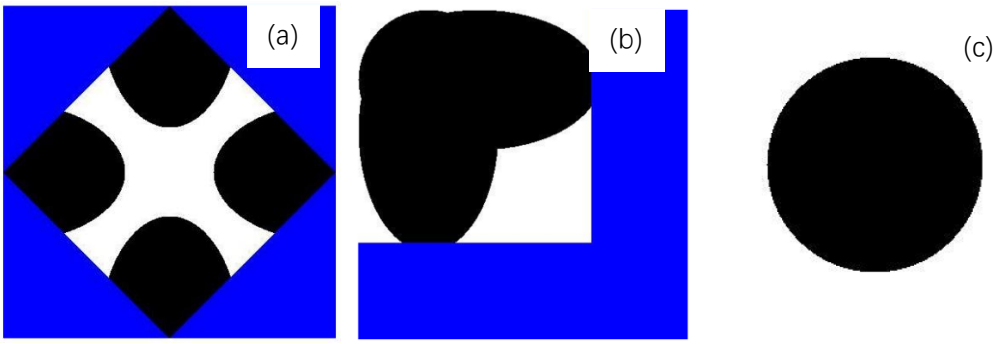

Figure 3- 6 Cross sections of (a) octahedral structure; (b) bespoke structure; (c) rod structure

It was calculated that the octahedral unit cell can lift any proposed working fluids to the required height when the unit cells are smaller than 260 µm. The bespoke capillary wick structure can lift to the required height with unit cell sizes of 180 to 240 µm for all fluid candidates. The rod structure can lift to the required height for all fluids when

the unit cell size is smaller than 160 μm. The resolution of the SLM machines would not allow unit cells of small size to be built without the part being completely solid and therefore not able to transport fluid. Based on this reason and the complete pore interconnectivity, the octahedral unit cell was selected in the study.

The octahedral unit cell is a porous structure developed by the University of Liverpool. The detailed approach was described in (Mullen et al., 2009). The software Conformal Surface developed at the University was used to generate the structure automatically. The structure and a simple example of an octahedral porous structure are shown in Figure 3-7.

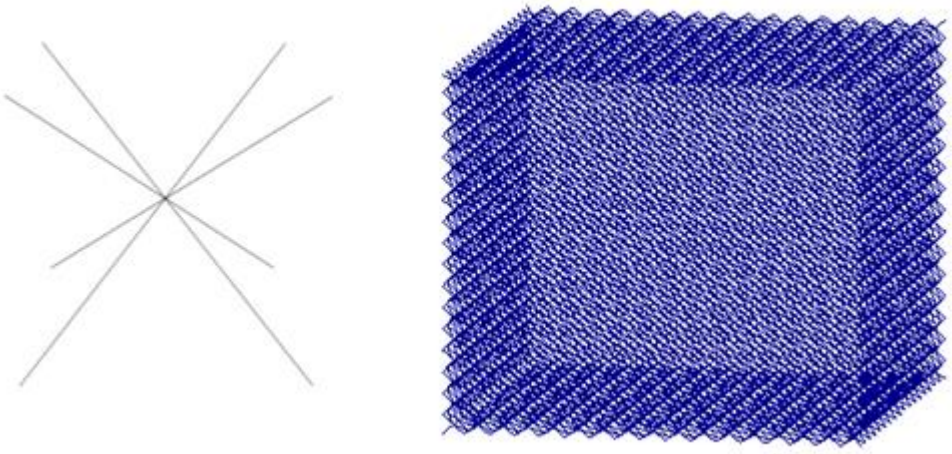

Figure 3- 7 Single octahedral unit cell (Mullen et al., 2009a) and an example of a porous cube

The octahedral structure was modelled with a varying unit cell size for four proposed working fluids, which are suitable for heat pipes operated under low temperatures. As the working fluid properties are temperature dependent, data are presented for two cases: the minimum operating temperature of -35 ℃ and maximum operating temperature of 120 ℃. The calculated lift heights for each unit size are outlined in

Table 3- 1.

The octahedral unit cells equal to or smaller than 300 μm would be able to lift any of the proposed working fluids to the required height in this project under both temperatures. However, the resolution of the SLM machines may not allow unit cells of these sizes to be built without the part being completely solid and, therefore, not able to transport fluid. Therefore, different laser parameters need to be used and analysed for each unit cell, especially for the small unit cells to find out the optimum condition.

Table 3- 1 Octahedral unit cell lift height at left: 0 ℃; right: -35 ℃

Unit Cell Size, U, μm	Lift Height, h, mm			
	Acetone	Ammonia	Methanol	Pyridine
260	263.8	267.9	258.0	302.9
280	253.7	264.5	246.5	296.9
300	202.0	221.9	193.8	245.4
320	149.3	169.2	142.6	185.1
340	112.7	127.7	107.6	139.7
360	89.9	101.9	85.9	111.5
380	74.3	84.2	71.0	92.1
400	63.2	71.6	60.3	78.3
420	54.5	61.7	52.0	67.6
440	47.7	54.1	45.6	59.2
460	42.3	48.0	40.4	52.5
480	37.9	42.9	36.2	46.9
500	34.1	38.7	32.6	42.3

Unit Cell Size, U, μm	Lift Height, h, mm			
	Acetone	Ammonia	Methanol	Pyridine
260	280.7	309.8	282.9	318.4
280	273.3	314.5	276.7	315.1
300	223.0	278.4	227.8	265.4
320	166.8	224.7	171.3	203.0
340	125.9	170.2	129.3	153.3
360	100.0	135.8	103.2	122.3
380	83.0	112.3	85.3	101.1
400	70.6	95.4	72.5	85.9
420	60.1	82.3	62.5	74.1
440	53.3	72.1	54.8	64.9
460	47.2	63.9	48.6	57.6
480	42.3	57.2	43.4	51.5
500	38.1	51.6	39.2	46.4

Seven unit cell sizes, 250, 275, 300, 350, 400, 450 and, 500 μm, were studied for CpTi and four unit cell sizes, 300, 350, 400, 450 μm were studied for Ti64.

3.4 Materials

SLM can work with many materials, including metal, ceramic, and composite materials. One of the aims of this project is to manufacture heat pipes for space applications. They need to be lightweight since if the weight increases, the cost of the launching is increased. In the beginning, aluminium and its alloys were selected to be the materials due to their suitable mechanical and thermal properties, lightweight,

availability, and wide acceptability as structural materials in the automobile and aerospace industries. However, as described in the previous chapter, it is tough to manufacture solid parts with a density of 100% in aluminium using SLM with current machines. It is very dangerous if pores or cracks are existing in the solid wall of a heat pipe because the vapour pressure within the chamber may break the wall, or the leakage from working fluid may occur in the operating situation. According to Schleifenbaum et al. (2010), high laser power is necessary to achieve parts with mechanical properties comparable with those of cast wrought components, with 330W being necessary to manufacture high-quality aluminium components. Furthermore, the processing of aluminium and its alloys in poorly controlled atmospheres has shown a tendency for the melt pool to ball or for powder particles to fail to incorporate into the melt pool (Olakanmi et al., 2009). These limitations and the necessity of more expensive, higher power laser have imposed a restriction on the use of aluminium and its alloys with SLM. Therefore, titanium and its alloys were proposed as alternative materials for the project.

CpTi and Ti64 are widely used in dental implants and osseointegration due to the superior strength to weight ratio, corrosion resistance and the full biocompatibility. The density of the parts manufactured by SLM in CpTi and Ti64 can approach 100%. All these advantages make titanium and its alloys possible for use in heat pipe applications.

The details of the CpTi and Ti64 powders are given in Table 3-2. Two scanning strategies were used for the CpTi and Ti64 powders in the MCP and Renishaw systems, respectively.

Table 3- 2 The Ti64 and CpTi powders used in this study

Material	Commercially Pure Titanium	Ti6Al4V
Manufacturer	Sumitomo	Renishaw
Powder Diameter, *d*, µm	<30	<45
Thermal Conductivity, -, W/m.K	20.4	8
Reflectivity, -, %	55	-
Density, *ρ*, Kg/m^3	4500	4500
Melting Point, *T*, ℃	1668	1665

3.5 Characterisation of Porous Structures

Laser power and laser exposure time were varied in this study. The porosity and pore size of the porous structures as manufactured were measured. The relationship between the laser parameters and the characteristics of the porous structures was studied. The methods used to measure porosity and pore size are described below.

3.5.1 Porosity

Porosity reflects the volume of voids existing in the porous structure. For an open-cell porous structure, porosity reflects the accessible space and has a significant influence on the flow rate passing through the porous structure. The geometry of the samples used for porosity testing was cuboids, 300 mm in length, 20 mm in width, and 5mm in height, as shown in Figure 3-8. These samples were also used for pore size and permeability measurements.

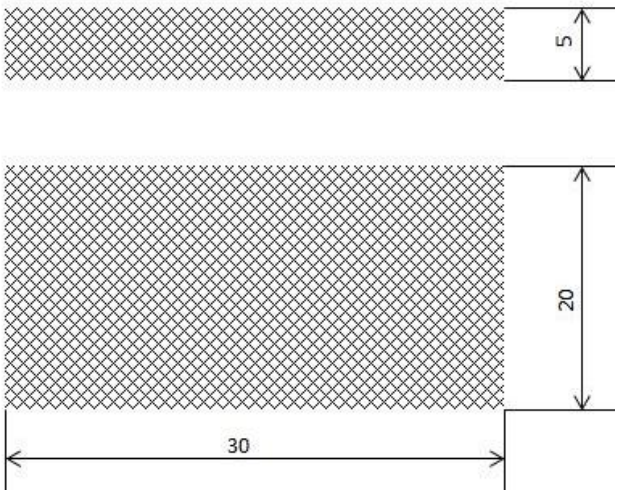

Figure 3- 8 The porous parts for porosity, pore size, permeability and heat transfer testing

The porosity was determined by the sample's mass in air and the sample's mass when suspended in water using the following equation:

$$\varphi = \frac{\rho_w m_{dry}}{\rho(m_{dry} - m_{wet})} \quad \text{(Equation 3-1)}$$

where m_{dry} is the mass of the dry sample; m_{wet} is the mass of the sample immersed in water; ρ is the density of the metal used for making the sample; and ρ_w is density of water.

A Sartorius balance (Sartorius, UK) was used to measure mass, to an accuracy of 0.0001 g. The measurement was repeated four times for each sample, and the average was taken.

3.5.2 Pore Size

The pore size was analysed by photogrammetry, following the method described by Evans et al. (2017). Firstly, a Wild Heerbrugg Microscopy (Wild Heerbrugg, Switzerland) was used to take a photo of the surface of the part. The software Image J was then used for image processing. Local thickness measurements were made to determine the distribution of pore size in the porous structure. This technique was able

to calculate the diameters of the pores within the porous structure. The measurements required several distinct steps to complete the analysis, which is shown in Figure 3-9 as an example.

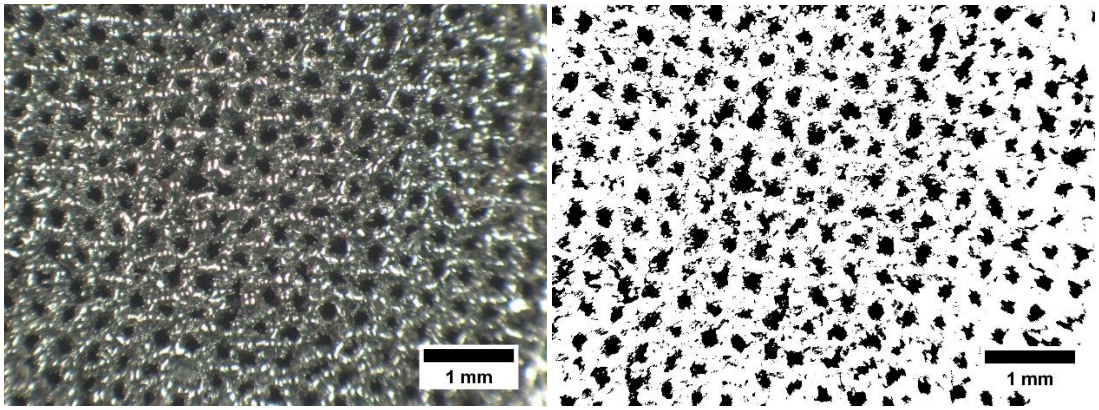

Figure 3- 9 500 µm unit cell CpTi structure captured by microscopy (left) and the converted image using a threshold to binary

Initially, a distance map was produced, in which each pixel was assigned a value equal to the Euclidian distance from that pixel to a white pixel, which represents a solid part in Figure 3-10 (Dougherty and Kunzelmann, 2007, Hildebrand and Rüegsegger, 1997). A distance ridge formed from the highest values in the distance map was then created. The centres of the pores, i.e. the structures formed from black pixels, were located. From each pixel in the distance ridge, a circle was expanded until its circumference encountered a white pixel. The diameter of the circle corresponded to the diameter of the pore at that point along the ridge (Dougherty and Kunzelmann, 2007). The local thickness was determined using Equation 3-2 where $\tau(\underline{p})$ is the mean thickness, $D_{map}(\underline{q})$ represents the distance map and $\underline{p}$ and $\underline{q}$ represent points just inside and on the perimeter of the structure, respectively (Hildebrand and Rüegsegger, 1997).

$$\tau(\underline{p}) = 2 \cdot \max_{\underline{q} \in X(\underline{p})} (D_{map}(\underline{q})) \qquad \text{(Equation 3-2)}$$

The set $X(\underline{p})$, shown in Equation (3-3), represents the centre points of all circles with

a radius equal to the value of the distance map at that point, contained within the set Ω_R, the pixels in the distance ridge of the structure, and including point $\underline{p}$.

$$\widetilde{X}(\underline{p}) = \{\underline{x} \in \Omega_R | \underline{p} \in sph(\underline{x}, D_{map}(\underline{x}))\} \quad \text{(Equation 3-3)}$$

It is used to specify which pixels in set $\underline{p}$ should be used as points of measuring local thickness by the placement of a circle, primarily to reduce the computational time (Hildebrand and Rüegsegger, 1997). The output of the local thickness analysis of pores is shown in Figure 3-10.

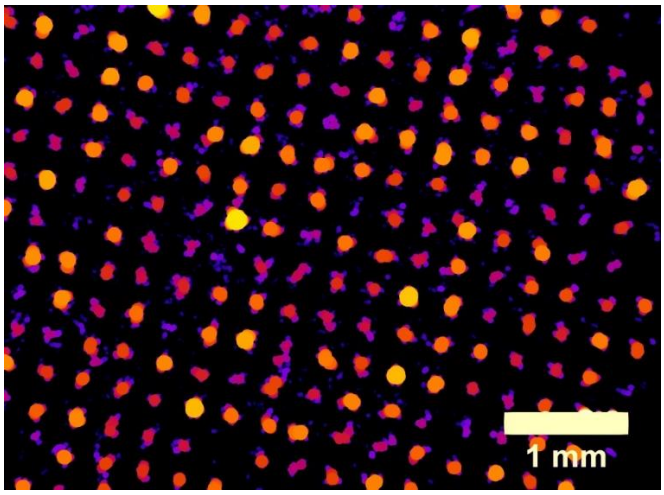

Figure 3- 10 Output of local thickness analysis of pores for 500 µm unit cell CpTi structure

From this analysis, a histogram showing the distribution of pore size was produced (Figure 3-11). This histogram shows the value of each measurement taken and the frequency by which each value occurred.

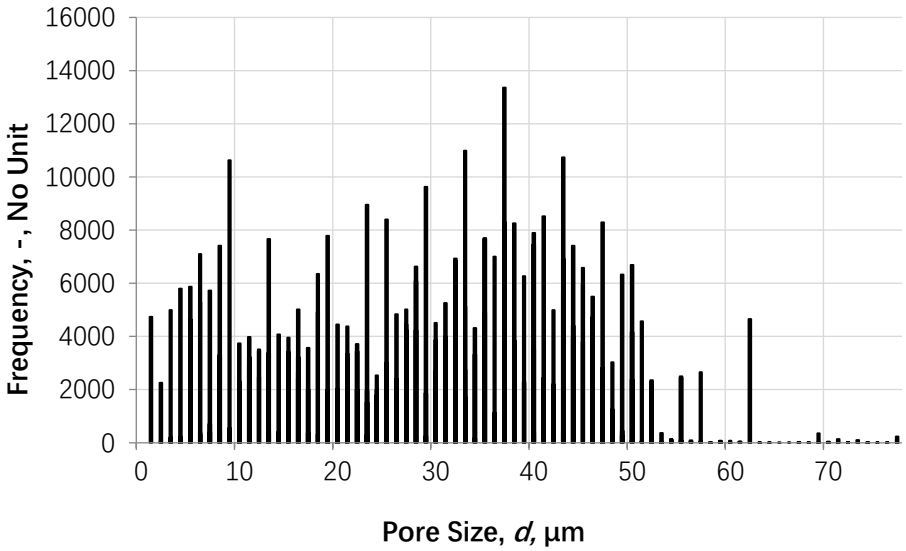

Figure 3- 11 Histogram showing the pore size distribution for 500 µm unit cell CpTi structure

This method produced good quantitative results with a mean error of 2.7 µm for measurements between 63 and 208 µm. The accuracy decreased when the examined pore size became smaller (Evans et al., 2017). Typically, the pore size results appeared to be bimodal, because two kinds of pores exist in the structure, as shown in Figure 3-12. In this study, the interconnecting pores were used to determine the pore size of the structure, as they form the easiest path for fluid to pass through.

According to the calculation by (Dan, 2011), the diameter of the interconnecting pores is the diameter of the cylinder which can pass through the interconnecting space of adjoining octahedra, and can be expressed as:

$$d = \left[2\left(\frac{a}{\sqrt{8}}\right)\right] - s \qquad \text{(Equation 3-4)}$$

where a is the unit cell size and s is the strut thickness. The measured strut thicknesses for all the CpTi samples are listed in Table 4-2.

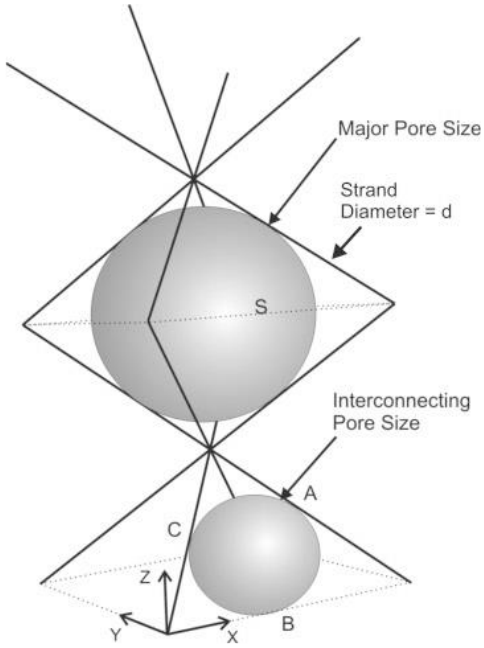

Figure 3-12 Schematic of major and interconnected pores in an octahedral porous structure (Mullen et al., 2009b)

3.6 Fluid and Thermal Properties

Once the porosity and pore size were measured, the measurements of relevant fluid and thermal properties were followed. In this study, the permeability, capillary force, and thermal transfer coefficient for varying porous structures were measured, and the used methods are detailed below.

3.6.1 Permeability

Permeability reflects the ability of how easy a fluid can pass through the porous media. In order to ensure that a certain quantity of gas or liquid can be transferred through the wick structure, the permeability of the porous structure needs to be tested.

A forced water flow apparatus, as shown in Figure 3-13, was used for the permeability measurements. The water flowed through a filter, a ball valve, an input pressure transducer, the porous sample contained in the sample holder, an output pressure transducer and a flowmeter. The input and output pressures were measured by ruggedized pressure transmitters (OMEGA, USA). The flow rate was measured using

a panel mount flowmeter (OMEGA, USA) with an accuracy of ±5%. The sample holder was made of polytetrafluoroethylene (PTFE), and the flow channel through the sample holder was 20 mm wide and 5 mm high. All the test instruments were properly mounted on the sample holder. The signals of pressure and temperature were logged by a computer and recorded using the software InstrNet (Instrument, UK).

The specimens used had a cuboid geometry, 30 mm in length, 20 mm in width and, 5 mm in height. There were no solid walls for these samples because the wall of the rig is rigid, and there was no leakage between the sample and the wall.

The fluid flux was varied from 0.1-2.0 L/min and the pressure drops were measured. In this flow regime, the calculated Reynolds number was more than 10, sometimes even more than 50. The inertial force may have a dominant influence and the flow can transform from laminar flow to turbulence flow. Therefore, the intrinsic permeability was calculated using the Forchheimer's equation:

$$\frac{\Delta P}{L} = \frac{P_{in} - P_{out}}{L} = \frac{\mu}{K} V + \rho C V^2 \qquad \text{(Equation 3-5)}$$

where V is Darcy velocity, K is the permeability of the porous medium, μ is the viscosity of the fluid, P_{in} and P_{out} are inlet and outlet pressure, respectively, $\triangle P$ is the fluid pressure drop, L is the length of the porous medium, ρ is the density of the fluid and C is the form drag coefficient.

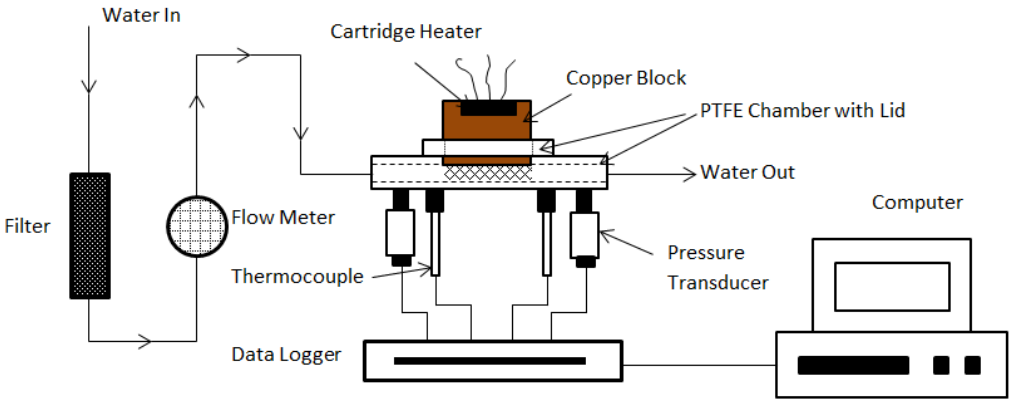

Figure 3- 13 Schematic diagrams of forced water flow and heat transfer apparatus

3.6.2 Capillary Action

Capillary action of the porous structures is described by the lift height against the gravity in a specific time, which was measured using a porous tube as shown in Figure 3-14. The height-time method and weight-time method were used simultaneously and the results from both methods were compared. The apparatus used to measure the lift height test of the porous structure is shown schematically in Figure 3-15.

Figure 3- 14 Drawing of the porous tube made for capillary force testing

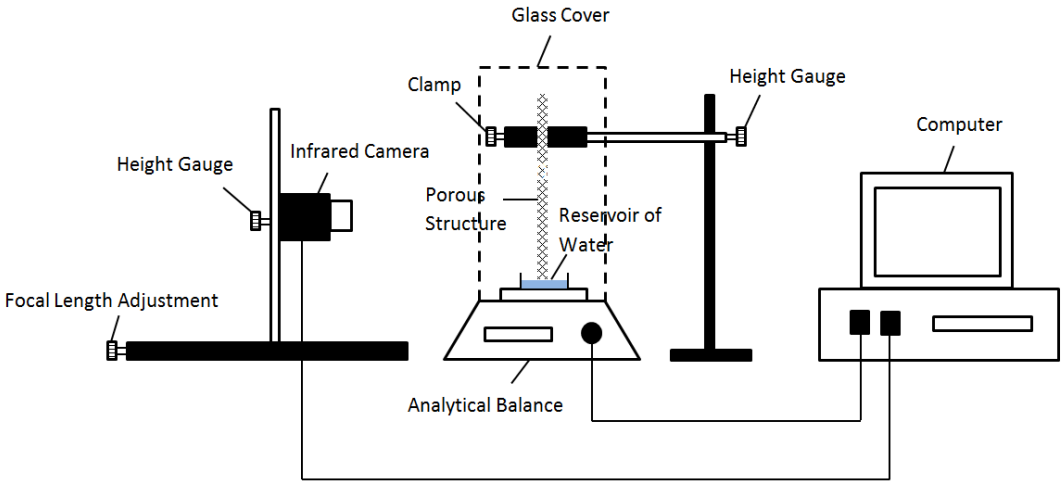

Figure 3- 15 Diagram of the lift height test

In the measurements, distilled water was used as the working fluid and the room temperature was kept at 20℃ by an air conditioner. A Tamarisk 640 infrared camera (DRS Technologies, US) was used to capture and locate the water level change during lift height testing. The camera is a vanadium oxide-based long-wave infrared video camera with a 17 μm pixel pitch 640x480 microbolometer detector, and it is sensitive to thermal radiation emissions from 8 – 14 μm. The camera was controlled by the software, DRS Camera Control Software (DRS Technologies, USA) and Framelink Express (Inperx, USA), and the sample was photographed every 5 seconds, with the images saved automatically. A Nimbus analytical balance (Adam Equipment, UK) with a readability of 0.0001 g and a repeatability of 0.0002 g was used to record the weight change of absorbed water. It was connected to a computer and the data was recorded automatically by the software AdamDu (Adam Equipment, UK) every 5 seconds.

During the test, one end of the porous wick structure was dipped into the distilled water, the IR camera captured the increasing meniscus, and the balance recorded the weight change of water until the pressure on both sides of the meniscus equilibrated.

In the earlier measurements, it was found that the weight kept changing after 1 hour even the IR images showed that the water level was not changing anymore. Water evaporation from the petri dish and the sample surface was identified to be the factor affecting the weight results. In order to eliminate this effect, the evaporation rate from the petri dish was determined. Specifically, a petri dish of distilled water was put on the balance under room temperature for 1 hour and the weight change was recorded every 5 seconds. The average evaporation rate was calculated to be 0.17mg/s. In later measurements, the sample was wrapped by a PVC film, preventing any evaporation from the surface. The wieght change data was modified by removing the evaporation from the petri dish, as shown in Figure 3-16. It was found that the sample was fully saturated after about one hour.

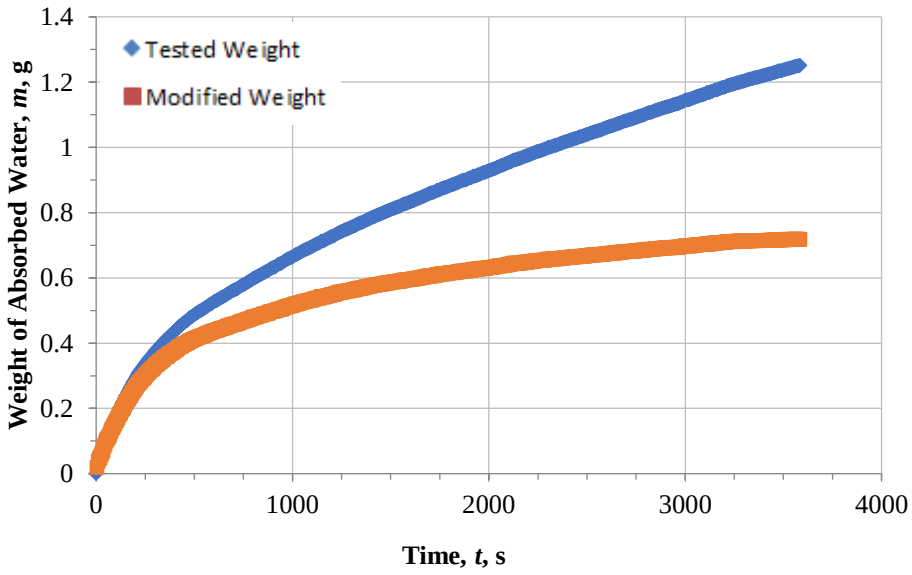

Figure 3- 16 Tested and modified weight changes of absorbed water in 500 μm unit cell size CpTi structure

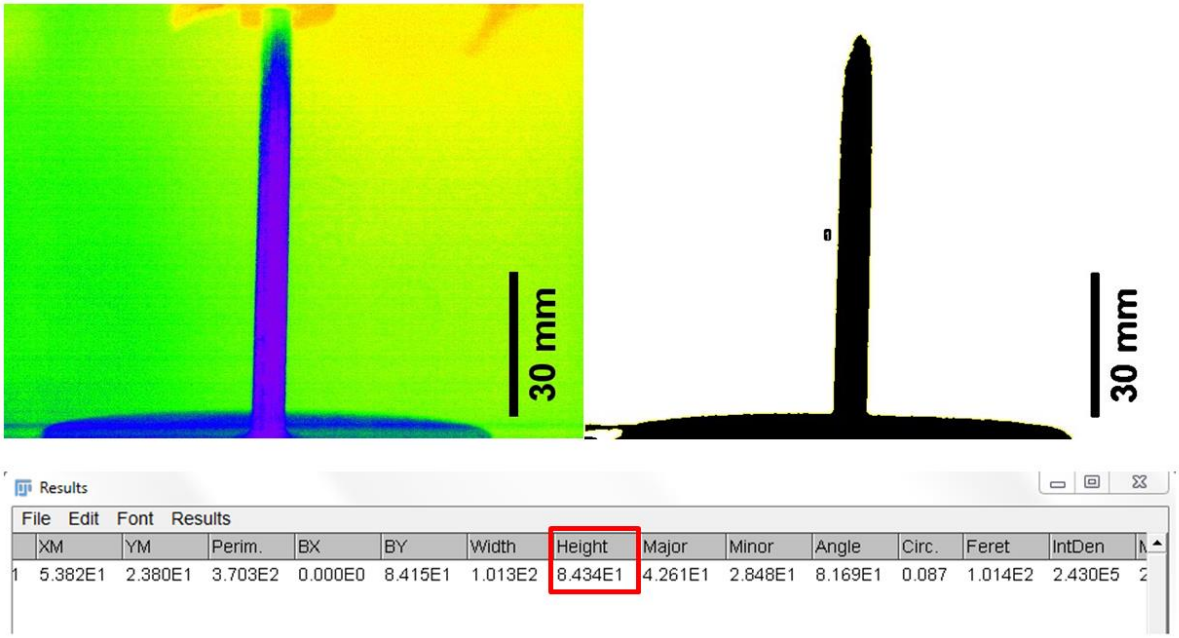

Figure 3- 17 IR image analysed by ImageJ (400 µm unit cell size CpTi structure)

The height of the water in the selected part of the sample was measured automatically using ImageJ, as shown in Figure 3-17. The lift height for each sample was also calculated from the weight change as follows:

$$h = \frac{m}{\rho\,\pi\,(R^2 - r^2)\varphi} \qquad \text{(Equation 3-6)}$$

where h is the lift height in the porous structure, m is the mass change over time, ρ is the density of water, R is the outer diameter of the sample, r is the inner diameter of the sample, and ε is the porosity of the sample.

Although the final choice of working fluid in the project is ammonia, water was used in the lift height tests instead. This is because ammonia is poisonous and corrosive to the human body, so it is not easy to handle ammonia in the lift height testing. Ammonia has a lower density (730 kg/m^3) than water (997 kg/m^3) at room temperature and a similar intermolecular force (hydrogen bonding) to water. Theoretically the lift height of ammonia should be higher than that of water in a heat pipe, according to Equation 2.11.

3.6.3 Heat transfer

The heat transfer performance of the porous structures was investigated under forced convection cooling using water as the coolant. The samples and the apparatus used for the measurements were the same as those for permeability testing, as illustrated previously in Figures 3-8 and 3-13. A copper block with a thermal conductivity of 391 W/mK was put onto the sample, with the bottom of the copper block attached tightly to the surface of the sample during the experiment. In order to minimise heat loss, the copper block was surrounded by cotton and PTFE. The block was heated using eight FIREROD cartridge heaters (Watlow, USA), which can deliver a maximum total input power of 0.8 KW. The heaters were controlled by a variac so that various input power could be selected in the experiment.

When the copper block was heated, the heat was conducted through the copper to the porous sample and dissipated due to convection caused by the coolant flowing through the sample. Two thermocouples were used to measure the difference in temperature between the top and bottom of the copper block. Two thermometers with an accuracy of ±0.1 K were used to record the temperatures of the coolant flowing in and out of the sample. The software InstrNet (Instrument, UK) was used to record the change of temperature over time.

The power input was controlled to be 85 W/m^2. The range of flow rate was between 0.1 to 1.5 L/min. It usually took half an hour to achieve a steady-state in temperature for each flow rate.

Because heat passes through the copper block by conduction, assuming no heat loss in this process, the heat flux can be calculated using the temperature gradient along the conduction direction according to Fourier's law:

$$Q = CA\frac{T_t - T_b}{L} \qquad \text{(Equation 3-7)}$$

where C is the heat conductivity of the copper block (391 W/mK), A is the cross-sectional area of the heating block (5.985 x 10^{-4} m^2), T_t is the temperature of the block at the top, T_b is the temperature of the block at the bottom, and L is the distance between T_t and T_b(80 mm).

Once the heat is transferred to the porous sample, the convective heat flow is generated due to the coolant flowing through the structure. The overall heat transfer rate for the porous structure can be expressed in terms of the heat transfer coefficient, and can be described as follows:

$$Q = hA(T_b - T_{in}) \qquad \text{(Equation 3-8)}$$

where Q is the heat flow to the coolant, h is the heat transfer coefficient of the sample, A is the interfacial area between the solid and the coolant and T_{in} is the temperature of the fluid.

Combining Equations 3-7 and 3-8, the heat transfer coefficient, h, can be calculated by:

$$h = \frac{C\,(T_t - T_b)}{L\,(T_b - T_{in})} \qquad \text{(Equation 3-9)}$$

3.6.4 Selection of Pore Size

This project aims to design and manufacture a heat pipe which can work against gravity under low temperature. The selection of the porous structure is based on the requirement of the fluid and thermal properties for a space application. As discussed in Chapter 2.3, the permeability and heat transport capability of wick structure increase with increasing pore size, whereas the capillary lift height decreases with increasing pore size. Therefore, it is important to find out an optimum pore size range that can satisfy all the requirements in this project, which are:

(3) lift height of 20 cm against gravity.

(4) permeability in the range of 10^{-10} to 10^{-12} m^2.

(5) heat transport capability up to 30 W at the maximum operating temperature.

It was estimated that the pore size of the final porous structure should be smaller than 60 μm, as illustrated schematically in Figure 3-18.

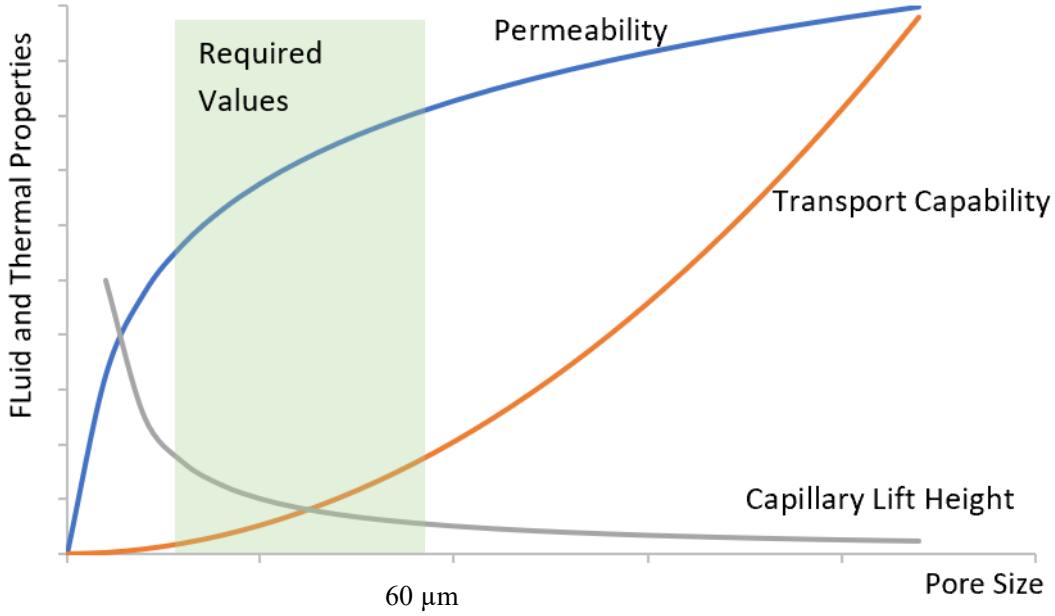

Figure 3- 18 Selection of pore size with required fluid and thermal properties

3.7 Uncertainty Analysis

The uncertainty of each experiment in this study was calculated using the standard error analysis method, the root of the sum of the squares method (Moffat, 1988). The accuracies of the caliper, the precision balance, the flowmeter, the presure transducers and the thermometers, used for the dimensional, mass, flow rate, pressure and temperature measurements are ± 0.1 mm, 10^{-4} g, ± 0.1 L/min, ± 0.25 Bar and ± 0.1 K, respectively. The uncertainty of porosity measurements depends on the measurement accuracies of mass and the length, width, and height of the sample, and was calculated to be 0.25%. The uncertainty of permeability depends on measurement acuracies of

the cross-section of the sample, flow rate and pressure drop, and was calculated to be less than 9.5%. The maximum uncertainties of the capillary lift height tests were calculated to be 7.1% and 4.2% for the height and weight measurements, respectively. The uncertainty for the heat transfer coefficient measurements depends on the cross-section of the sample and the temperature difference, and was calculated to be less than 3.1%.

Chapter 4

Development of Porous Structures Based on Unit Cell Size

Porous materials are widely used in heat transfer devices because the highly connected pores allow fluids to pass through them easily. Heat transfer performance can be improved by the tortuous shape of the structure and the high permeability. Porous structures play an essential role in heat pipe applications, especially when an against-gravity operating situation is required. Highly porous, open-celled geometries can provide space for the working fluid to pass through, and capillary force generated by the porous structure can lift the working fluid with an angle or vertically. The capillary action can be improved by decreasing the pore size of the structure. Additionally, the contact angle between the working fluid and the pipe material, the operating temperature, and the working angle can also affect the capillary performance.

There are many advantages of using SLM to produce porous structures, such as high material utilisation and capability of manufacturing intricate geometries. The porous structure can be designed and modified depending on the different requirements of specific applications. The porous structures used in this study are based on the unit cell approach described in Chapter 2. It was found that the most favourable candidate cell geometry for use in this heat pipe application consists of octahedral unit cells due to the following reasons:

- The octahedral structure can theoretically avoid the overhanging surface with a small inclined angle, thus avoiding the defects of hanging dross and pore blockage during manufacturing (Wang et al., 2012).
- It is calculated that an octahedral unit cell smaller than 300 μm can lift any of the proposed working fluids in this project to a specified height of 200-mm.
- The "pores" in the structures are designed to be open and interconnected, which is essential for permeability and heat transfer performance, and the characteristics of the porous structures can be tailored.

This chapter investigates the relationship between the characteristics of the porous structures and the laser parameters.

4.1 Manufacture of Unit Cell Structures in Commercially Pure Titanium (CpTi)

In this study, CpTi was used firstly in the MCP Realizer system. In order to identify the optimum structures for heat pipe application, a range of laser powers and laser exposure times were used to analyse the relationship between the laser parameters and the characteristics of the manufactured structures. According to the research by Yasa and Kruth (2011), the densities and surface roughness of the parts can be improved by laser re-melting by removing pores formed between neighbouring melt pools in the borders. The ability of permeability and capillary force can be affected by the roughness due to extra channels with small pores according to the research by Thompson et al. (2015). Therefore, double exposure scanning was also used to see whether the surface quality of the samples can be improved. In double exposure scanning, each layer was scanned by the laser twice.

The micrographs in Figure 4-1 show the surfaces of two CpTi 250 μm samples with extremely short and long exposure times.

The micrographs in Figure 4-1 show the surfaces of two CpTi 250 µm samples with extremely short and long exposure times.

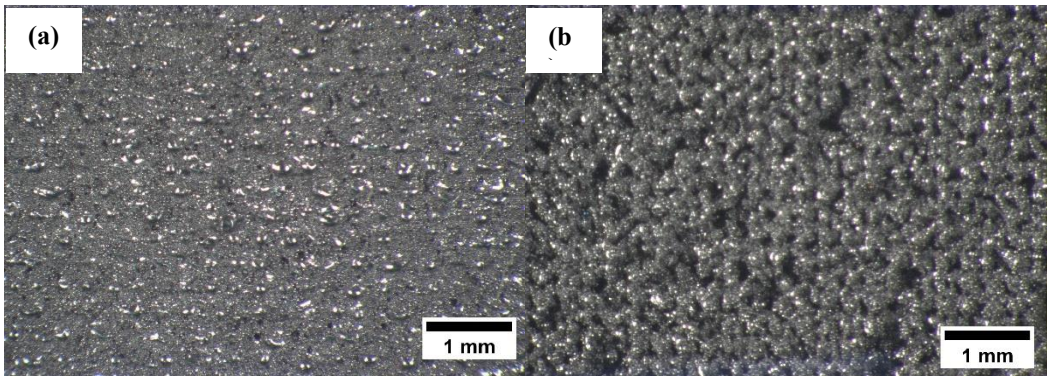

Figure 4- 1 Micrographs of the surfaces of CpTi 250 µm samples: (a) power 83 W, exposure time 410 µs; (b) power 83 W, exposure time 40 µs

Both do not display a clear and consistent porous structure. The part is dense with most of the pores inside the structure blocked when the laser exposure time is too long, whereas the structure with insufficient laser exposure is defective.

Seven unit cell sizes were used to manufacture the samples with a power of 83 W and exposure time between 20 to 410 µs. One sample was selected for each of the processing conditions given in Table 4-1.

Table 4- 1 Laser processing conditions used for the optimisation of CpTi porous structures

Scanning Strategy	Unit Cell Size, *U*, µm	Laser Power, *P*, W	Exposure Time, *t*, µs
Single Exposure	250	83	20
	275	83	40
	300	83	200
	350	83	200
	400	83	410
	450	83	410
	500	83	410
Double Exposure	450	83	410
	500	83	410
	550	83	410
	600	83	410
	650	83	410

4.1.1 Porosity and Pore Size

Figures 4-2 shows the SEM images of the 500 μm unit cell structures manufactured with single exposure scanning and double exposure scanning. The strand diameter increases when the laser process is repeated for each layer. The sintered attachments to the strut also increase due to the double laser scanning. The strut diameter for all single and double scanning samples were measured and shown in Table 4-2.

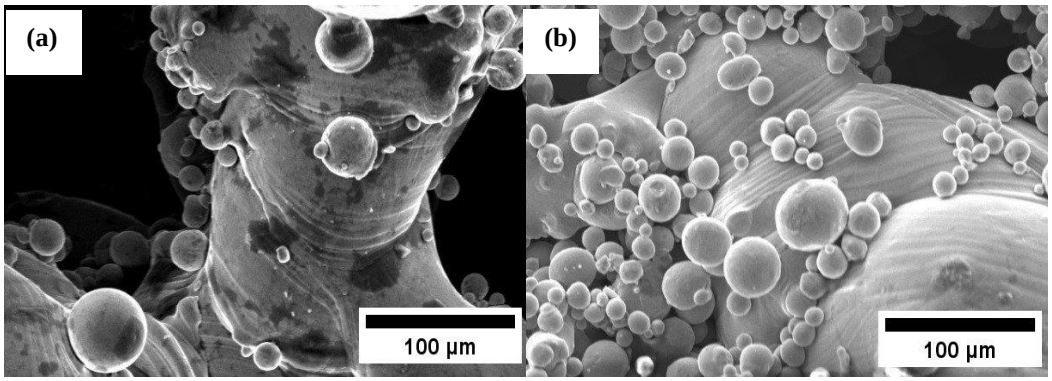

Figure 4- 2 SEM images of 500 μm unit cell size samples: (a) single exposure; (b) double exposure

The pore size was measured using the method described in Chapter 3, and the average pore size distribution of porous structures manufactured using single exposure scanning is shown in Figure 4-3. It is shown that the peak pore size increases when a larger unit cell size was used.

Figures 4-4 and 4-5 show the experimental and theoretical pore sizes for single and double exposure unit cell structures respectively. The experimental pore size increases with the unit cell size, and the ranges of pore size of 30-171 μm and 78-166 μm for single exposure scanning and double exposure scanning, respectively, were achieved with the SLM manufacturing process.

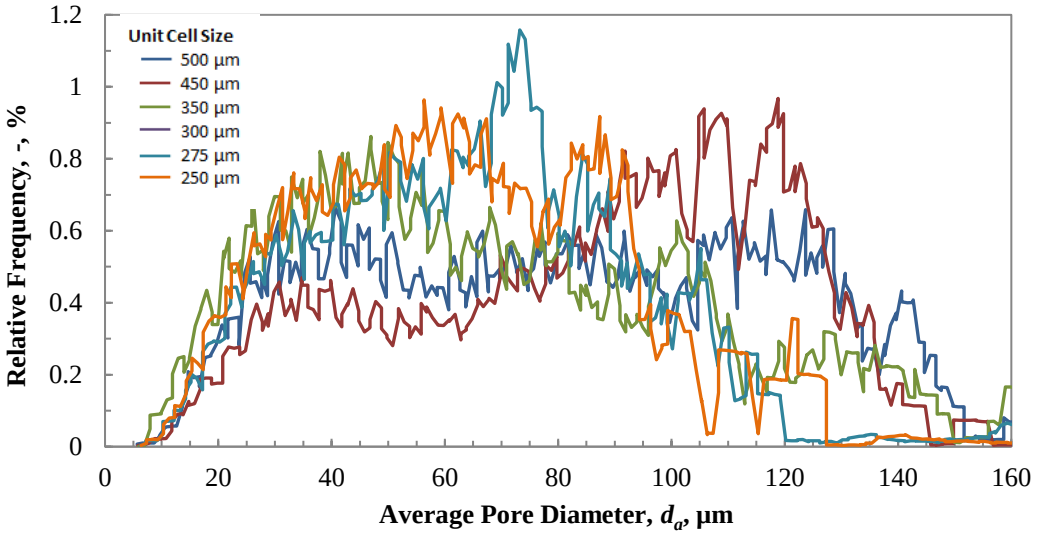

Figure 4- 1 Pore size distribution of single exposure CpTi samples

Table 4- 2 Average strand diameter for varying CpTi unit cells and different laser strategies

Scanning Strategy	Unit Cell Size, *U*, µm	Strand Diameter, *s* µm
Single Exposure	250	-
	275	-
	300	129
	350	129
	400	188
	450	193
	500	185
Double Exposure	450	285
	500	281
	550	278
	600	276
	650	275

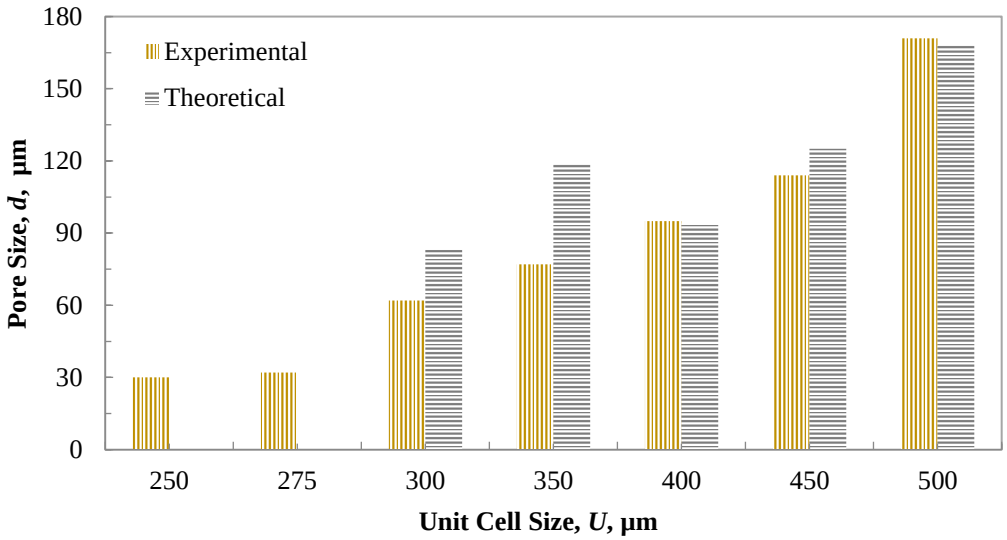

Figure 4- 4 Variation of pore size with unit cell size for samples manufactured with single exposure scanning

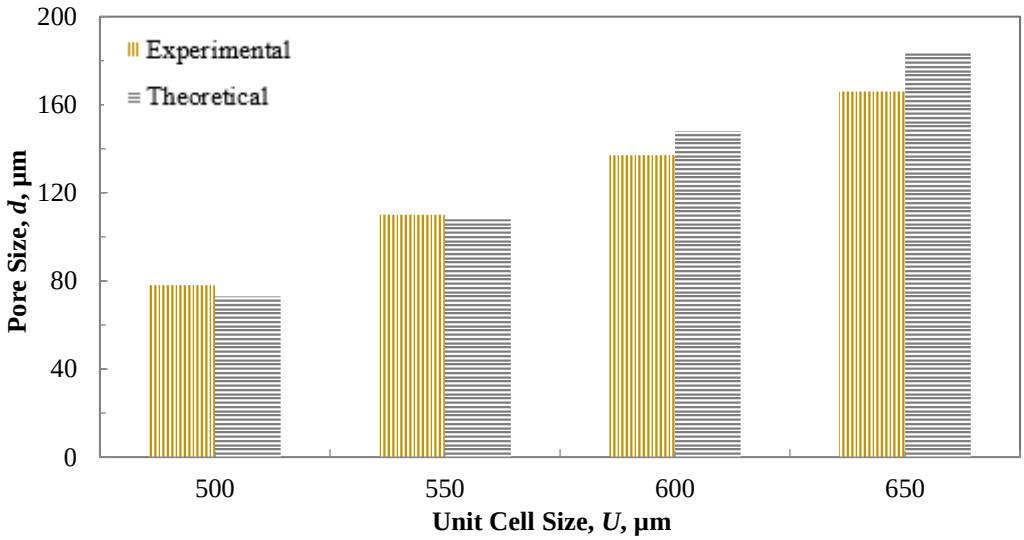

Figure 4- 5 Variation of pore size with unit cell size for samples manufactured with double exposure scanning

The porosity values of the structures were obtained using the Archimedes' method described in Chapter 3. Figure 4-6 shows the changes of porosity with unit cell size for samples manufactured with single exposure scanning, with the same laser power. It is shown that the porosity increases with the unit cell size, and a range of porosity between 25.9% and 54.2% can be obtained. Figure 4-7 shows the changes of porosity

with unit cell size for samples manufactured with double exposure scanning, with the same laser power and exposure time. Again, the porosity increases with increasing unit cell size, varying between 32.1% and 66.1%.

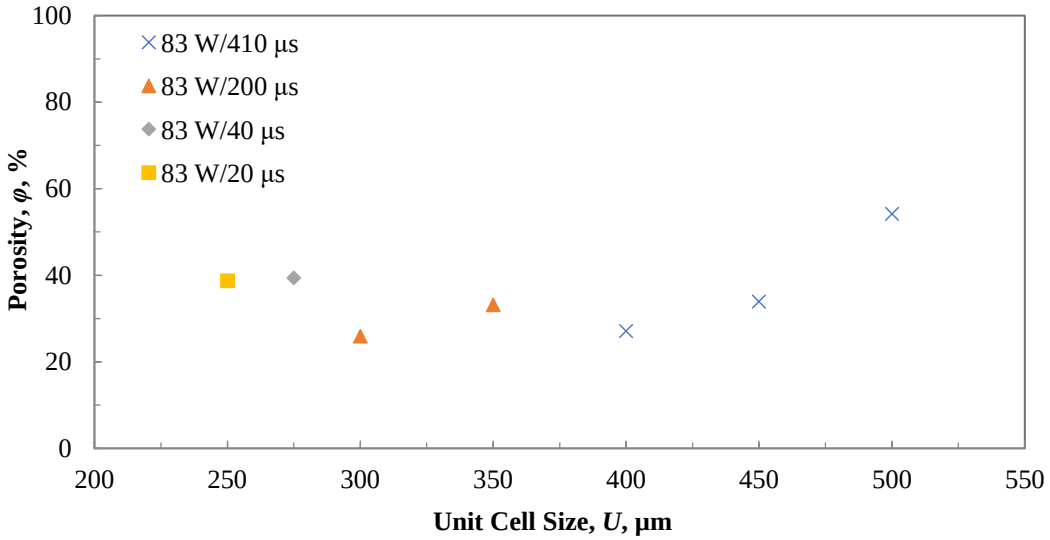

Figure 4- 6 Variations of porosity with unit cell size for single exposure samples with a laser power of 83 W and different exposure times

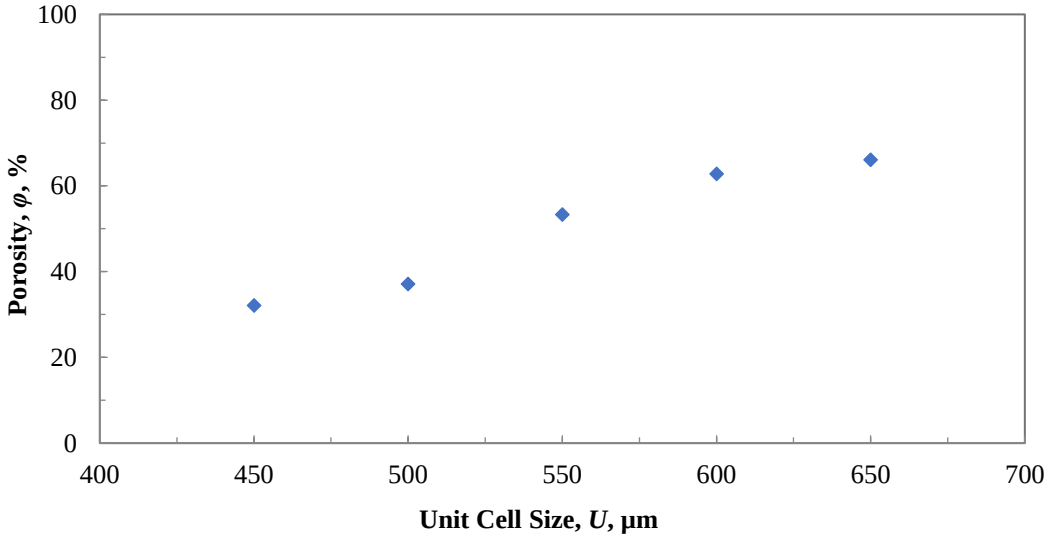

Figure 4- 7 Variations of porosity with unit cell size for double exposure samples with a laser power of 83 W and exposure time of 410 µs

A comparison between the structures with the same unit cell sizes, manufactured with

single and double exposure scanning strategies is made in Figure 4-8. The porosity of the single exposure samples is always higher than that of the double exposure samples, and the difference becomes larger with increasing unit cell size.

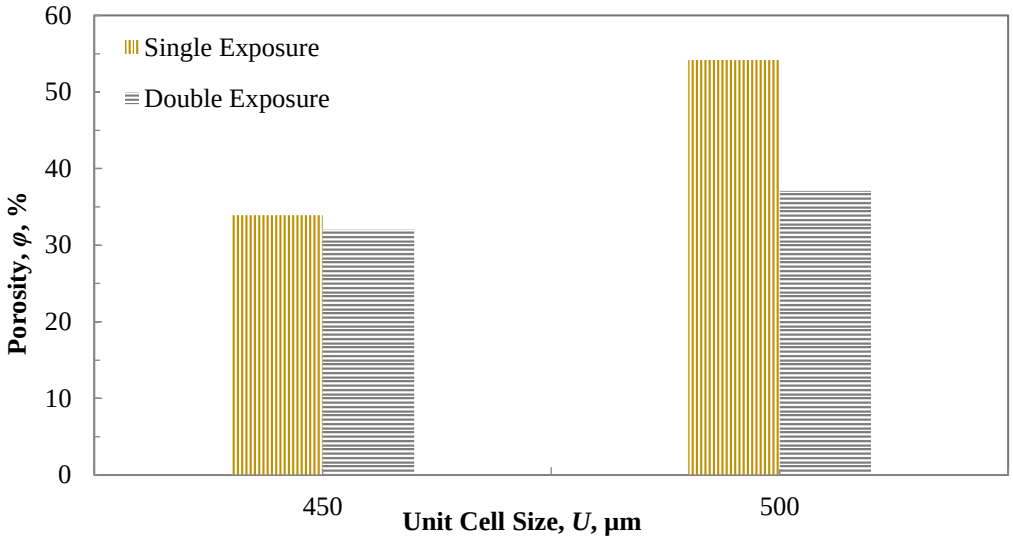

Figure 4- 8 Comparison of porosity between the same unit cell size structures with different laser scanning strategies

4.2 Manufacture of Unit Cell Structures in Ti-6AL-4V

Ti-6Al-4V was used as an alternative material to manufacture porous structures because its products manufactured by AM have been widely used in orthopaedic applications due to its biocompatibility and excellent corrosion resistance. In addition, Ti-6Al-4V has good compatibility with all the working fluid candidates in this project. However, the optimum pore size for orthopaedic applications is in the range of 200-800 µm, which is too large for heat pipe applications. The predicted average pore size should be less than 260 µm to meet the requirement of lift height when working against gravity. Different laser powers and laser exposure times have been used for various unit cell sizes to find out the optimum porous structures with small pore sizes. The aim is to achieve porous structures with a pore size less than 200 µm and find out the optimum laser parameters. The effects of laser power and laser exposure time were

investigated. Four small unit cell sizes were selected to compare the porosity and pore size. The processing conditions are shown in Table 4-3.

Table 4- 3 Laser processing conditions used for the optimisation of Ti-6Al-V4 porous structures

Unit Cell Size, *U*, µm	**Laser Power, *P*, W**	**Laser Exposure, *t*, µs**
300	60-180 (interval of 20)	40-200 (interval of 40)
350		
400		
450		40-120 (interval of 40)

4.2.1 Porosity and Pore Size

The SEM images of the 400 µm unit cell samples with six combinations of laser power and laser exposure time are shown in Figure 4-9. The measured values of the strut diameter are between 130 and 235 µm.

Figure 4-10 shows that the pore size of the samples with various unit cells changes with laser power and laser exposure time. All pore sizes are smaller than 100 µm and are in the range of 30 and 95 µm. The pore size has the same trend as porosity, decreasing with increasing laser power, increasing exposure time or increasing unit cell size. All the porous structures have severe powder adhesion defects and some have slags inside. For porous structures with tiny pores, some of the pores are blocked by the sintered attachments.

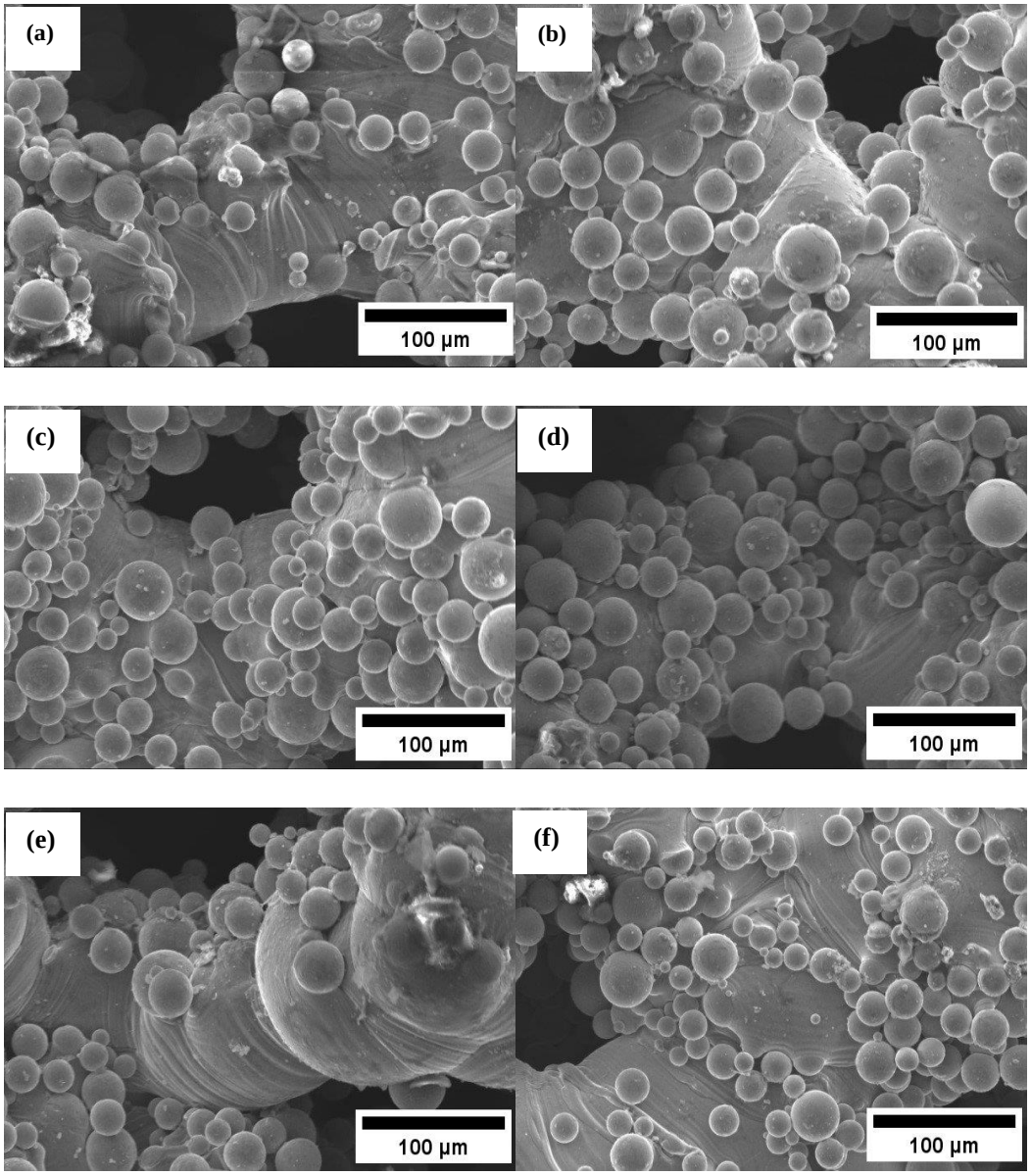

Figure 4- 9 SEM images of Ti64 400 µm unit cell porous structures manufactured with different combinations of laser power and exposure time: (a) power 100 W, exposure time 40 µs; (b) power 120 W, exposure time 60 µs; (c) power 80 W, exposure time 80 µs; (d) power 100 W, exposure time µs; (e) power 60 W, 120 µs; (f) power 160 W, exposure time 80 µs

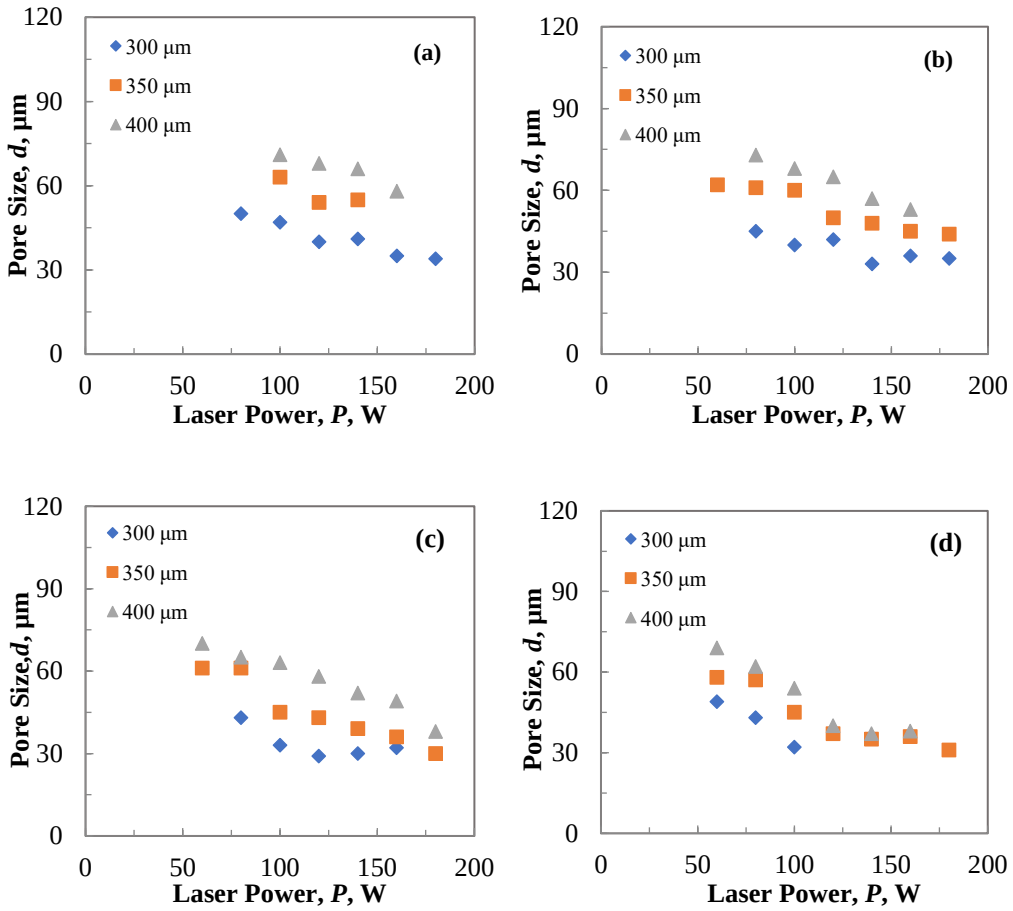

Figure 4- 2 Changes of pore size with laser power for samples with different unit cell sizes and different exposure times: (a) 40 µs; (b) 80 µs; (c) 120 µs; (d) 160 µs

Laser energy density can be introduced to express the influence of both laser power and laser exposure time on the characteristics of porous structures. It can be expressed as follows:

$$E_\rho = \frac{Pt}{\pi r^2} \qquad \text{(Equation 4-1)}$$

where P is the laser power, t is the laser exposure time, and r is the radius of the applied laser beam. The nominal beam diameter used here is a constant with a value of 50 µm. According to Nemec (2017), there is an optimal porosity of sintered wick between 30% and 75%. Figure 4-11 shows that the porosity of the parts is less than 30% when the laser energy density is more than 5 J/mm^2 for 300 µm and 350 µm unit cells. It was

reported that varying the combination of the power, exposure time and beam diameter can have a significant effect on the structure and the properties of the manufactured component even if the beam energy remains constant (Lü et al., 2013). Figure 4-12 shows that, with the same laser energy density, the porosity of the same unit cell size samples can be different.

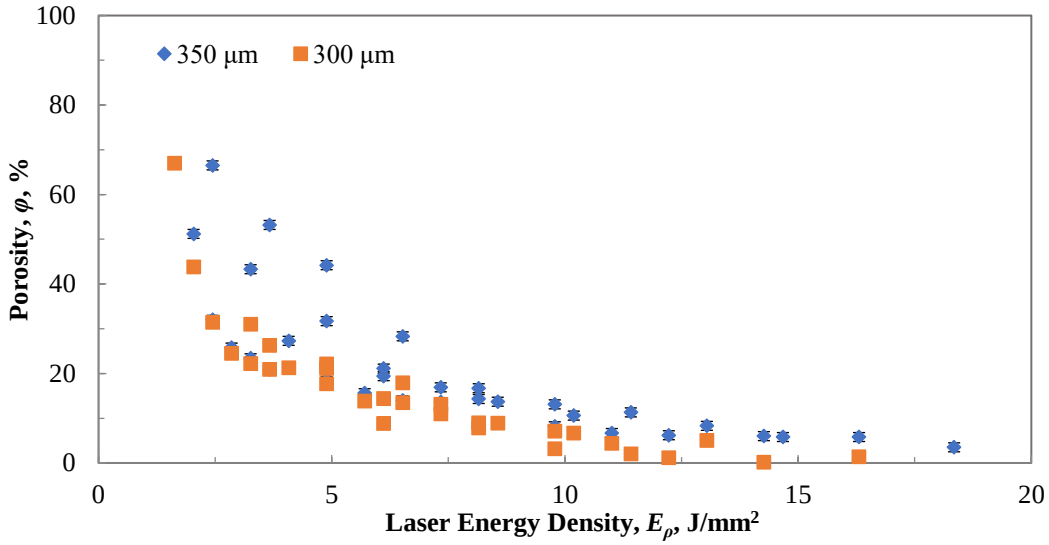

Figure 4- 11 Changes of porosity with laser energy density for 300 µm and 350 µm unit cell size samples

4.3 Discussion

As shown in Figure 4-1, when a short laser exposure time was used, some defects exist in the porous structure because the laser energy used was insufficient to fully melt the metal powder, hindering liquid phase interaction with un-melted powder. Besides, the laser beam could not penetrate the previously solidified layer for the new layer to attach. When the laser exposure time was too long, however, the width of the melt pool increased, and overlap between the melt pools (especially for small unit cell size samples) occurred, resulting in the densification of the porous structure.

The strand diameter was increased for the double exposure samples compared with the single exposure samples manufactured with the same unit cell size and laser

parameters. The experimental strut diameters for the 300 and 350 μm unit cell structures are the same. They are also similar for the 400, 450 and, 500 μm unit cell structures. The average strut diameters for all double exposure samples are similar. It is shown that the strand diameter only depends on the laser parameters used, i.e., laser power (see Figure 4-12) and laser exposure time, and the unit cell size has little effect on it. The strut diameter is only affected by the unit cell size when the unit cell size is smaller than 300 μm. It is because the adjacent exposures are too close to each other so that the neighbouring melt pools are merged to form a thicker strut diameter.

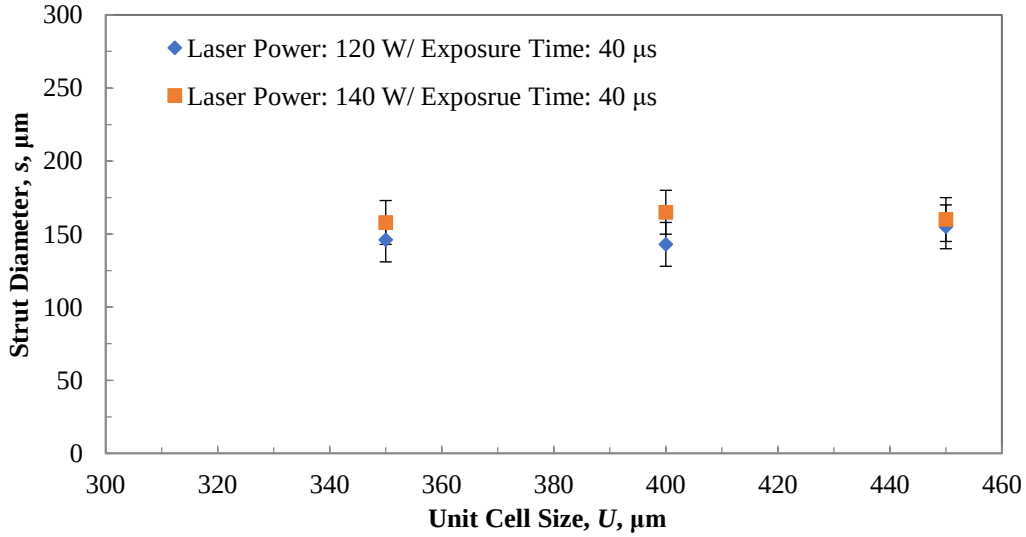

Figure 4- 12 Changes of strut diameter with unit cell size for samples built with the same laser parameters in Ti64

The porosity and pore size of the porous structures are highly dependent on the unit cell size and laser parameters. The laser energy density used in the SLM process should be high enough to melt the metal powder; otherwise, the balling phenomenon occurs. When the laser energy density is small (low laser power and short laser exposure time), the balling effect arises because the powder cannot be melted and fused properly. When the powder is heated and becomes molten, the intermolecular forces of the metal when in a liquid state attract in all directions (Louvis, 2012). These

forces cause the surface tension of the metal and at high values, cause the metal to ball up into a sphere, which has the lowest surface to volume ratio. Balling also occurs when high laser powers are used with short exposure time, as this produces an unstable cylindrical molten track, which results in liquid droplet splash from the track surface (Gu et al., 2008). The experimental results also show that the porosity and pore size of the porous structures decrease with double exposure scanning for the same unit cell size and laser energy density, and the difference becomes more significant with a large unit cell size, because an increasing strut diameter forms from the enlargement of the melt pool. For small unit cell sizes such as 250 and 275 μm, the pores can be blocked if the large laser energy density is used because the melt pools created by adjacent points can overlap with each other, causing solid part or closed pores. The porosity is mainly contributed by the space between unmelted powder particles and the space between the powder particles and the struts. The porosity and pore size can be different, even the same unit cell size and the same laser energy density are used. The strut diameter for the sample manufactured with a laser power of 60 W and a laser exposure time of 120 μs is 105 μm, while in the samples manufactured with a laser power of 180 W and a laser exposure time of 40 μs, the pores are hardly observed in the SEM images.

In this work, by comparing the porosity values of the samples manufactured with the same laser energy density but different laser powers and laser exposure times, as shown in Table 4-4, it was observed that the porosity was affected by laser power more than laser exposure time. For the 300 μm unit cell porous structure, the porosity increased from 17.7 to 22.1% with laser power decreasing from 120 to 60 W, even the exposure time was doubled from 80 to 160 μs. For the 400 μm unit cell porous structure, porosity increased from 24.9% to 65.9%. This trend applies to all the

samples in this study. It can be concluded that laser power is the dominating factor compared with laser exposure time in affecting the porosity of the sample, because the exposure time used in this study is very short and the formation of the melt pool is affected directly by the power delivered by the laser beam.

Table 4- 4 Porosity values of samples produced with the same laser energy density

Laser Parameters	**300 µm**	**350 µm**	**400 µm**
180 W/40 µs	20.9%	20.9%	26.6%
60 W/120 µs	26.3%	53.2%	65.9%
120 W/80 µs	17.7%	20.3%	24.9%
80 W/120 µs	21.1%	31.7%	47.5%
60 W/160 µs	22.1%	44.2%	65.9%
160 W/80 µs	13.5%	14.0%	20.4%
80 W/160 µs	17.9%	28.3%	41.6%
100 W/120 µs	14.4%	21.1%	28.0%
60 W/200 µs	8.8%	19.4%	53.9%
180 W/80 µs	11.0%	13.6%	10.9%
120 W/120 µs	13.1%	16.9%	19.9%

Powder particles visibly adhered to the surface of the melted strands, increasing the mean strand diameter. The sample consisted of properly melted central core and a low-sintered zone (Tolochko et al. 2003). The main core was formed during the laser melting stage, becoming the fully dense core of the wireframe strands. In the low-sintered zone, only the skins of the particles were melted, and the necks were formed between the particles and the strands. More powders are prone to attach on the surface of strut with larger diameter because the perimeter of melt pool increases which means there are more space for loose powder attachments. In the double exposure samples, re-melting increased the width of the central core and the low-sintered zone

simultaneously. The powder adhesion issue can lead to low accuracy of the pores. It becomes worse when an overhanging structure is fabricated, because low heat conduction in the powder supported zone than the solid-supported zone can lead to a bigger melt pool, which can sink into the powder as the result of gravity and capillary force (Wang et al., 2013). It has widely been reported that strut orientation has a strong effect on the final diameter of the lattice strut and greater deviations can happen in a horizontal strut due to overmelting (Arabnejad et al., 2013, Cuadrado et al., 2017, Echeta et al., 2020). The strut diameter also increases around the nodes. This can explain the pore distribution in Figure 4-3 and the difference between the theoretical and experimental pore sizes, because, although all the pores are designed to be the same, the pore size is affected by the number and size of the attached unmelted powder particles. For heat pipe applications, the sintered attachments to the surface of the strut or the wall can serve as secondary capillary structures allowing for decreased start-up power and probably increased lift height of working fluid. The existence of sintered attachments also means less space between the struts. The decreasing 'pore size' can benefit the capillary lift height according to Equation 2.11.

Several studies have used re-melting strategies to improve the density of the solid parts manufactured by SLM (Demir and Previtali, 2017, Yasa and Kruth, 2011, Yasa et al., 2011). It was found that re-melting can significantly reduce the surface roughness of the solid parts because the residual particles are melted in the second scanning routine and the oxidation film formed and floated on the surface of the melting pool in the first scanning can be broken by the second scanning (Yu et al., 2019). However, re-melting has the opposite effect to the side surface. Figure 4-2 shows that more partially melted particles tend to adhere to the side surfaces of the strut because more particles are exposed to the melting pool due to the second laser scanning and the partially fused

powder in the first scanning tends to expand because of heat absorption (Calignano, 2018).

Theoretically, the target of a lift height of 200 mm can be achieved by decreasing the pore size to under 60 μm, which can be achieved by decreasing the laser energy density and the unit cell size for both CpTi and Ti64. However, as discussed above, structures made with low energy density can contain many defects. Therefore, low laser energy density should be avoided even though a small pore size may be generated, and a high lift height may be obtained. Moreover, large unit cells are preferable for the ease of production of the porous structure. The modelling and experimental results showed that 300 and 350 μm unit cells are suitable for this project.

Chapter 5

Permeability, Capillary Force and Heat Transfer Coefficient of Porous Structures

The previous chapter has described the process of optimising laser parameters for the production of porous structures in Cp-Ti and Ti6Al4V. In order to understand the fluid and thermal performance of the porous structures, the permeability, capillary force and heat transfer coefficient have been measured using the methods detailed in Chapter 3. Highly porous, open-celled geometries are usually preferred for use in heat transfer devices as they improve the heat transfer performance by enhancing thermal convection between the solid wall and the fluid. In heat pipe applications, the working fluid is contained in the wall and the phase change of the working fluid between gas state and liquid state can make the devices handle heat fluxes over 1 kW/cm^2. The pore size plays an essential role in the capillary action, which is very important for heat pipes required to work against gravity. The vertical lift height of working fluid increases with decreasing pore sizes.

One of the significant advantages associated with the use of the unit cell approach for the manufacture of wick structures in heat pipe applications is that the structures can be designed and modified to possess the exact properties for the use in any operating situation. The octahedral porous structure can be manufactured with fully interconnected pores which have a significant effect on the flow properties.

5.1 Permeability

The permeability of all samples was measured using the methods detailed in Chapter 3. The flow rate used was between 0.1 L/min to 2.0 L/min, and Forchheimer's law was used to calculate the permeability. The standard deviation of the measured permeability is less than 3.5%. For a heat pipe application, the requirement of the permeability of the wick structure is in the range of 10^{-12} to 10^{-10} m^2.

5.1.1 Permeability of Samples in CpTi

The permeability results of all samples are listed in Table 5-1. Each sample was characterised by its unit cell size, porosity and pore size. The permeability is in the range of 0.2 to 36.6 10^{-10} m^2.

It can be found that the permeability increases with increasing porosity and pore size. For single exposure samples, the highest permeability with a value of 2.9 x 10^{-10} m^2 is obtained in the sample with a porosity of 54.2% and a pore size of 170 μm, while the lowest permeability with a value of 0.2 x 10^{-10} m^2 comes from the sample with a porosity of 25.9% and a pore size of 30 μm.

The permeability of the porous structures manufactured with double exposure scanning shows the same trend as samples made with single exposure scanning. The highest permeability with the value of 36.6 x 10^{-10} m^2 is obtained from the sample with a porosity of 66.1% and a pore size of 166 μm, and the lowest permeability with the value of 0.5 x 10^{-10} m^2 is from the sample with a porosity of 37.1% and a pore size of 78 μm.

Table 5- 1 Permeability of porous structures in CpTi with different pore sizes and porosities, single exposure scanning

Unit Cell Size, *U*, µm	**Laser Strategy**	**Porosity *φ*, %**	**Pore Size *d*, µm**	**Permeability *K*, 10^{-10} m^2**
650	Single Laser	-	-	-
	Double Exposure	66.1	166	36.6
600	Single Laser	-	-	-
	Double Exposure	62.8	137	7.7
550	Single Laser	-	-	-
	Double Exposure	53.3	110	1.7
500	Single Laser	54.2	171	2.9
	Double Exposure	37.1	78	0.5
450	Single Laser	33.9	114	0.4
	Double Exposure	-	-	-
400	Single Laser	27.1	95	0.2
	Double Exposure	-	-	-
350	Single Laser	33.2	77	0.3
	Double Exposure	-	-	-
300	Single Laser	25.9	62	0.2
	Double Exposure	-	-	-
275	Single Laser	39.4	32	0.2
	Double Exposure	-	-	-
250	Single Laser	38.7	30	0.2
	Double Exposure	-	-	-

The variations of pressure drop with outlet water velocity for selected specimens with different unit cell sizes with single exposure and double exposure are shown in Figures 5-1 and 5-2.

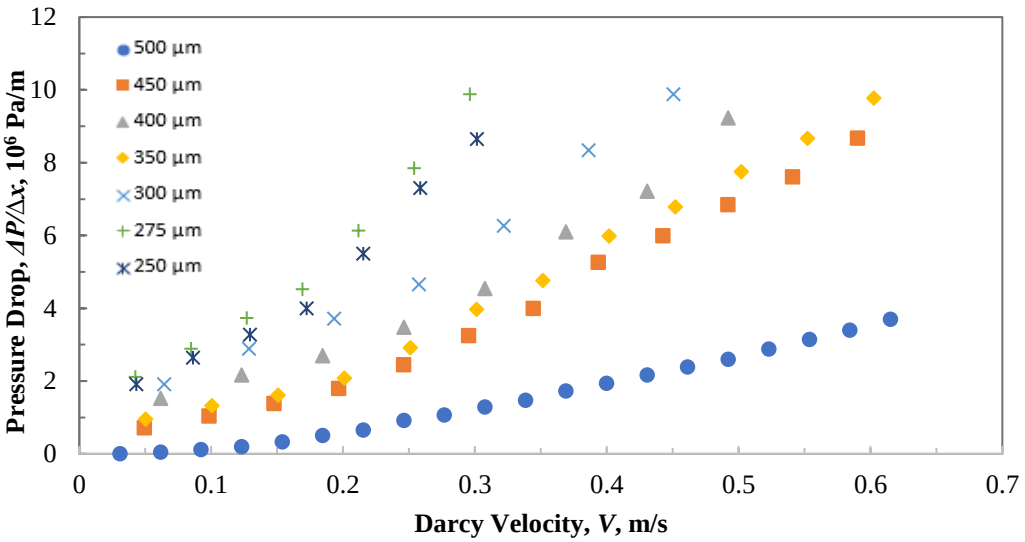

Figure 5- 1 Variations of pressure drop with outlet velocity for specimens manufactured with single exposures

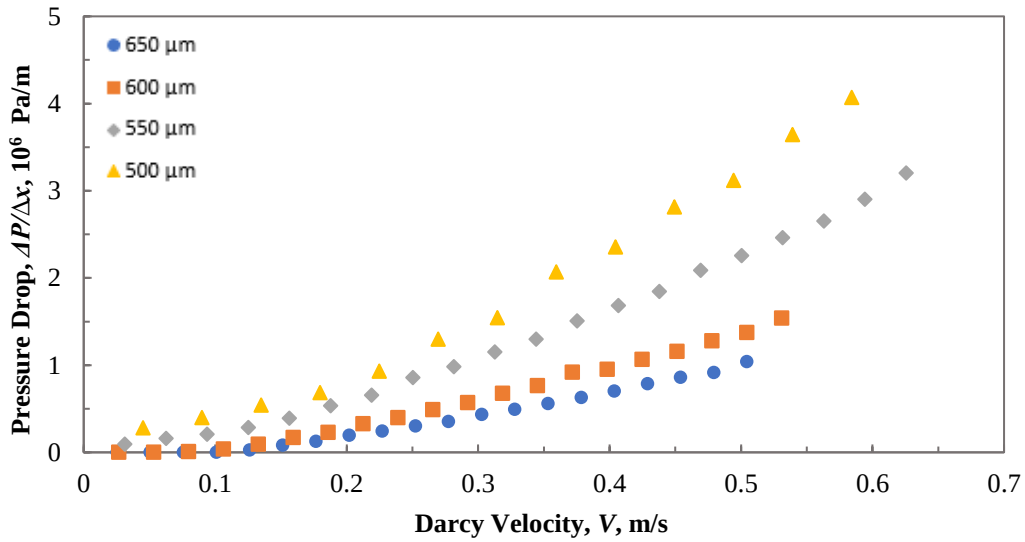

Figure 5- 2 Variations of pressure drop with outlet velocity for specimens manufactured with double exposures

It can be found that pore size and porosity play essential roles in the permeability and pressure drop. Samples with similar porosity and pore size have a similar permeability. For example, the 250 µm and 275 µm unit cell samples, having similar porosities of 39.4% and 38.7% and pore sizes of 32 µm and 30 µm, respectively, have a similar permeability value of 0.2 x 10^{-10} m^2. The 650 µm unit cell samples show the lowest

pressure drops at any given flow rate and the highest pressure drops come from the 275 and 250 μm unit cell size samples that possess the lowest porosity and smallest pore size. The pressure drop decreases with unit cell size.

As the porous structures are intended for use in space applications, the pressure drop per unit mass has been considered. The pressure drop per unit mass results for the samples with single exposure and double exposure are shown in Figures 5-3 and 5-4, respectively. They show the same trend as in Figures 5-1 and 5-2. The highest value still comes from the sample with the largest unit cell, which possesses the highest porosity and largest pore size. For double exposure samples, the difference of pressure drop between varying unit cell sizes becomes smaller when mass is taken into consideration.

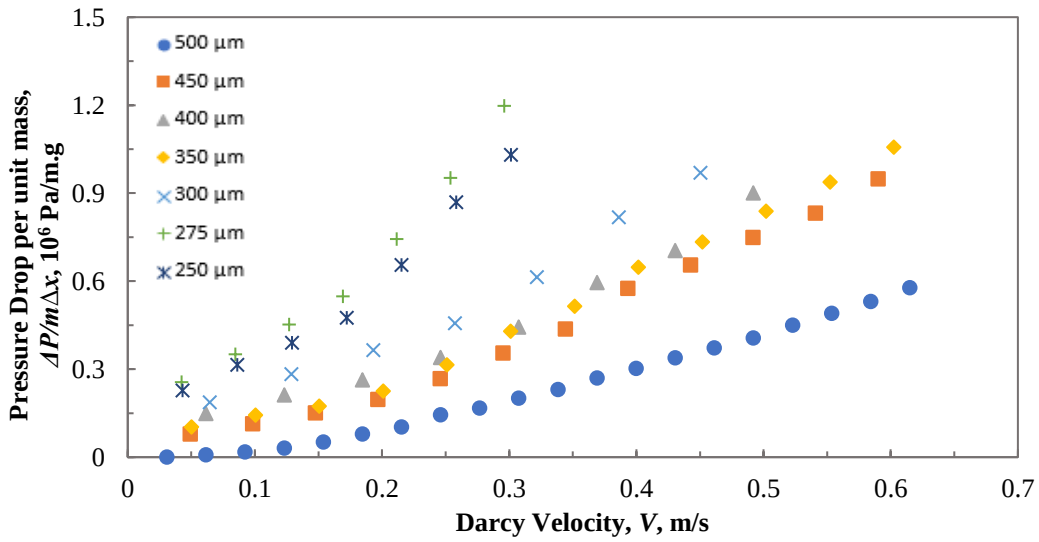

Figure 5-3 Variations of pressure drop per unit mass with outlet velocity for specimens manufactured with single exposures

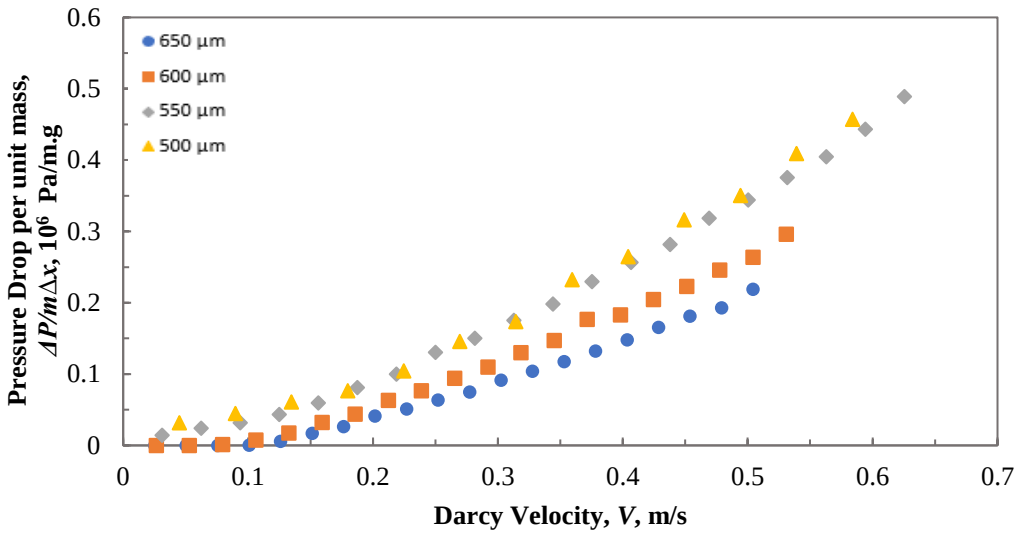

Figure 5-4 Variations of pressure drop per unit mass with outlet velocity for specimens manufactured with double exposures

A modification was made to Equation 3-4 by dividing both sides by the Darcy velocity, and a new relationship between reduced pressure drop and Darcy velocity is obtained:

$$\frac{\Delta P}{LV} = \rho C V + \frac{\mu}{K} \qquad \text{(Equation 5-1)}$$

The relationship between the reduced pressure drop and Darcy velocity for a 550 µm unit cell sample is shown in Figure 5-5, as an example. There are three regimes for the flow rate in the range of 0.1 L/min to 2 L/min. When the Darcy velocity is less than 0.05 m/s, the reduced pressure drop tends to be a constant, which means the flow is laminar in this regime, and Darcy's law should be applied:

$$\frac{\Delta P}{L} = \frac{\mu}{K} V \qquad \text{(Equation 5-2)}$$

For the other two regimes, there is a linear relationship between the reduced pressure drop and Darcy velocity, so Forchheimer's law, as shown in Equation 3-4, should be applied.

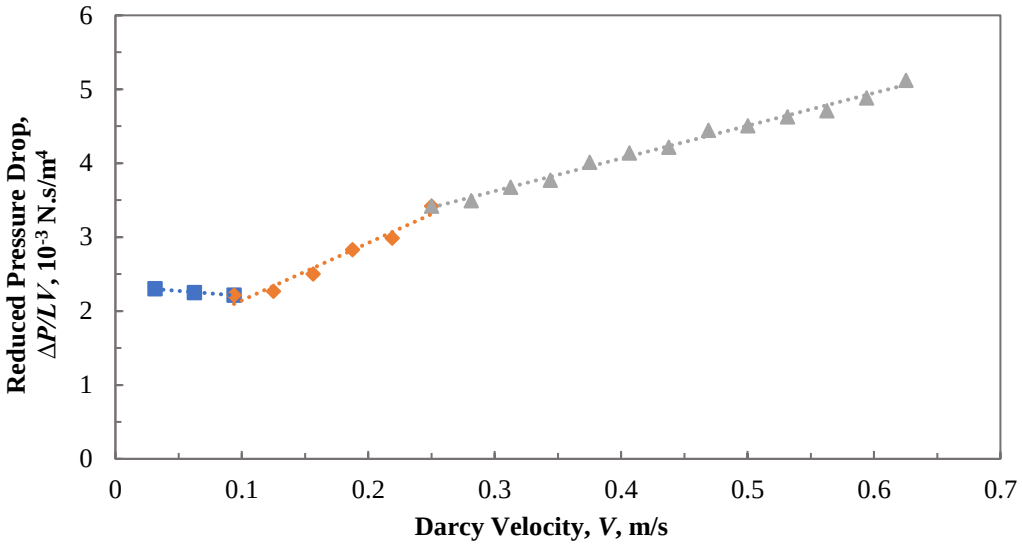

Figure 5- 5 Change of reduced pressure drop with Darcy velocity for 550 μm unit cell sample

Reynolds number is introduced to define the different regimes of the flow, and it can be calculated as follows (Zeng and Grigg, 2006):

$$Re = \frac{DV\rho}{\mu\varphi} \qquad \text{(Equation 5-3)}$$

where Re is the Reynolds number, D is the diameter of the pores, V is the Darcy velocity, ρ is the density of the fluid, μ is the viscosity of the fluid and φ is the porosity of the sample. In Figure 5-5, the first transition point is at a Reynolds number of 10.8, below which the fluid flow is laminar. The second transition point is at a Reynold number of 29.3, above which the fluid flow has become turbulent.

The critical Reynolds numbers were calculated for all the samples and are displayed in Table 5-2. The permeability for the first regime was calculated using the Darcy equation and the permeabilities for the second and third regimes were calculated using the Forchheimer equation. However, the pressure drop measurement accuracy in Darcy's flow was limited by the rig used, leading to significant errors in the results. Therefore, only the permeabilities for the second and third regimes were calculated

and are listed in Table 5-3. It is shown that the second permeability of each sample is always higher than the third permeability. The permeability tends to decrease with the increase of flow rate.

Table 5- 2 Critical Reynolds numbers of transitions for varying unit cells in CpTi

Unit Cell Size *U*, μm	**Laser Strategy**	**Reynolds Number for First Transition**	**Reynolds Number for Second Transition**
650	Single Laser	-	-
	Double Exposure	16.9	33.9
600	Single Laser	-	-
	Double Exposure	10.8	29.3
550	Single Laser	-	-
	Double Exposure	10.4	27.8
500	Single Laser	10.6	42.5
	Double Exposure	14.2	28.3
450	Single Laser	22.7	45.3
	Double Exposure	-	-
400	Single Laser	23.6	-
	Double Exposure	-	-
350	Single Laser	23.6	47.3
	Double Exposure	-	-
300	Single Laser	16.1	-
	Double Exposure	-	-
275	Single Laser	5.5	-
	Double Exposure	-	-
250	Single Laser	5.2	-
	Double Exposure	-	-

Table 5- 3 Permeabilities of CpTi samples with different unit cell sizes

Unit Cell Size *U* μm	Laser Strategy	Second Permeability *K*, 10^{-10} m^2	Third Permeability *K*, 10^{-10} m^2
650	Single Exposure	-	-
	Double Exposure	48.2	24.8
600	Single Exposure	-	-
	Double Exposure	7.5	4.8
550	Single Exposure	-	-
	Double Exposure	2.5	1.4
500	Single Exposure	4.6	2.1
	Double Exposure	0.8	0.3
450	Single Exposure	0.6	0.3
	Double Exposure	-	-
400	Single Exposure	0.5	-
	Double Exposure	-	-
350	Single Exposure	0.6	0.2
	Double Exposure	-	-
300	Single Exposure	0.4	-
	Double Exposure	-	-
275	Single Exposure	0.4	-
	Double Exposure	-	-
250	Single Exposure	0.4	-
	Double Exposure	-	-

5.1.2 Permeability of Samples in Ti-6Al-4V

The relationship between reduced pressure drop and Darcy velocity for the Ti64 samples was analysed. It is the same as for CpTi, and there are three regimes for the flow rate in the range of 0.1 L/min to 2.0 L/min. The Reynolds numbers of the two transitions and the corresponding permeabilities for the 300, 450, 350 and 400 μm unit cell samples were calculated, and the results are displayed in the Appendix. The Reynold numbers for the first transition for all samples are between 7 and 20, while the Reynold numbers for the second transition for all samples are between 20 and 65.

Figures 5-6 and 5-7 show the first and second transition Reynold numbers for samples manufactured with an exposure time of 80 μs.

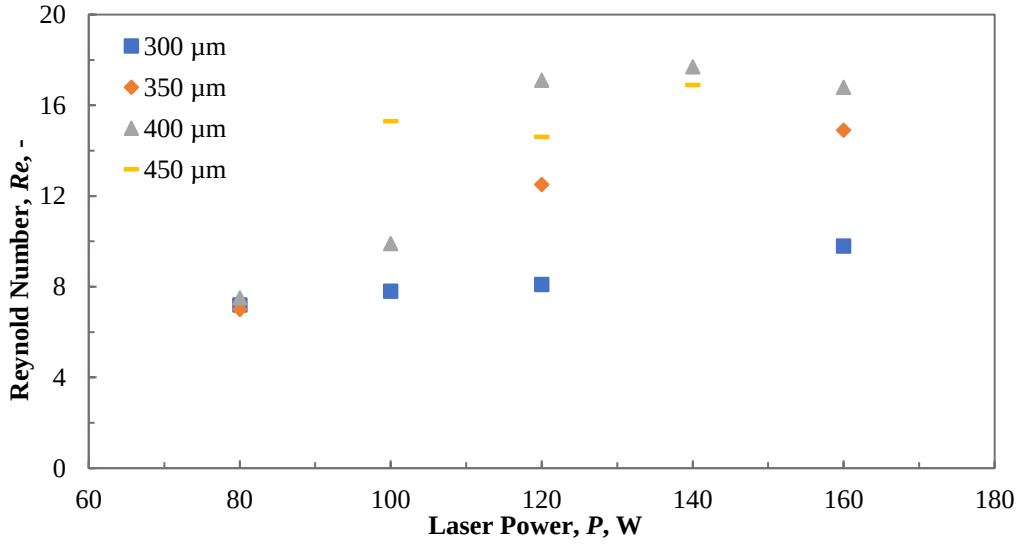

Figure 5-6 Variations of first transition Reynolds number with laser power for various unit cell size samples

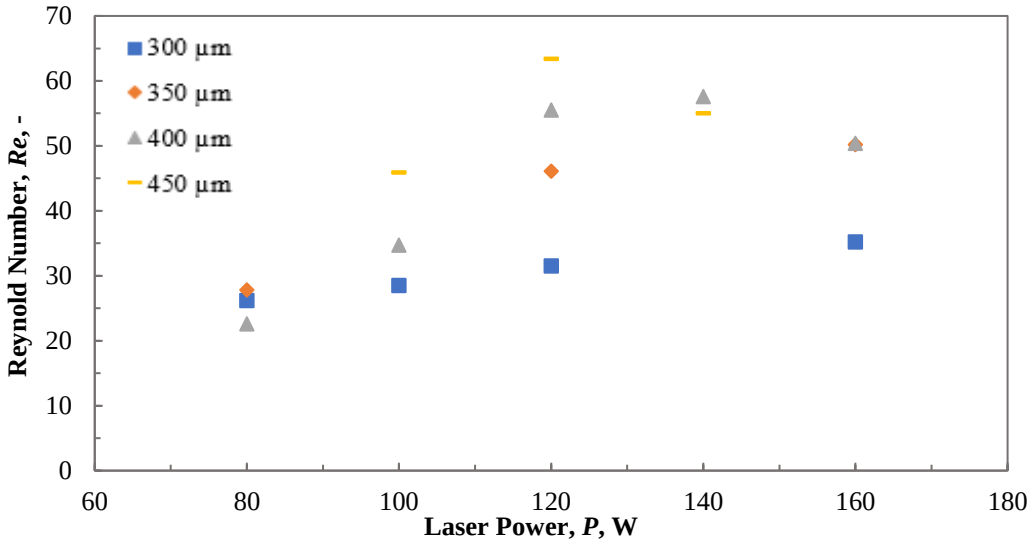

Figure 5-7 Variations of second transition Reynolds number with laser power for various unit cell size samples

It is shown that the transition Reynolds numbers change with laser power and unit cell size, because the as-manufactured porous structures have varying porosity and pore size. In samples with high porosities and large pore sizes, with the same flow rate, the

passing fluid tends to be laminar due to larger space or less flow resistance. Figure 5-8 shows that the overall permeability increases with increasing porosity and pore size manufactured with larger unit cell size, lower laser energy. All the permeability results are in the range of 10^{-11} to 10^{-10} m^2.

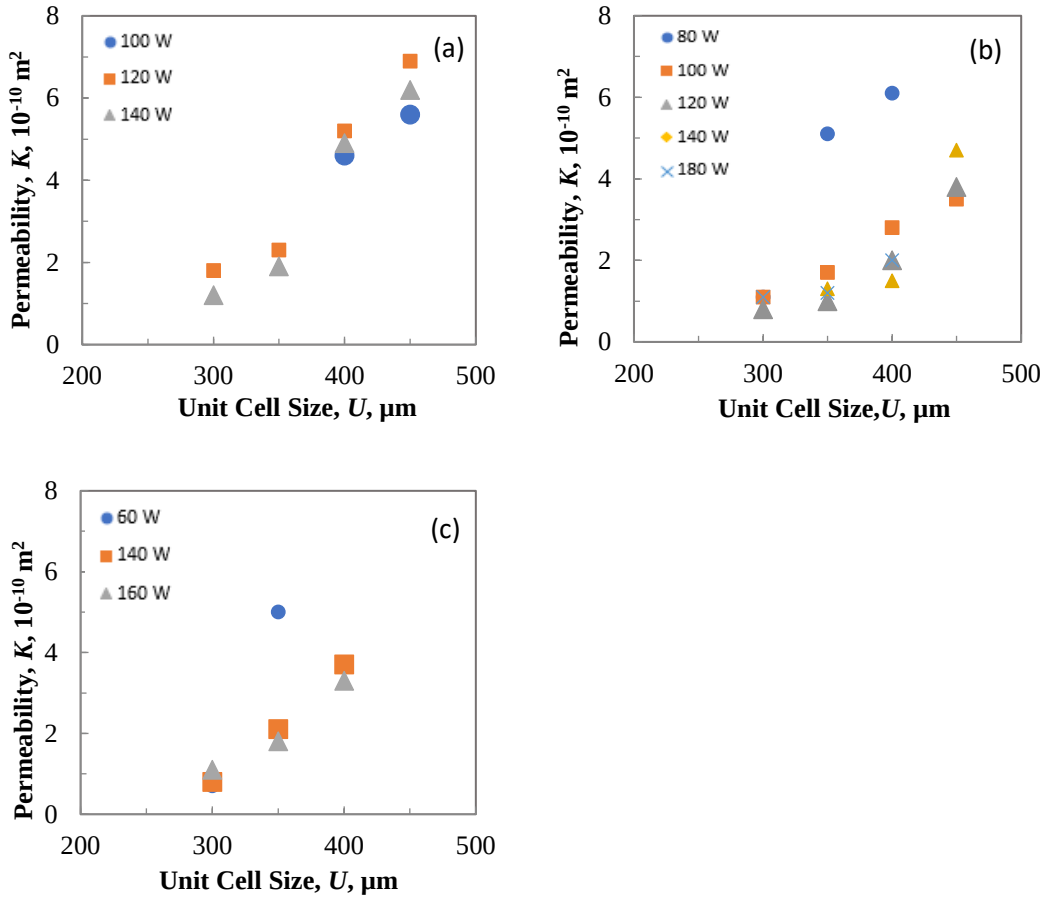

Figure 5- 8 Permeabilities of porous structures in Ti64 with different laser powers and exposure times of: (a) 40 µs; (b) 120 µs; (c) 200 µs

5.1.3 Discussion

The experimental results of pressure drop show that lower pressure drops are generated for the samples with higher porosities and pore sizes. The pores within the porous structures manufactured by SLM are designed to be totally interconnected. An increase in porosity means a smaller solid fraction within the structure and more channels for the fluid to flow through, which can significantly reduce the flow

resistance of the fluid. Similarly, for samples with any specific unit cell, larger pores mean decreasing strut size and decreasing solid volume in the structure, which give rise to lower flow resistance and thus a lower pressure drop at any given flow rate. Samples with high porosities and pore sizes always have the lowest pressure drops per unit mass. They have higher permeabilities with less weight and can significantly reduce the cost for space applications.

Many studies determined the permeability of porous structures using the Darcy equation. This equation is only valid when the flow is considered laminar, and this is usually accepted when the Reynolds number is less than 10. Davis et al. (1992) showed that the experimental results published by Darcy fit the quadratic relationship better than the linear one when the velocity is more than 4×10^{-3} m/s. Khayargoli et al. (2004) used flow velocities in the range of 0-15 m/s and found that the pressure drop across the metal foam is a quadratic function of the flow velocity. When velocity increases, the inertia effect becomes more significant, the flow tends to be turbulent, and the pressure drop in the structure displays a quadratic trend. The quadratic term in the Forchheimer equation represents the influence of inertia, and the value of C is influenced by many factors of the structure such as porosity, pore size and surface roughness.

In this study, the permeability was calculated using the Forchheimer equation for flow rates in the range of 0.1 L/min to 2.0 L/min. For both CpTi and Ti64 structures, when the same laser power and laser exposure time were used (which means the manufactured strut diameters are similar), the permeability increases with the unit cell size. This is because a higher porosity and larger pore size are resulted with a larger unit cell size, which means less strut or smaller solid fraction exists in the structure, so the resistance to the fluid flow in the structure decreases.

The relationship between reduced pressure drop and flow velocity is shown in Figure 5-3. There are three flow regimes in the flow rate range studied. When the flow rate is low, less than 0.05 m/s, the reduced pressure drop remains a constant, which means the pressure drop has a linear correlation with the flow velocity. Darcy equation is applicable in this region, and the inertia force is negligible. It means that the flow in this range is laminar. With the velocity increases, the flow in the structure begins to deviate from laminar, and there is a linear relationship between reduced pressure drop and velocity. It means that the inertia force begins to replace the viscous force as the dominant force in the flow. This region can be considered as a transition regime from laminar to turbulent. The Forchheimer equation should be applied to determine the permeability. The slope of the curve changes when the velocity increases further, and the flow becomes fully turbulent. It was found that the Reynold number for each transition point varies with the structure. The permeability in the transitional flow is always larger than that in the turbulent flow. Lu et al. (2018) studied the permeability of a porous glass structure in different flow regimes. Their results showed that the permeability in Darcy flow is always the largest, and the permeability decreases when the velocity increases and the flow becomes turbulent. It is because the interaction between the fluid and the solid structure in the Darcy regime is weak, causing less energy dissipation. When the velocity increases, the flow changes to turbulent, which means the flow undergoes irregular fluctuations instead of moving in smooth paths or layers, causing a decrease in mass transfer efficiency.

5.2 Lift Height

5.2.1 Lift Height of Samples in CpTi

Only samples with single exposure were used for the capillary action tests, because double exposure can worsen the strut surface roughness and similar porosity and pore

size can be achieved by changing the unit cell size using single exposure.

Figure 5-9 shows the IR images of the meniscus rising process in a typical porous structure. It shows that the sample was wetted by the working fluid, in this case, water, with time. A meniscus was formed, which is dark due to the different infrared emissivity of dry Ti and wet Ti. The images from the IR camera were analysed using ImageJ. The height of the peak of the meniscus was considered to be the lift height. All the lift height results are listed in Table 5-9.

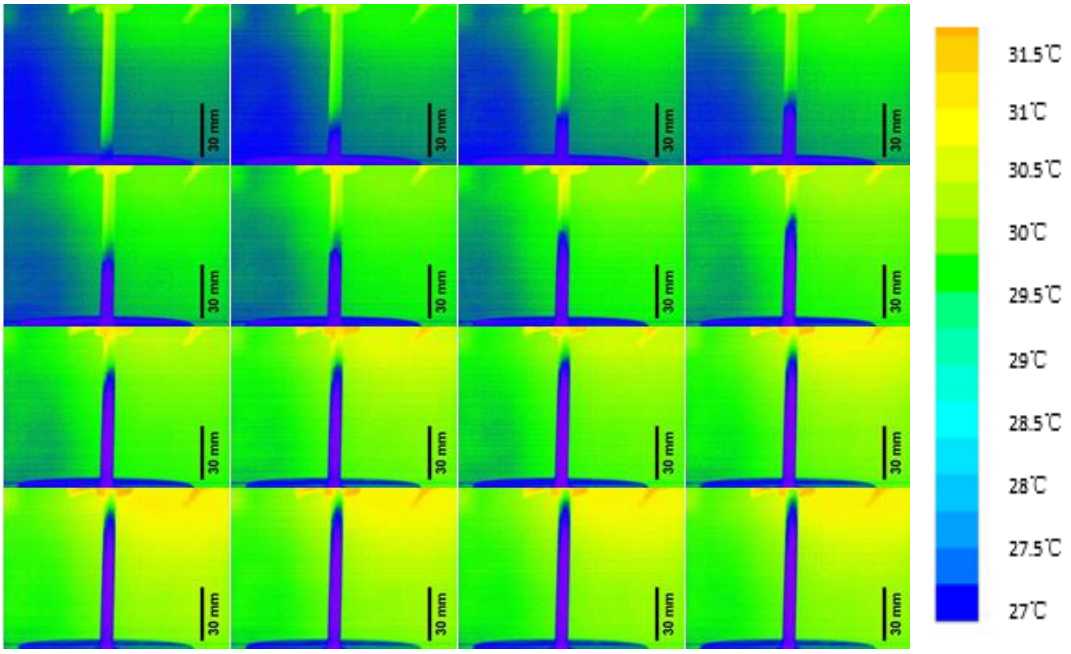

Figure 5- 9 IR images of meniscus rising process of SLM porous structure, 400 μm unit cell size, in 10 minutes (Interval of 40s)

Table 5- 4 Lift height results from IR images for CpTi samples

Unit Cell Size *U*, μm	250	275	300	350	400	450	500
Lift Height *h*, mm	33.6	20.2	194	200	94.4	95.2	97.6

The weight changes of the water absorbed in 1 hour for the CpTi structures, recorded by the analytical balance with an interval of 5 seconds, are shown in Figure 5-10. The

absorption rate is very high in the first 10 minutes for all samples, and then it becomes stable after about 1 hour. The 450 µm unit cell sample shows the highest absorption among all the samples; the 275 µm and 250 µm unit cell samples show the steepest weight changes in the first 10 minutes.

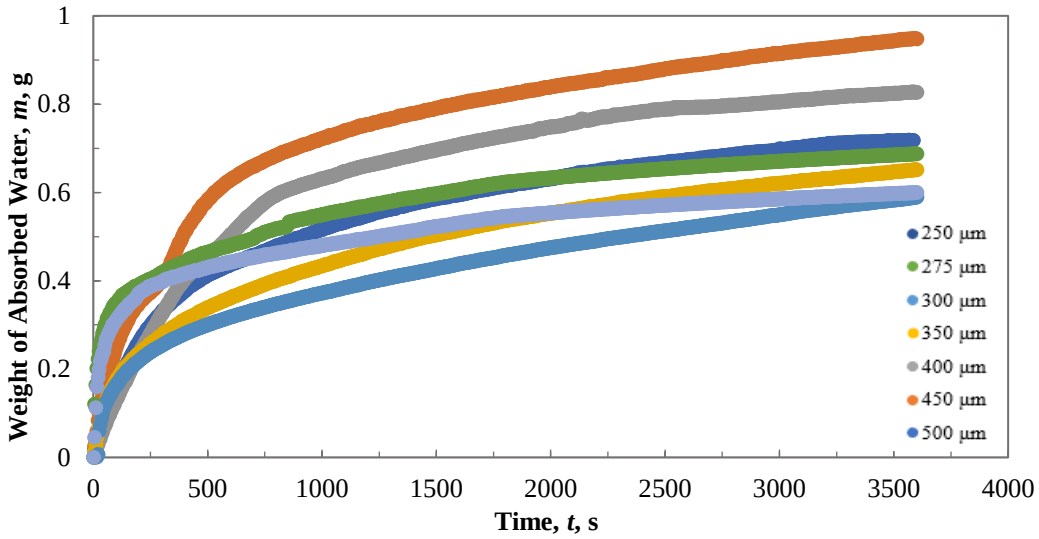

Figure 5- 10 Change of weight of absorbed water with time for CpTi samples with different unit cell sizes

A comparison between the lift height results obtained from the IR images and the weight changes for the CpTi samples is shown in Figure 5-11. Equation 3-5 was used to determine the lift height from the weight change of the absorbed water. Figure 5-11 shows that the weight change results are always higher than the IR image results, and the difference becomes more significant at small lift heights. The best lift heights, 180-200 mm, are obtained from the 300 and 350 µm unit cell samples with porosities of 25.9% and 33.2% and pore sizes of 62 and 77 µm, respectively.

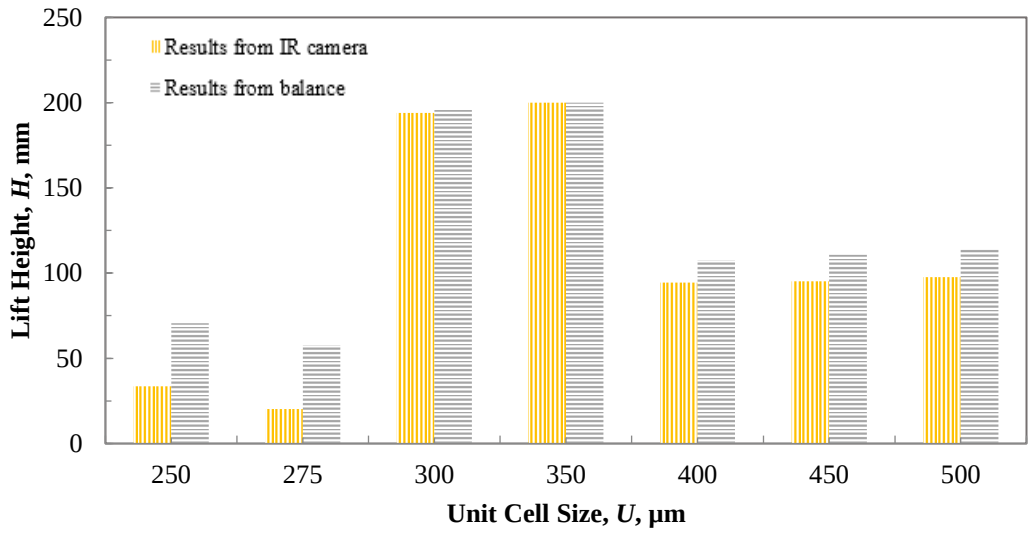

Figure 5- 11 Lift heights determined from weight change and IR camera for the CpTi samples

5.2.2 Lift Height of Samples in Ti-6Al-4V

The lift height results for the Ti-6Al-4V samples, obtained from the weight change and IR image methods, are shown in Figures 5-12 and 5-13, respectively. The values from the weight change method are always larger than the values from the IR image method. The results show that the lift height decreases when the unit cell size increases. The highest achievable lift height is 200mm, which is the height of the sample, and comes from the samples with the porosity between 19.2 - 32 % and the pore size between 44 - 67 µm.

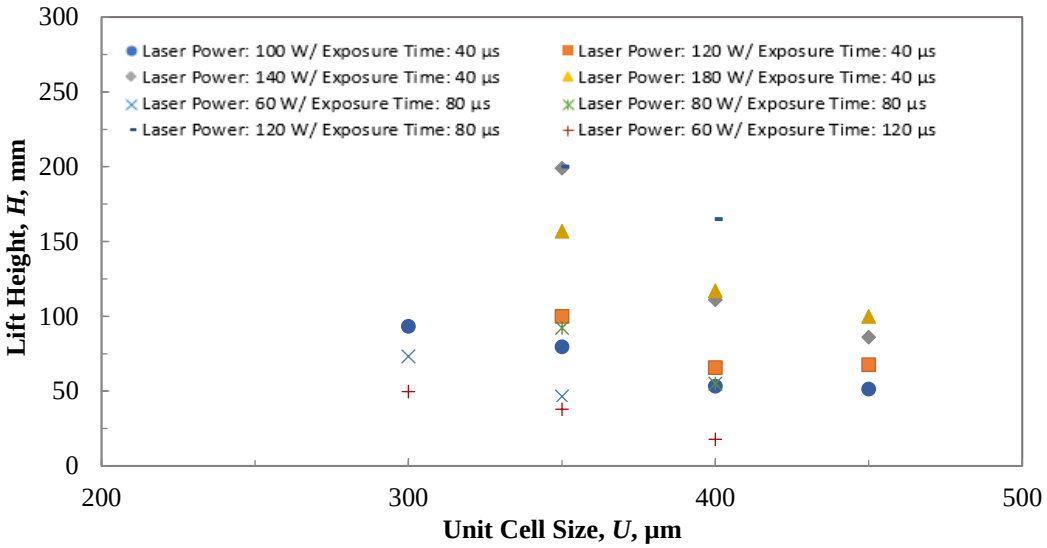

Figure 5- 12 Lift heights obtained from the weight change method for the Ti64 samples

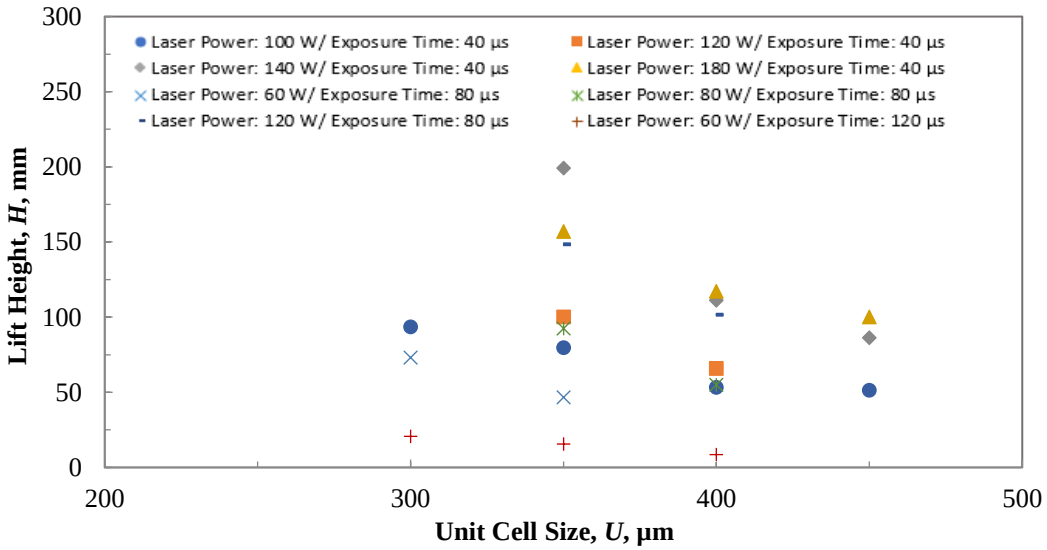

Figure 5- 13 Lift heights from the IR image method for the Ti64 samples

5.2.3 Lift Height of Other Wick Structures

As a comparison, two common types of wicks, mesh wicks and sintered powder wicks, were also analysed. The mesh wicks were manufactured and provided by the Aavid Thermacore. They are a copper mesh 150 structure, a copper mesh 200 structure, an aluminium mesh 200 structure and an SS316 mesh structure, as shown in Figure 5-14. They were folded twice to ensure the same thickness as the porous structure made by SLM, which is 1mm. All the mesh samples have the same length of 200 mm. The light

height was measured using the same IR image and weight change methods.

A sintered copper heat pipe was provided by Aavid Thermacore. It has a diameter of 12.7 mm and a length over 250 mm. The heat pipe was cut using Electrical Discharge Machining wire cutting. The sintered wick structure is shown in Figure 5-15. The porosity for the sintered copper, determined by Archimedes' method, is 52%. Only the weight change method was used to measure the lift height because a solid copper wall surrounds the wick structure and the wetted height cannot be detected by the IR camera.

Figure 5- 14 Mesh wick samples with different mesh screens and materials

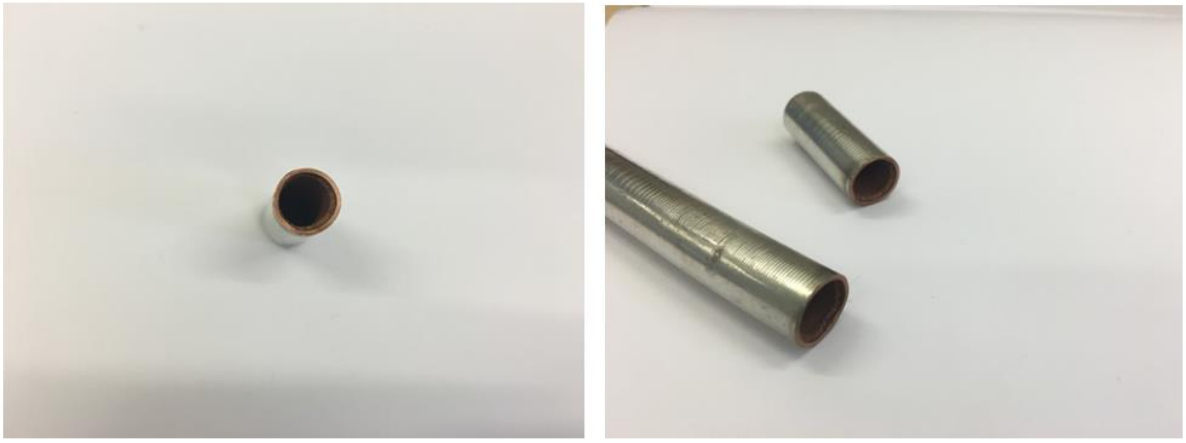

Figure 5- 15 Sintered copper heat pipe sections

The porosity and pore size values of the mesh and sintered structures are detailed in Table 5-5. The porosity and pore size were correlated to the mesh number, which is the defined number of openings per linear inch. The lift height for each structure was predicted using Jurin's Law. The results show that the predicted lift heights for sintered powder samples are higher than those for mesh structures.

Table 5- 5 Porosity, effective pore radius and calculated lift height of copper/water heat pipes (Andreas, 2008).

	Screen Mesh				**Sintered Powder**	
Mesh Type	Coarse Mesh 100	Standard Mesh 150	Fine Mesh 200	V. Fine Mesh 250	Powder Type 1	Powder Type 2
Calculated Porosity (%)	69	71	69	69	n.a.	n.a.
Effective Pore Radius(μm)	79.3	54.6	39.6	31.9	n.a.	n.a.
Calculated Lift Height (mm)	112	162	223	277	326	366

The IR images of the mesh wick samples after 10 minutes are shown in Figure 5-16. No apparent capillary action was observed in the mesh structures, except for the

copper mesh 200 sample. Even for the copper mesh 200 sample, the lift of the meniscus was very small.

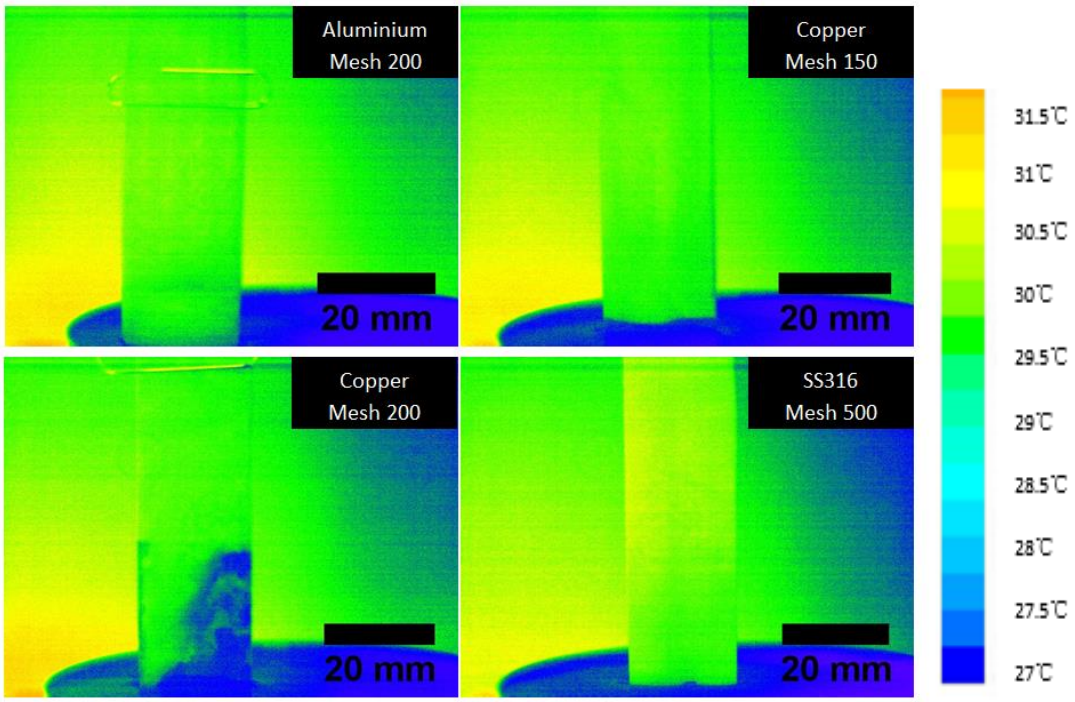

Figure 5- 16 IR images of the four mesh wick samples at 10 minutes

The lift height values obtained from the weight change method for all the mesh structures and the sintered copper heat pipe are displayed in Figure 5-17. It shows that the sintered copper wick structure is capable of lifting water to a higher level than the mesh structures as predicted in Table 5-10. The lift height for the sintered copper structure is also higher than the porous SLM structures with a similar porosity. However, the pore distribution for the sintered powder in this study is random and hard to reproduce. The capillary action is not uniform for this structure.

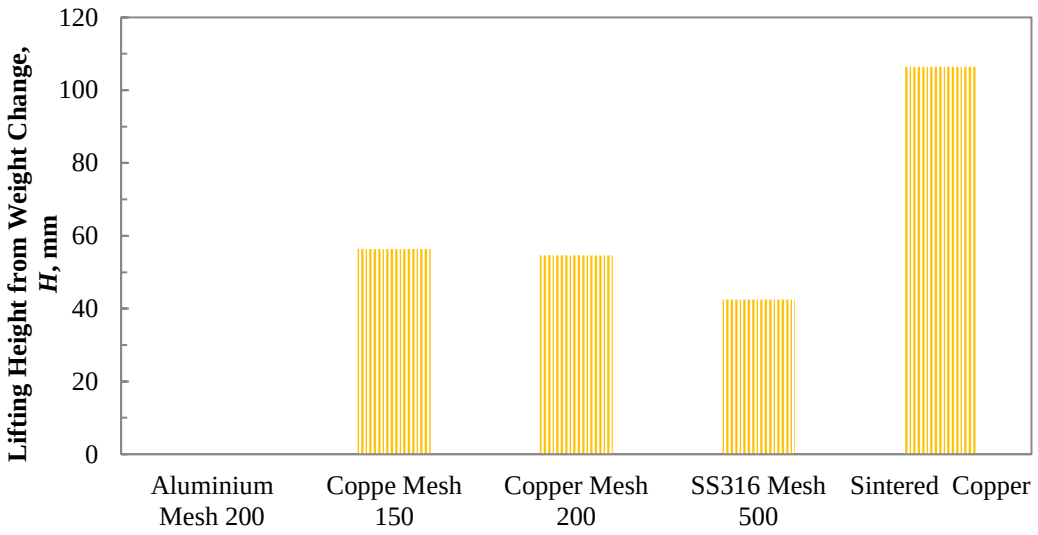

Figure 5- 17 Lift heights obtained from the weight change method for mesh and sintered structures after 1 hour

The lift height per mass values for the mesh and sintered copper samples are shown in Figure 5-18. It can be seen that the sintered sample has the lowest value, although its lift height is much higher than the mesh samples.

Mass cannot be ignored, especially in space applications. The lift height per mass values for the SLM samples in CpTi and Ti64 are calculated to be in the ranges of 11.3-35.3 and 6.1-31.6 mm/g, respectively, which are three times of those of the traditional mesh and sintered samples. The SLM porous structures benefit from the flexibility of changing manufacturing parameters and model designs.

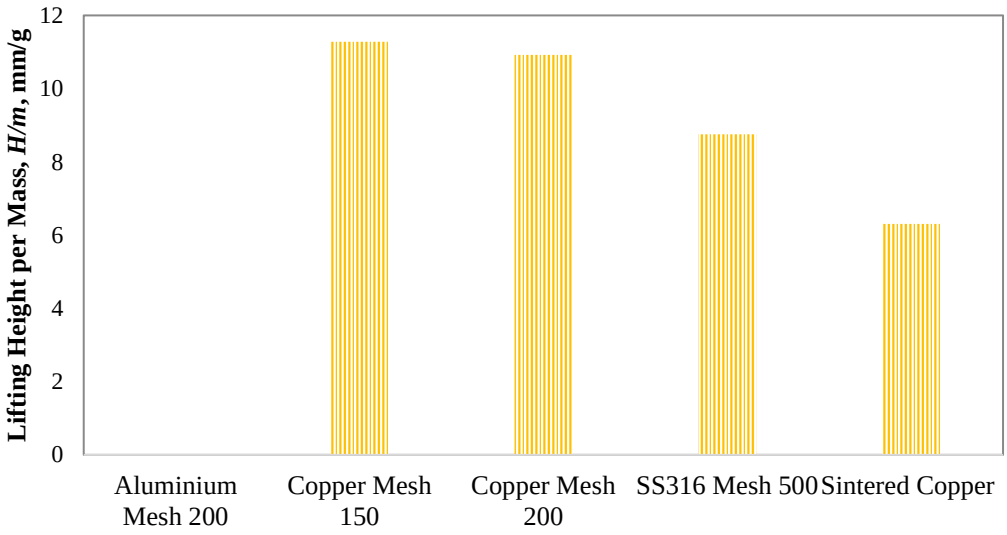

Figure 5- 18 Lift height per mass values obtained from the weight change method for the mesh and sintered structures after 1 hour

5.2.4 Discussion

In a capillary structure, the capillary force is the driving force to make the working fluid lift into the structure. There are two types of flow resistance, friction pressure loss and hydrostatic pressure loss. It is considered that the velocity of the fluid in the structure is slow and the inertial effect can be neglected, so the capillary force can be expressed as follows (Tang et al., 2010):

$$\Delta P_{cap} = \frac{\mu\varepsilon}{K} h \frac{dh}{dt} + \rho g h \qquad \text{(Equation 5-4)}$$

where μ is the viscosity of the fluid, ε is the porosity of the structure, K is the permeability of the structure, $\frac{dh}{dt}$ is the velocity of the wetted height growth, h is the wetted height, ρ is the density of the fluid and g is the gravitational acceleration. The wetted height and wetted velocity can be used to compare the capillary force for different wicks. When the equilibrium of wetted height is reached after a period of time, which is 1 hour in this study, the lift height can be used to compare the capillary force.

Figure 5-10 shows that the working fluid rose very quickly at the early stage of the

capillary process due to small friction resistance to the working fluid flow and the rate decreased with time. The fastest rate comes from the smallest unit cell size samples, 250 and 275 μm. This is because, for the same thickness, samples with smaller unit cells have more struts and pore channels (rough surface) immersed in the working fluid, providing a sizeable capillary force. Additionally, many non-fully melted particles are attached on the surface of the struts, as shown in the SEM images of the SLM porous structures in Chapter 4. Extra channels can be formed between these particles and between the particles and the struts. The wetted height is contributed from the capillary forces generated by the pores of the structure and the pores between the sintered particles. The rough surface can also help to hinder the water level dropping by trapping the fluid into the concavity. This mechanism also explains why the capillary forces in the sintered powder wick structure and the SLM porous structure are higher than that of the mesh wick. The surface of the metal wires is smooth, and the mesh is intertwined transversely and longitudinally, meaning no smooth path for the fluid to go through.

As can be seen in Figures 5-12 and 5-13, the lift height of the Ti64 samples decreased with increasing unit cell size. The results in Chapter 4 showed that, with the same manufacturing parameters, larger unit cell sizes resulted in higher porosities and larger pore sizes. A large effective pore radius of the structure would lead to a reduced capillary force, according to the Young and Laplace equation. However, it should be pointed out that the wetted heights of the CpTi samples with the 250 and 275 μm unit cell sizes were quite small even though their pore sizes are very small, 30 and 32 μm, respectively. This is because the particle size of the CpTi powder used was smaller than 45 μm so that some pores were blocked, and some closed pores were formed. Besides, these two structures have low porosities of 38.7 and 39.4%, respectively,

which means that there is a large solid fraction within the porous structure, significantly increasing the flow resistance to the fluid.

The lift height results obtained from weight change were always larger than those from IR images. It could be due to the different ways of measurement of the amount of lifted water. Since larger pores are filled more quickly, fluid uptake by the larger pores can be easily observed with the camera, whereas penetration into smaller pores at the same height occurs later (Jafari et al., 2018) and is not registered by the camera. The evaporation from the petri dish and experimental errors and noises can also contribute to the difference.

The traditional mesh samples were not capable of lifting the working fluid against gravity to the required height, whereas the sintered sample possessed high capillary actions and could pump the working fluid to a high height. However, the situation changes when the mass is taken into consideration. Although the lift height of the sintered copper sample is much higher than the mesh samples, it has the lowest lifting height per mass (Figure 5-18). Aluminium and titanium are therefore widely used in space applications, because their densities are much lower than those of copper and SS316, although the latter have superior properties in some respects such as low cost or high thermal conductivity.

5.3 Heat Transfer Coefficient

5.3.1 Heat Transfer Coefficient of Samples in CpTi

Figure 5- 19 shows the variation of heat transfer coefficient with flow rate for different unit cell CpTi structures, manufactured using the same laser power of 83 W and laser exposure time of 200 μs for the 300 and 350 μm cell size structures and the same laser power of 83 W and laser exposure time of 410 μs for the 400, 450 and 500 μm cell size samples. For all the porous structures, the heat transfer coefficient increases with

the flow rate and the difference between the maximum and minimum values can be 4-5 times. The heat transfer coefficient of samples with the smallest unit cell size, and thus a small porosity, cannot be measured at normal coolant flow rates due to the limited input pressure of water.

The results also show that the heat transfer coefficient of the 300 µm cell size structure is larger than the 350 µm cell size structure at all flow rates. The heat transfer coefficient of the 450 µm cell size structure is larger than those of the 400 and 500 µm cell size structures. The highest heat transfer coefficient occurs for the 450 µm unit cell structure, which has a porosity of 33.9% and pore size of 171 µm.

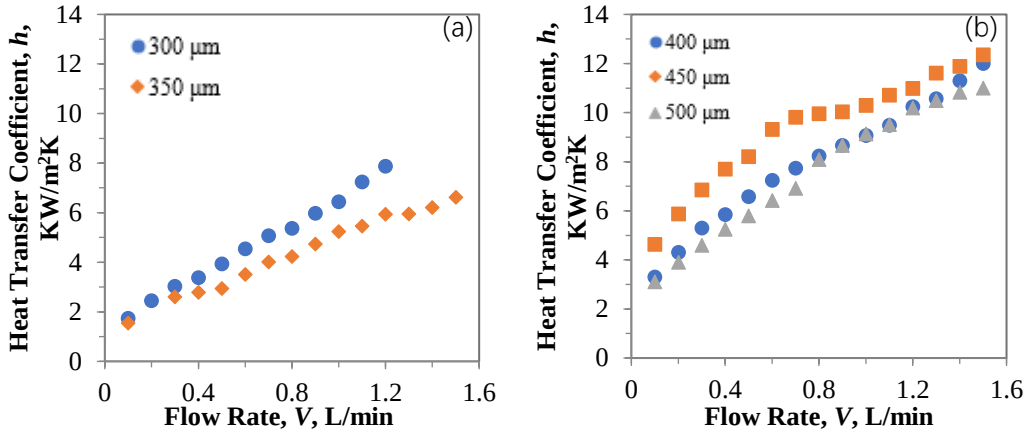

Figure 5- 19 Variation of heat transfer coefficient with flow rate for the (a) 300 and 350 µm and (b) 400, 450 and 500 µm unit cell CpTi structures

5.3.2 Heat Transfer Coefficient of Samples in Ti-6Al-4V

The variations of heat transfer coefficient with flow rate for the Ti64 samples with the 350 µm and 400 µm unit cell sizes manufactured with various laser powers in the range of 60 to 180 W and laser exposure times in the range of 40 to 200 µs are shown in Figures 5-20 and 5-21, respectively. Same as the CpTi samples, the heat transfer coefficient increases with flow rate for all the Ti64 samples, and there is no apparent trend between the laser parameters and the heat transfer coefficient. Generally, the rate of increase of heat transfer coefficient with flow rate in samples manufactured with

higher laser energy densitities is lower than that in the samples manufactured with lower laser energy densities.

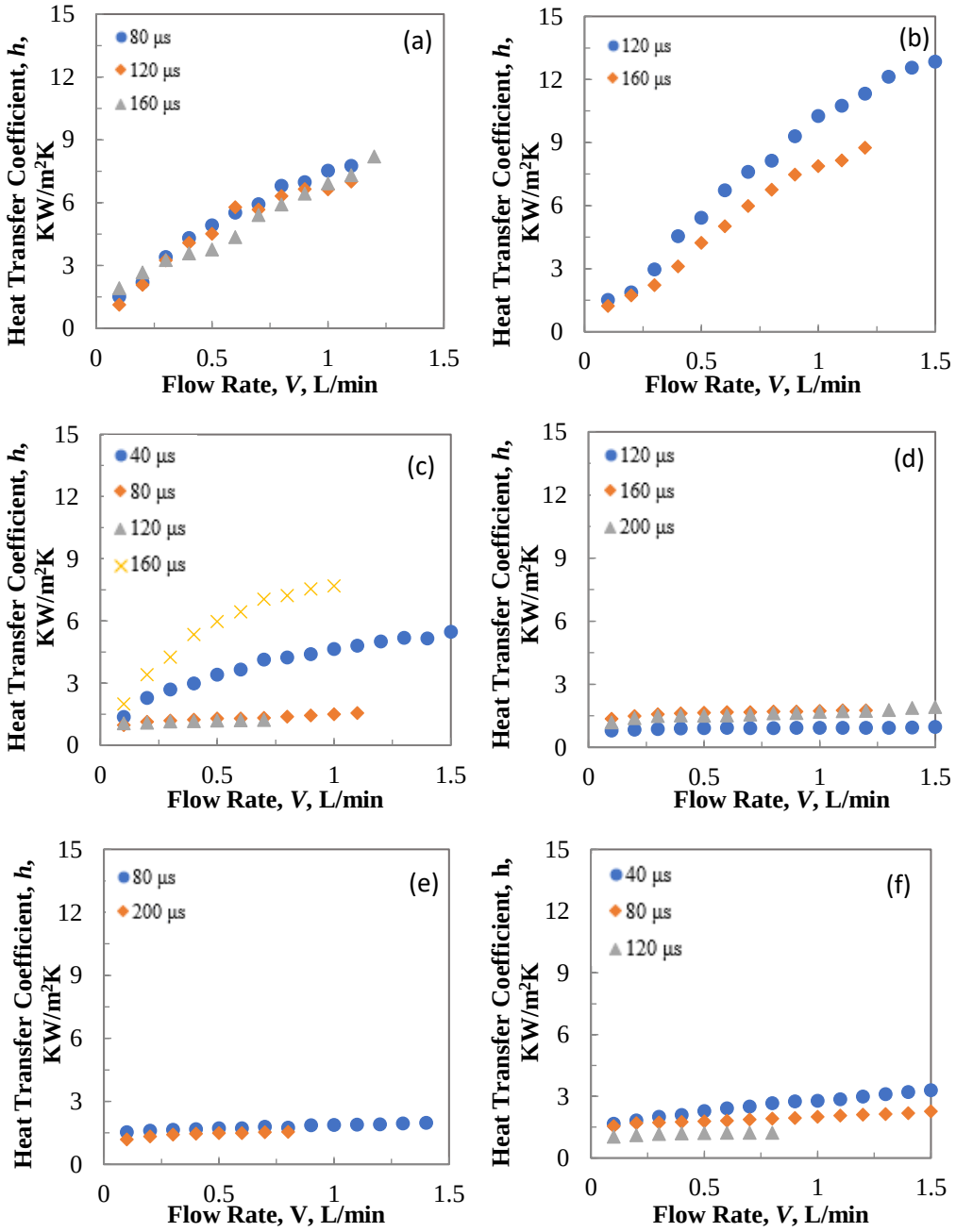

Figure 5- 20 Variation of heat transfer coefficient with flow rate for the Ti64 350 µm unit cell samples with different laser exposure times and different laser powers: (a) 60 W; (b) 80 W; (c) 120 W; (d) 140 W; (e) 160 W (f) 180 W

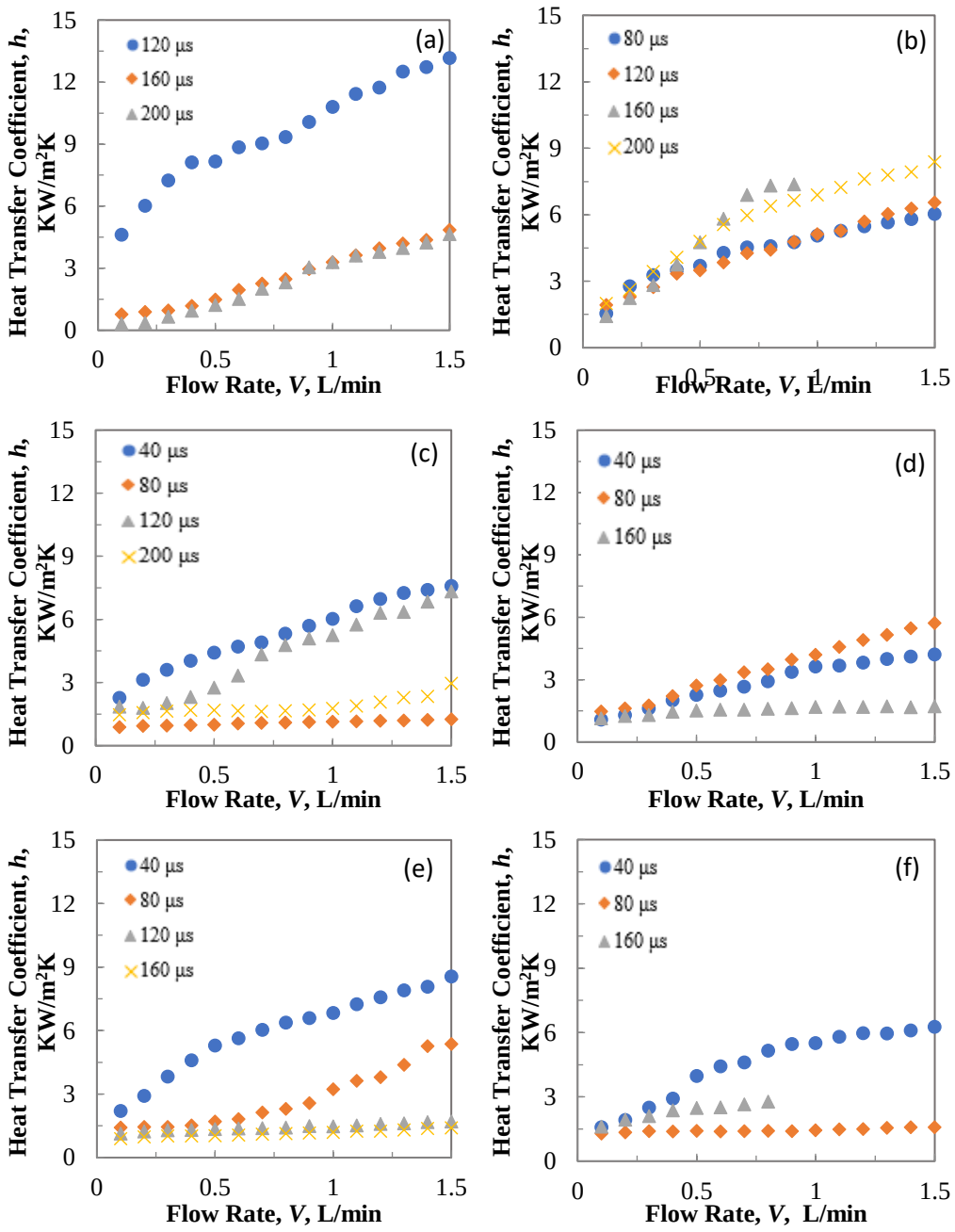

Figure 5- 21 Variation of heat transfer coefficient with flow rate for the Ti64 400 µm unit cell samples with different laser exposure times and different laser powers: (a) 60 W; (b) 80 W; (c) 120 W; (d) 140 W; (e) 160 W (f) 180 W

The largest heat transfer coefficient occurs in the 400 μm cell size sample manufactured with a laser power of 60 W and a laser exposure time of 120 μs, the corresponding porosity and pore size of which are 65.9% and 70 μm, respectively. It is evident that the heat transfer coefficient of samples manufactured with high energy densities has similar values and does not change much with flow rate.

5.3.3 Discussion

In the experiments, the input heat flux from the heat cartridges to the heating block was controlled to be 85 W/m^2. The actual input heat flux to the sample from the copper heating block was calculated according to Fourier's law:

$$Q_{in} = CA\frac{T_t - T_b}{L} \qquad \text{(Equation 5-2)}$$

where C is the heat conductivity of the copper, A is the cross-sectional area of the heat block, T_t is the temperature of the block at the top, T_b is the temperature of the block at the bottom, and L is the distance between T_t and T_b.

Figure 5-22 shows the actual input heat flux with various flow rates for CpTi 500 μm unit cell samples. The actual input heat flux is always smaller than the designed input heat flux. This difference was caused by the heat loss from the copper block during the heat transfer process due to convective heat transfer to the atmosphere, which is affected by the low air temperature around the copper block. This loss can be reduced by wrapping the block with thermal insulation materials such as calcium-magnesium-silicate wool.

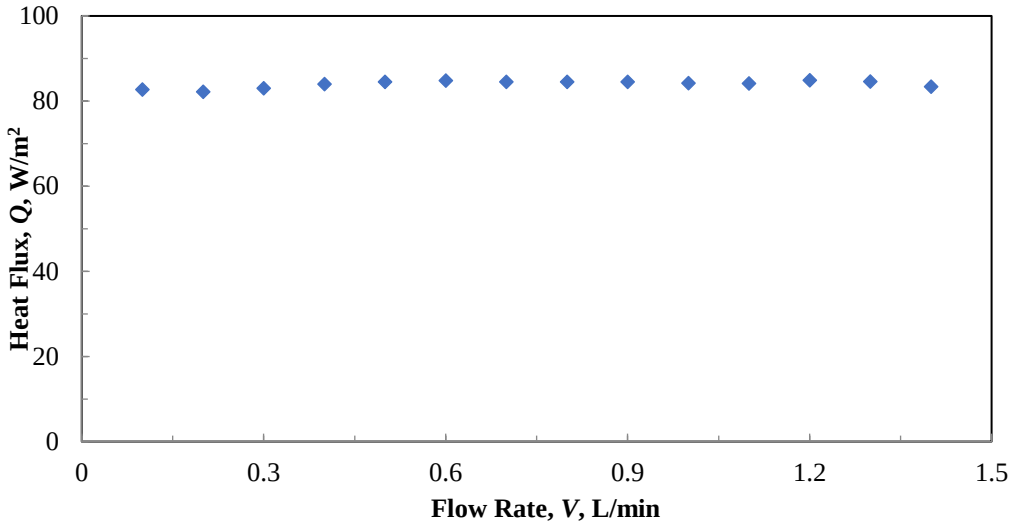

Figure 5- 22 Comparison of actual and designed input heat flux at different flow rates for the CpTi 500μm unit cell structure

This study is concerned with the performance of the SLM porous structure as a heat transfer medium from a heat source to a coolant, so the temperature difference between the porous sample and the coolant inside it is considered. Figure 5-23 shows the temperatures of the heating block at the interface with the sample and of the surrounding coolant for the CpTi 500 μm structure under different flow rates. It is shown that the temperature of the surrounding coolant remains almost constant, while the temperature of the sample decreases with the flow rate, initially dramatically and then very little after 1 L/min. It means that, when the heat source is cooled down to below a certain value, more flow is needed for further cooling. The final temperature achievable for each sample is dependent on the temperature of the heat source and can be estimated by its heat transfer coefficient.

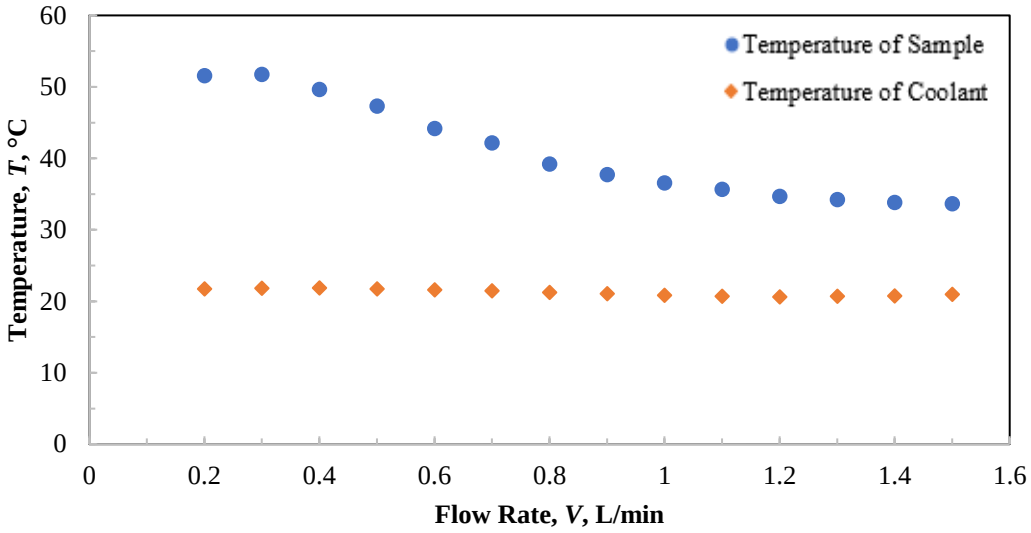

Figure 5-23 Changes in temperatures of the CpTi 500 μm unit cell sample and the surrounding coolant with flow rate

The experimental results showed that the heat transfer coefficient does not change proportionally with the unit cell size, which affects porosity and pore size. The permeability and thermal conductivity of the porous structure are important factors that can affect the heat transfer performance. The results in Chapter 5.1 showed that the permeability increases with the unit cell size, because of increased porosity and pore size. The thermal conductivity decreases with increasing porosity due to reduced volume of the solid matrix. With a low porosity, the thermal conductivity of the porous sample is high, but the internal surface area and the fluid permeability of the sample become low, resulting in inadequate heat removal of fluid. In other words, low porosity is conducive to better thermal conduction from the heat source to the porous structure but bad for convectional heat transfer from the porous structure to the coolant. In this situation, thermal convection by the coolant is the limiting factor. Therefore, the permeability is critical at low porosities. The samples with high porosities, however, have lower thermal conductivities and the limiting factor is thermal conduction in the copper matrix.

According to the research by Zhang et al. (2009), the effect of porosity on the heat transfer coefficient is more significant than the effect of pore size, and there is an optimum porosity which can achieve a balance between the thermal conduction in the solid matrix and the heat removal to the fluid. For CpTi, the best heat transfer coefficient comes from the 450 μm unit cell sample, which has a porosity of 33.9% and a pore size of 114 μm. For Ti64, the best heat transfer coefficient comes from the 400 μm unit cell sample manufactured with a laser power of 60 W and a laser exposure time of 120 μs, which has a porosity of 65.9% and a pore size of 70 μm.

A summary of the requirements for the characteristics and properties of heat pipes in this project and the experimental results for the CpTi and Ti64 porous structures is shown in Table 5-6.

Table 5-6 Summary of the porosity, pore size, permeability and capillary lift height results for the CpTi and Ti64 porous structures

Test	**Material**	**Measured Values**	**Target**	**Comment**
Porosity, φ, %	CpTi	32 - 66	-	-
	Ti64	4 - 67	-	-
Pore Size, d, μm	CpTi	28 - 166	⩽60	√
	Ti64	23 - 110		√
Permeability, K, 10^{-10} m^2	CpTi	0.1 - 37	0.01 - 1	√
	Ti64	1 - 9.5		√
Lift Height, h, mm	CpTi	70 - 200	up to 200 (150 as secondary target）	√
	Ti64	30 - 200		√

Chapter 6

Manufacture and Compatibility Test of Full-Length Heat Pipes

The research described in the previous chapters has focussed on the development of an optimised porous structure for heat pipe applications. Through this work, it has been proven that SLM technology is capable of manufacturing porous structures that exhibit excellent fluid and thermal performance and could satisfy the requirements for heat pipes for space applications.

In this chapter, the design, manufacture and development tests of heat pipes are introduced. The overall full length of the heat pipe was designed to be over 250 mm, which is over the achievable maximum height of the MCP Realizer 250 system (250 mm) but is acceptable by the Renishaw AM250 (300 mm). Ti64 was used in manufacturing the full-length height pipes.

6.1 Thermosyphon Prototypes

Before specific porous structures suitable for use as the wick structure in a heat pipe were selected, SLM trials were conducted using an SLM machine that was undergoing improvement modifications to assess the feasibility of producing full-length thermosyphons. One single piece thermosyphon prototype, with a fill tube of 6.35 mm diameter and 40 mm length, was manufactured. Fill tube is designed for working fluid charging and crimping to seal the pipe. It usually fits on the top of the thermosyphon. A hole exists on the top of the fill tube to remove as much powder as possible from the pipe. Another single piece thermosyphon prototype with a Φ3.175 mm fill tube

was manufactured as well. Although the diameter of the fill tube was changed for better crimping, the diameter of the hole was kept as 1.3 mm (it became 1.5 mm after machining) because this is the minimum size that the loose powder can pass through. However, issues arose from the crimping trials on the Ti64 thermosyphons, as brittle fractures occurred under the crimp pressure. The situation was better for the CpTi samples, but cracks were still present. It is hypothesised that titanium oxide layers may be present between the AM build layers, potentially causing embrittlement. Therefore, CpTi fill tubes machined from solid rods were selected as the preferred fill tube type for use in the test prototypes and were welded onto the Ti64 heat pipe bodies in the manufacture of the prototypes (Figure 6-1).

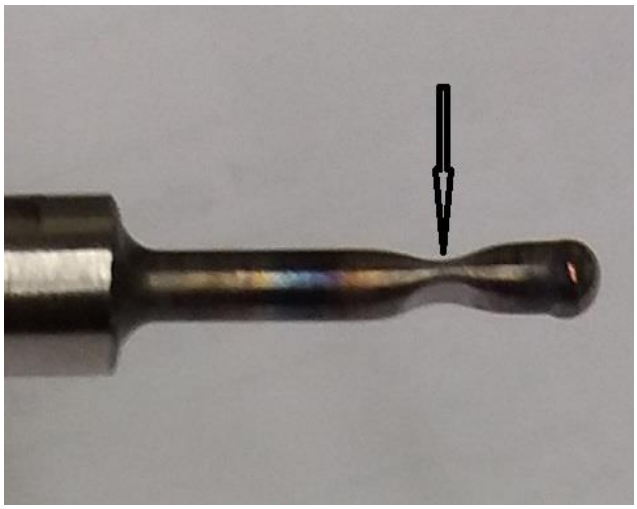

Figure 6- 1 CpTi fill tube welded onto the SLM Ti6Al4V tube

6.2 Manufacture of Sectional Heat Pipes

Trials were carried out to manufacture both the solid and porous sections of the heat pipes to produce the final geometry in one manufacturing step using the SLM process. Wick thickness is an important parameter of the heat pipe. Increasing wick thickness can increase the heat transport capability, but it increases the thermal resistance, which affects the maximum allowable evaporator heat flux. The wick structure designed in this study was 1 mm in thickness and approximately 200 mm in length. The depth of

the contact surface was 0.1 mm in the SLM manufacturing process to allow for proper integration of the solid wall and the wick structure.

After considering all the unit cell structures in Chapter 5, two types of porous structures with the unit cell size of 350 μm, as shown in Table 6-1, were selected. The porous structures were manufactured with a solid wall for observation as a section of a heat pipe. The section sample manufactured with a laser power of 140 W and a laser exposure time of 40 μs is shown in Figure 6-2.

Table 6- 1 Laser parameters and properties of the two Ti64 porous structures used for heat pipes

Laser Power, *P*, W	**Laser Exposure, t, μs**	**Porosity, *φ*, %**	**Pore Size, *d*, μm**	**Permea-bility, *K*, 10^{-10} m^2**	**Lift Height, *h*, mm**
80	80	43.3	61	4.5	92.3
140	40	24.5	44	1.2	199

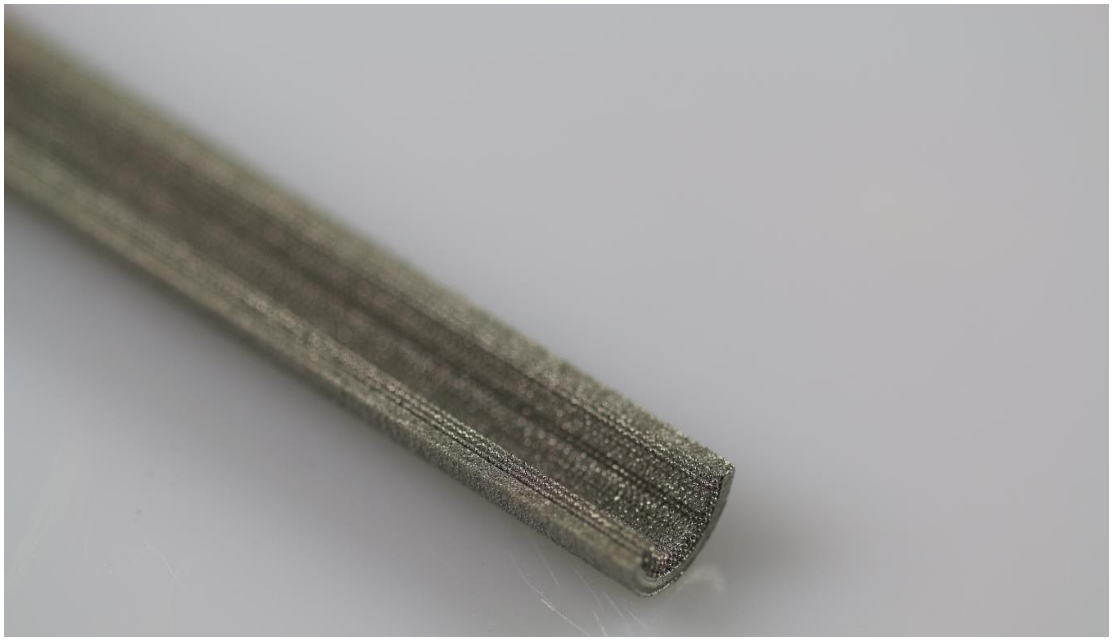

Figure 6- 2 Heat pipe section with a 350 μm unit cell wick structure

6.3 Manufacture of Full-Length Heat Pipes

Full length heat pipes based on the porous structures detailed in Table 6-1 were manufactured. Parts manufactured by SLM commonly exhibit different mechanical properties to those manufactured by conventional methods. The rapid heating and cooling processes involved in SLM typically produce parts with low yield and tensile strengths, high hardness, low fatigue strength and high residual level of residual stress (Mahmoudi et al., 2017). The parts produced using layer by layer techniques are also likely to exhibit anisotropic mechanical behaviour such that the yield, compression and tensile strengths perpendicular to layers differ to those parallel to the layers (Agarwala et al., 1995). The properties can be improved by post heat treatment.

The as-manufactured heat pipes were heat treated before removal from the substrate. Annealing, as shown in Figure 6-3, was used to decrease the undesirable residual stresses and to improve the ductility. The heat pipes were first heated to 840℃ to 860℃, held for 1 hour and then cooled naturally to 350℃ before removed from the furnace. The process was carried out under argon protective gas shielding to avoid contact with air and nitrogen.

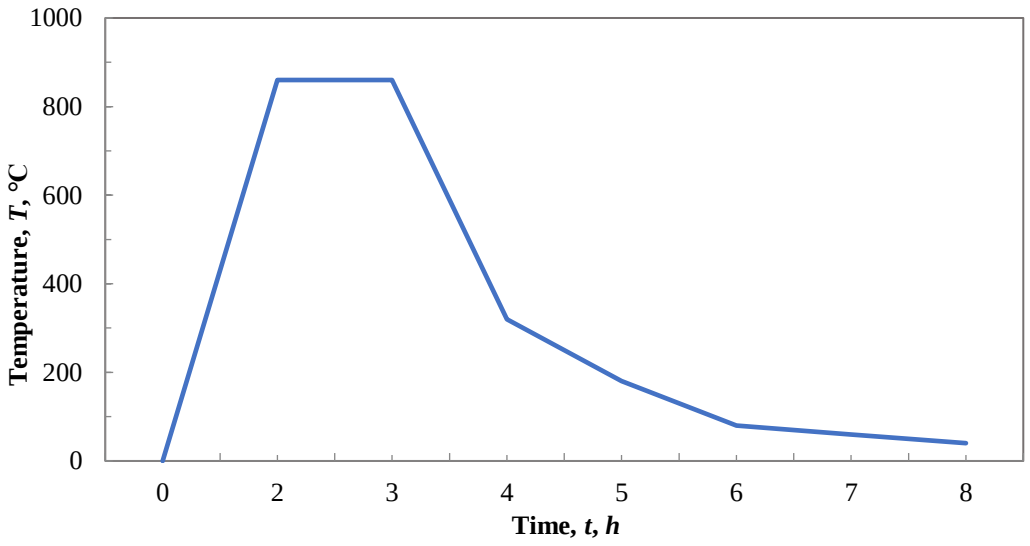

Figure 6- 3 Annealing process used for Ti64 heat pipes

The surface roughness of the SLM parts was considerably higher than that of CNC machined samples, because of many sintered metal particles attaching to the fully melted constructs. Post-manufacturing polishing was conducted to improve the rough structure. The full-length heat pipes before and after polishing are shown in Figures 6-4 and 6-5, respectively.

Figure 6- 4 As manufactured full length heat pipes with fill tubes and drilling holes

Figure 6- 5 Polished full length heat pipes

The cost of each full-length heat pipe was estimated by a Rough-Order-of-Magnitude analysis as shown in Figure 6-6, based on the predicted build times and component costs. The build rates of the Renishaw AM250 system using Ti64 powder for the solid part and the porous part are 0.5 cm^2s^{-1} and 1 cm^2s^{-1}, respectively. In estimating the associated costs for each heat pipe, the following assumptions were made:

1) The capital cost of the equipment is £300k, fully depreciates after five years.
2) Machine running cost is £10 per hour.
3) The Ti-6Al-4V powder cost is £250 per kg.

4) The cost of heat treatment is £100 per plate.
5) The time to set up the machine and to remove samples from the machine is 3 hours.
6) There is no powder wastage in the process.
7) Post-manufacture steps such as EDM part removal are not included.

Machine Information	
Build x/mm	250
Build y/mm	250
Build z/mm	300
Layer Thickness/mm	0.03
Capital Cost(£)	300,000
Per-hour Running Costs(£)	10

Build Rates (mm³/s)	
Wall	8.33
Porous Structure	16.67
Support	8.33

Component Information (mm)	
Support Height	3
Component Height	234.2
Component Footprint X	9.3
Component Footprint Y	9.3

Component Volumes (mm³)			
Build Type	Volume (mm³)	Density (%)	Melt Volume (mm³)
Wall	6770.68	100	6770.68
Porous Structure(8080)	3808.55	43	1637.68
Porous Structure(14040)	3808.55	24.5	933.09
Support	0	100	0
	Total Melt Volume (mm³)		8408.36/7703.77

Material Information			
	Price Per Kg(£)	Density (kg/m³)	Cost per mm³(£)
Ti64	250	4500	0.00113

Capacity Information	
Machine Days per Year	330
Machine Hours per Day	20
Machine Hours per Year	6600
Capital Depreciation per Year (%)	20

SLM Build Information	
Number of Components per Build	26
Total Melt Volume per Component (mm³)	8408.36
Number of Layers	7806
Total Build Time (hr)	61.02
Total Time per Component(min)	140.82

Machine Running Costs	
Depreciation per Running Hour(£)	9.09
Per-hour Running Costs(£)	10
Total Costs per Hour(£)	19.09

Post Process Costs	
Heat Treatment Costs per Plate(£)	100
Machining Costs per Unit (£)	5
Labour Cost per Hour (£)	25

Production Data	
Machine Costs per Component(£)	21.34
Running Cost per Component(£)	23.47
Material Costs per Component(£)	9.46
Post Process Cost per Component(£)	8.85
Labour Cost per Component (£)	58.67
Total Costs Per Component(£)	121.78

Figure 6- 6 Cost prediction for a full length heat pipe

6.4 Compatibility Tests

The selection of a working fluid that is compatible with the wall and wick structure material is essential. Additionally, the working fluid must have freezing and boiling points that encompass the operation temperature range and have a high latent heat, a low viscosity and a high heat transport capability. The maximum operating temperature for the heat pipes in this study is 370-400 K and the working fluid should not freeze at the minimum operating temperature of -35℃. Once the working fluid is selected, the charge mass also needs to be optimised.

Helium leak testing was conducted on the full-length heat pipes to investigate if there

was any leak in the solid wall. Proof pressure testing was then conducted to ensure the vessels could meet the proof pressure specifications. The helium leak test was repeated after proof pressure testing, before charging the pipes with the working fluid.

Non-condensable gas (NCG) tests were conducted after working fluid charge to ensure the correct amount of NCG in the hermetically sealed vessel. The tests were repeated after ageing tests. The hazard of NCG is significant because it collects in the condensing region and causes condenser blockage.

6.4.1 Charge Mass Optimisation

Ammonia was selected to be the working fluid in this study, because its boiling point and freezing point, -33.3℃ and -77.7℃ respectively, are suitable for the project. The properties of ammonia over a range of temperatures are shown in Table 6-2.

Table 6- 2 Properties of ammonia over a range of temperature (Reay et al., 2013)

Temperature, T, ℃	Liquid Density, ρ, kg/m^3	Liquid Surface Tension, -, N/m	Latent Heat, -, kJ/kg	Liquid viscosity, μ, cP	Heat Transport Capability, -, GW/m^2
-60	714.4	0.04062	1343	0.36	108
-40	690.4	0.03574	1384	0.29	118
-20	665.5	0.0309	1338	0.26	106
0	638.6	0.0248	1263	0.25	80
20	610.3	0.02133	1187	0.22	70
40	579.5	0.01833	1101	0.2	58.5
60	545.2	0.01367	1026	17	45
80	505.7	0.00767	891	0.15	23
100	455.1	0.005	699	0.11	14.5

Ammonia charging was carried out at Aavid Thermacore. The heat pipes were first cleaned to remove any residual loose powder and evacuated by a vacuum pump system. Ammonia was then introduced gently into the pipes. The pipes were vented to remove any impurities existing inside the pipes such as moisture or loose powder or reaction gas. This process was repeated three times to clean the pipes as far as possible. A hot

air gun with heating temperature up to 500℃ was used to heat the connection channel between the ammonia tank and the heat pipes to ensure that ammonia entered into the pipes completely during the charging process and any moisture in the pipes was removed during the venting process before the internal pressure became constant.

The tests for optimising ammonia charge mass were conducted by Aavid Thermacore on both heat pipe types under various charge masses, input powers and orientations. Tables 6-3 and 6-4 present the thermal test results of the two heat pipe types, respectively. The results for heat pipe with porosity of 43.3% showed that at the ammonia charge mass of 1.03 g, the heat pipe could transport the specified power of 10 W with a reasonably low temperature difference between condenser and evaporator (ΔT). Although an ammonia charge mass of 1.00 g gave a lower ΔT, it carried less power than the charge mass of 1.03 g.

Based on the thermal test data, the heat pipe wick structure manufactured with a laser power of 80 W and a laser exposure time of 80 μs, with a charged mass of 1.03 g of ammonia was selected as the preferred configuration for construction of the heat pipe test pieces required to complete the test plan. This wick structure has a higher porosity of 43.3%, which can maximise the heat transport capability. Although it cannot achieve a lift height of 150 mm for the water working fluid (see Table 6-1), the performance can be improved, as the selected working fluid in the final product is ammonia instead of water.

Table 6-3 Temperature difference as a function of ammonia charge mass, input power and orientation angle for the heat pipe with porosity of 43.3%

NH_3 Mass, m, g	Power, P, W	Angle, Θ, ˚	Temperature Difference, ΔT, ˚C
1.5	10.16	-0.3	12.02
	5.66	-5	23.46
	4.06	-10	22.85
	2.91	-15	19.74
	2.12	-20	18.57
1.4	10.39	-0.3	6.04
	6.28	-5	16.96
	4.06	-10	16.14
	3.44	-15	15.57
	2.79	-20	15.13
1.35	10.65	-0.3	4.39
	6.23	-5	18.63
	4.85	-10	15.13
	3.89	-15	8.62
	3.42	-20	7.61
1.29	10.37	-0.3	5.02
	7.37	-5	13.57
	5.87	-10	10.23
	5.21	-15	10.11
	4.31	-20	9.74
1.23	10.57	-0.3	5.12
	7.45	-5	11.41
	6.1	-10	10.64
	5.06	-15	6.68
	4.5	-20	4.19
1.2	10.35	-0.3	3.54
	7.93	-5	12.37
	6.64	-10	7.71
	6.29	-15	6.94
	4.78	-20	5.31
	3.23	-25	4.33
1.14	10.27	-0.3	3.05
	8.53	-5	7.34
	7.35	-10	6.64
	5.88	-15	5.27
	4.71	-20	4.96
	3.61	-25	3.25
1.1	10.73	-0.3	4.05
	7.89	-5	5.74
	7.23	-10	3.74
	6.37	-15	4.59
	5.54	-20	3.35
	4.42	-25	3.26
1.03	10.07	-0.3	3.08
	8.86	-5	3.35
	6.89	-10	3.61
	5.85	-15	2.04
	5.09	-20	1.93
	4.27	-25	2.03
1	9.49	-0.3	3.35
	7.87	-5	1.72
	6.55	-10	1.5
	6.06	-15	0.97
	4.82	-20	0.86
	3.26	-25	0.8
0.95	8.34	-0.3	1.42
	6.88	-5	2.09
	5.99	-10	2.21
	5.12	-15	1.69
	3.87	-20	2.41
	3.12	-25	1
0.89	5.91	-0.3	3.23
	4.24	-5	1.69
	3.19	-10	1.02

Table 6- 4 Temperature difference as a function of ammonia charge mass, input power and orientation angle for the heat pipe with porosity of 24.5%

NH_3 Mass, m, g	Power, P, W	Angle, θ, ˚	Temperature Difference, ΔT, ˚C
1.48	1.52	-0.4	15.55
1.38	1.75	-0.4	2.6
1.17	10.01	-0.3	7.79
	0.59	-5	20.78
1.08	10.86	-0.3	7.26
	0.93	-5	19.52
1	11.27	-0.3	5.58
	1.72	-5	23.04
0.91	10.79	-0.3	4.73
	1.55	-5	16.25
0.86	10.6	-0.4	5.24
	0.95	-5	9.67
0.81	8.33	-0.3	19.06
	0.83	-5	0.63

6.4.2 Helium Leakage and Proof Pressure Tests

The helium leakage, proof pressure and burst pressure tests were conducted at Aavid Thermacore to ensure that the vessel materials were hermetically sealed and the fill tube weld joints had no leaks. The helium leakage tests were conducted using the bag method. Pfeiffer Smart Test HLT 560 leak detector (Pfeiffer Vacuum, Germany) was used to produce a vacuum and to record the leak rates. The heat pipe was first evacuated by the vacuum pumping system and the detector was then valved in. The heat pipe was placed in an enclosure full of helium to detect any leak. The parts were considered to have failed to pass the test if the helium leak rate was more than 10^{-8} mbar 1/s. The helium leak rates for all the samples, as shown in Table 6-5, were less than 10^{-8} mbar 1/s, demonstrating that there was no leakage in the pipes manufactured by SLM.

Table 6- 5 Proof pressure test results for SLM Ti64 heat pipes.

Sample Number	**Proof Pressure, *P*, bar**	**Maximum Ratio of Post Dimension / Pre-Dimension *(Pass: value ⩽ 1.002)***	**Helium Leak Rate, -, mbar l/s *(Pass: value ⩽10^{-8})***
1	77.12	1.0006	$<1.8 \times 10^{-9}$
2	79.92	1.0006	$<7.0 \times 10^{-10}$
3	79.86	1.0001	$<1.2 \times 10^{-9}$
4	79.90	1.0005	$<1.5 \times 10^{-9}$
5	79.48	1.0000	$<8.0 \times 10^{-10}$
6	76.80	1.0003	$<1.2 \times 10^{-9}$

The proof pressure tests were conducted using a high-pressure nitrogen system to maintain an internal pressure above the proof pressure specification for 15 minutes. The maximum design temperature of the heat pipe in this study is 90℃ and the pressure specification is the corresponding vapour saturation pressure for the specific working fluid. For ammonia, the internal pressure is approximately 70 bar. Before the test, the diameters of the heat pipe were measured using a micrometre at locations one inch from each end of the flange, at two sides 90° apart for each marked location. Nitrogen was gently introduced into the heat pipe to raise the internal pressure to the proof pressure, which was held for 15 minutes. The pressure was then relieved and the diameter of the pipe was measured again using a micrometre at each of the locations. The maximum ratio of post-dimension to pre-dimension for each heat pipe is shown in Table 6-2. The maximum ratios of post/pre-dimensions of all the samples were well below 1.002, confirming that all the heat pipes passed the proof pressure tests.

The burst pressure test was conducted on one sample only and the results are shown in Table 6-6. It was completed using a hydraulic water pump system. The initial proof pressure test on the sample at 76.75 Bar (about 1.5 times the maximum design pressure

) the bar showed a maximum strain ratio of 1.0005. The sample was then subjected to a burst pressure of 140 bar (above 2.5 times the maximum design pressure) and showed a strain ratio of 1.0003, indicating a pass. As per the test requirement, a third test was conducted where the pressure was increased to identify the failure point (burst pressure). However, the sample had not failed at 200 bar, at which the strain ratio was measured as 1.0005. It can be concluded that a significant reduction in heat pipe wall thickness can be realised in future AM heat pipes. Wall thickness reduction can yield mass reduction and temperature difference reduction in the heat pipe. By maintaining the outside diameter, wall thickness reduction increases the inside diameter and wick volume, which may yield an increase in transport power due to increased mass flow rate of condensate.

Table 6- 6 Burst pressure test results for SLM Ti64 heat pipe

Sample Number	Test Pressure, *P*, bar	Maximum Ratio of Post Dimension / Pre-Dimension
7	80	1.0005
	140	1.0003
	200	1.0005

6.4.3 Non-Condensable Gas Test

Non-condensable gas (NCG) is considered as the leading cause for degrading the thermal performance and reducing the lifespan of the heat pipes. Generally, NCG consists of nitrogen, hydrogen, light hydrocarbons, carbon dioxide or other gaseous materials (He et al., 2014). NCG can be stored in the condenser section of a heat pipe, blocking a portion of the condenser. Figure 6-7 shows schematically the change of volume ratio between NCG and ammonia in a heat pipe when the temperature is decreased from 20 to -30℃. At a higher temperature, the vapour pressure of ammonia causes compression of the NCG. The vapour pressure is reduced by cooling the pipe

since the vapour saturation pressure for ammonia is about 20 bar at room temperature and 1 bar at -30℃. It causes NCG expanding along the condenser section, leading to a decrease in the effective length of heat pipe.

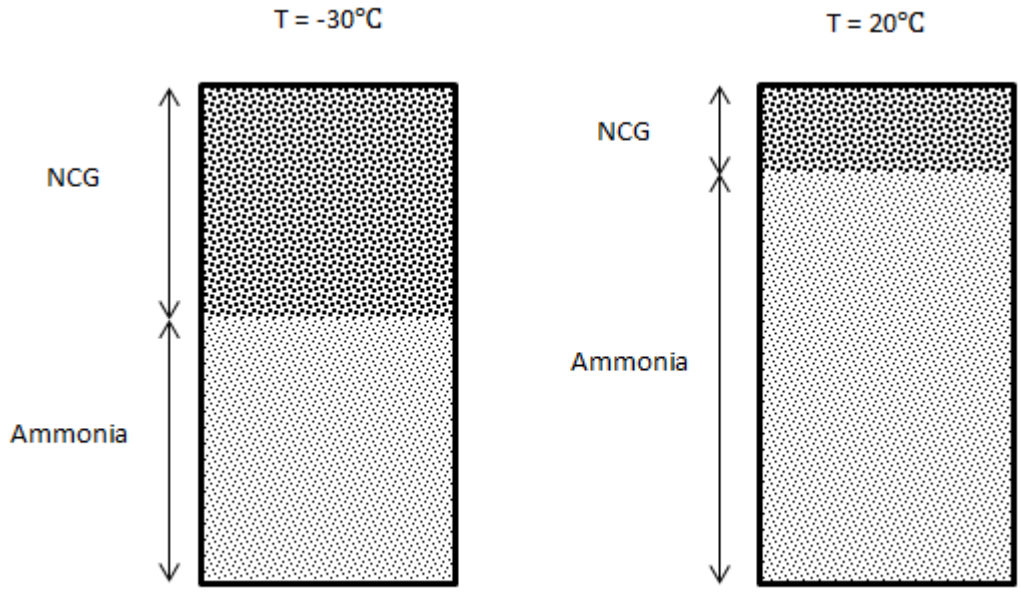

Figure 6- 7 Schematic of volume changes of NCG and ammonia caused by different temperatures

The NCG test rig used in this study consists of a heater block at the evaporator end of the heat pipe and a liquid-cooled condenser block that is chilled by a coolant supplied by a refrigeration unit. The NCG test was carried out with the test pipe operating with a heat load of 2 W at -30℃. Six thermocouples were attached to the condenser section of the pipe to measure the temperature differences along the heat pipe length. The first thermocouple was located at 5 mm from the end of the condenser section and the other thermocouples were located at an increment of 2.5 mm from the previous one.

The NCG tests were conducted at the following inspection points during the manufacturing process to check if NCG was generated: (1) after ammonia charging

(Pre-NCG), (2) after ageing (Post-NCG 1), and (3) after crimping and hot proof pressure test (Post-NCG 2). In this study, the charged heat pipes were subjected to a 300 hours ageing (burn-in) process at a temperature of 100℃ to 105℃ (maximum heat pipe storage temperature).

Figure 6-8 shows the temperature readings along the heat pipe length, from the evaporator section to the condenser section, i.e. the top NCG observation area, for five SLM Ti64 ammonia heat pipes. The temperature profiles are relatively flat. Although a dip occurs at the NCG observation area, the temperature difference along the pipe is within the specification.

The test data for the temperature difference in the condenser section are listed in Table 6-7 to check against the first pass/fail criterion that the condenser temperature difference must be < 2°C. The test data for the temperature difference between the condenser section and the remainder are listed in Table 6-8 to check against the second pass/fail criterion that the difference between the average temperature of the condenser section and the average temperature of the remainder of the heat pipe must be ⩽ 2°C.

The second criterion is to analyse whether a large volume of NCG is generated that extends outside of the condenser section.

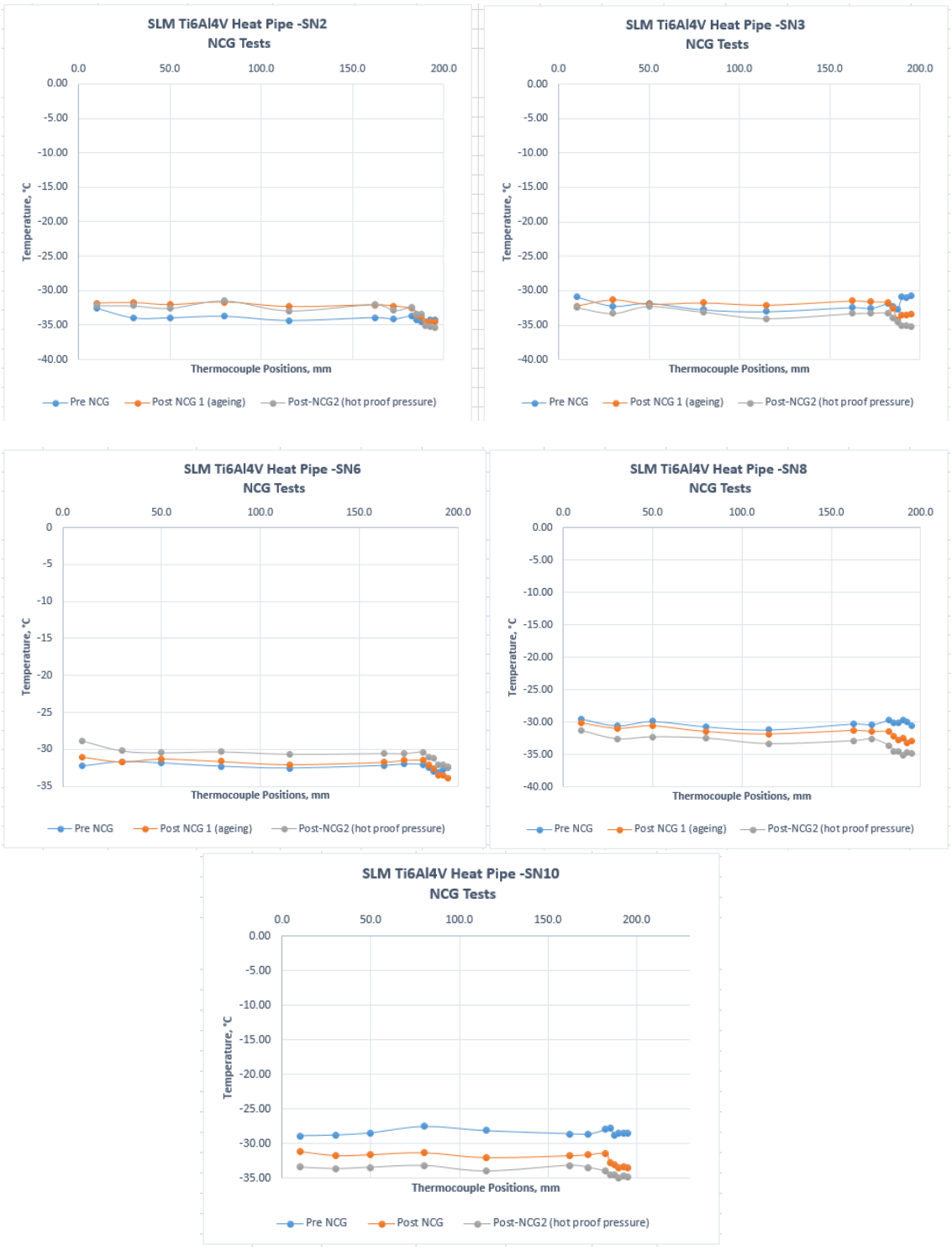

Figure 6-8 Temperature change along the heat pipe length in NCG test (5 samples)

All the heat pipes showed temperature differences below 2°C and therefore passed the two criteria in each stage of the NCG test. The temperature difference for SN3 is at the pass/fail limit but is unaffected by the ageing and proof pressure tests, indicating that ageing has not generated NCG. Sample 6 showed a test failure after ageing and

was therefore deselected for installation into the final heat pipe assembly, although the final post proof pressure temperature test result was within specification.

The high-temperature differences observed across the condenser section may be either due to the properties of the titanium heat pipe vessel or due to the condenser design. The condenser design is proposed to be evolved in a future study. A specific standard test procedure also needs to be created for miniature heat pipes.

Table 6- 7 Temperature differences in the condenser section of SLM Ti64 heat pipes

Sample Number	**NH_3 Charge Mass, *m*, g**	**Temperature Difference**			**Pass/ Fail**
		Pre-NCG – $\Delta T_{NCG\text{-}CON}$ (Unsealed Pipe), °C	**Post-NCG1 (ageing) – $\Delta T_{NCG\text{-}CON}$** (Unsealed Pipe) °C	**Post-NCG2 (hot pressure)- $\Delta T_{NCG\text{-}CON}$** (Sealed Pipe) °C	
1	1.03	2.33	1.83	Failed Crimping Process	N/A
2	1.05	1.03	1.91	1.79	Pass
3	1.04	2.00	1.87	1.99	Pass
4	1.05	1.07	2.34	1.98	Pass
5	1.04	0.88	1.74	1.50	Pass
6	1.03	1.11	1.36	1.05	Pass

Table 6- 8 Temperature differences between the condenser section and the remainder of SLM Ti64 heat pipes

Sample Number	NH_3 Charge Mass, *m*, g	Temperature Difference			Pass/ Fail
		Pre-NCG – $\Delta T_{NCG\text{-}CON}$ (Unsealed Pipe), °C	Post-NCG1 (ageing) – $\Delta T_{NCG\text{-}CON}$ (Unsealed Pipe) °C	Post-NCG2 (hot pressure)- $\Delta T_{NCG\text{-}CON}$ (Sealed Pipe) °C	
1	1.03	0.64	1.29	Failed Crimping Process	N/A
2	1.05	0.45	1.90	1.85	Pass
3	1.04	0.69	1.50	1.27	Pass
4	1.05	0.58	1.19	1.05	Pass
5	1.04	0.35	1.39	1.84	Pass
6	1.03	0.08	1.33	1.14	Pass

6.5 Thermal Test

The final heat pipe assembly is required to carry 30 W through three heat pipes (10 W each). The purpose of the thermal test is to verify each heat pipe's capability of transporting a heat load of 10 W under various operating conditions such as orientation angle and operating temperature. To achieve this goal, thermal angle tests and power tests were conducted.

6.5.1 Thermal Angle Tests

The test rig used for the thermal tests was designed to operate at different test angles. Figure 6-9 shows the thermocouple positions for the tests at a vertical orientation: 4 in the condenser section, 2 in the adiabatic section, 4 in the evaporator section and 2 at the inlet and outlet of the condenser cooling loop to monitor the inlet and outlet water temperatures. A mass flow meter was used to measure the water flow rate through the cold condenser plate, enabling an energy balance to be completed to determine the heat transported through the heat pipe. Besides, thermocouples (not included in the

schematic) were attached to the fill tube and valve body and monitored by a portable temperature monitor to ensure that the temperatures were sufficiently high to prevent condensation of the working fluid in the valve region, i.e., heat pipe dry-out.

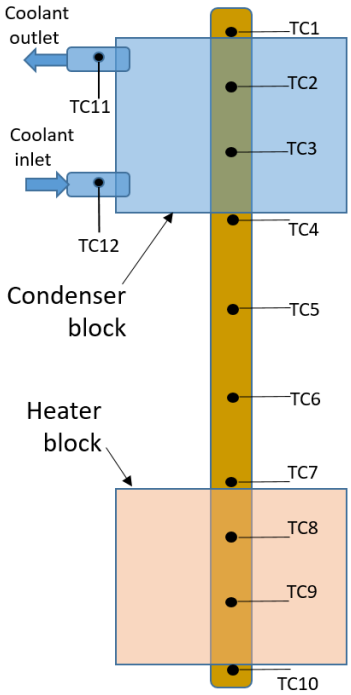

Figure 6-9 Thermocouple positions on an SLM heat pipe for thermal test

During the thermal test, the entire enclosure was packed with insulation to minimise heat loss from the system. For un-crimped heat pipes, as there was an ample void space within the valve region, a heater was deployed to heat the valve to prevent the collection of ammonia in this region, which could cause heat pipe dry-out and thus affect the test results.

Changing the angle of the heat pipe varies the lift height requirement when functioning against gravity. The thermal angle test was conducted to observe the effect of inclination angle on the thermal performance of the SLM heat pipe. The test conditions were:

1) Heat pipe target power load = 10 W
2) Operating temperature = 60˚C

3) Operating angles:
    a) +90˚ (gravity aided)
    b) -0.3˚ (simulated space environment with no gravity)
    c) $-\theta_{max}$ (largest negative angle the heat pipe is functional against gravity, determined by multiple tests)

Table 6-9 shows the angle test results. Samples 3, 4, 5 and 6 were fully tested, both before and after crimping. Comparing the pre- and post-crimping results shows that the temperature difference increased slightly after the crimping and sealing process, probably due to a slight loss in ammonia during crimping that was trapped in the valve area.

The variation of thermal transport capacity with inclination angle is shown in Figure 6-10. All the four heat pipes (Samples 3, 4, 5 and 6) could transport the required 10 W heat load with gravity aided return of the working fluid (angle = +90°), with low temperature differences between the two ends of the heat pipe. Under the adverse tilt condition (angle = -0.3°), Samples 3, 4 and 5 were able to transport the required 10 W heat load, but the temperature difference was elevated to ≈ 10°C. Sample 6 was able to transport 8.40 W, showing a significant reduction after crimping. The heat pipes can function at angles of -5° and -15° against gravity but with reduced transport capacity. Sample 4 was able to function at an angle of -20° against gravity with a transport power of 4.44 W and temperature difference of 7.9°C, indicating the potential to improve the performance of the heat pipe in the future.

Table 6- 9 Angle test results

Serial Number	Process	Test Angle, Θ, °	Power Input, P_{in}, W	Power Output, P_{out}, W	Heat Loss, -, %	Temperature Difference $\Delta T_{evap\text{-}cond}$, °C
1	Pre Crimp	90	16.00	10.41	34.94%	5.99
		-0.3	13.00	8.00	38.46%	3.93
		-5	11.50	5.65	50.87%	3.09
	Failed crimping process, no further test conducted.					
2	Pre Crimp	90	16.80	10.46	37.74%	1.87
		-0.3	15.50	8.27	46.65%	7.80
		-5	10.60	2.43	77.08%	10.92
	Progressed to subsequent power tests, without completing the post-crimping thermal tests, due to scheduling constraints					
3	Pre Crimp	90	16.00	11.07	30.81%	1.49
		-0.3	16.00	10.30	35.63%	4.51
		-5	13.40	7.66	42.84%	7.67
	Post Crimp	90	18.00	10.54	41.44%	2.54
		-0.3	17.00	10.15	40.29%	8.28
		-5	13.50	6.58	51.26%	8.95
		-15	9.00	3.67	59.22%	6.10
4	Pre Crimp	90	17.00	11.34	33.29%	-0.46
		-0.3	15.10	8.93	40.86%	5.40
		-5	13.20	7.05	46.59%	6.77
	Post Crimp	90	17.00	10.73	36.88%	1.52
		-0.3	16.00	10.09	36.94%	9.81
		-5	13.20	7.83	40.68%	9.63
		-15	10.50	7.26	30.86%	6.88
		-20	9.00	4.44	50.67%	5.53
5	Pre Crimp	90	17.00	10.73	36.88%	-0.14
		-0.3	16.00	10.93	31.69%	4.26
		-5	11.00	6.01	45.36%	8.84
	Post Crimp	90	18.00	10.34	42.56%	3.16
		-0.3	17.00	10.33	39.24%	7.50
		-5	13.00	6.56	49.54%	10.02
		-15	7.50	1.80	76.00%	3.47
6	Pre Crimp	90	16.00	10.47	34.56%	1.54
		-0.3	16.00	10.27	35.81%	5.62
		-5	11.50	6.60	42.61%	8.05
	Post Crimp	90	17.00	10.66	37.29%	3.26
		-0.3	14.00	8.35	40.36%	7.26
		-5	10.80	5.11	52.69%	6.39
		-15	8.40	2.08	75.24%	2.44

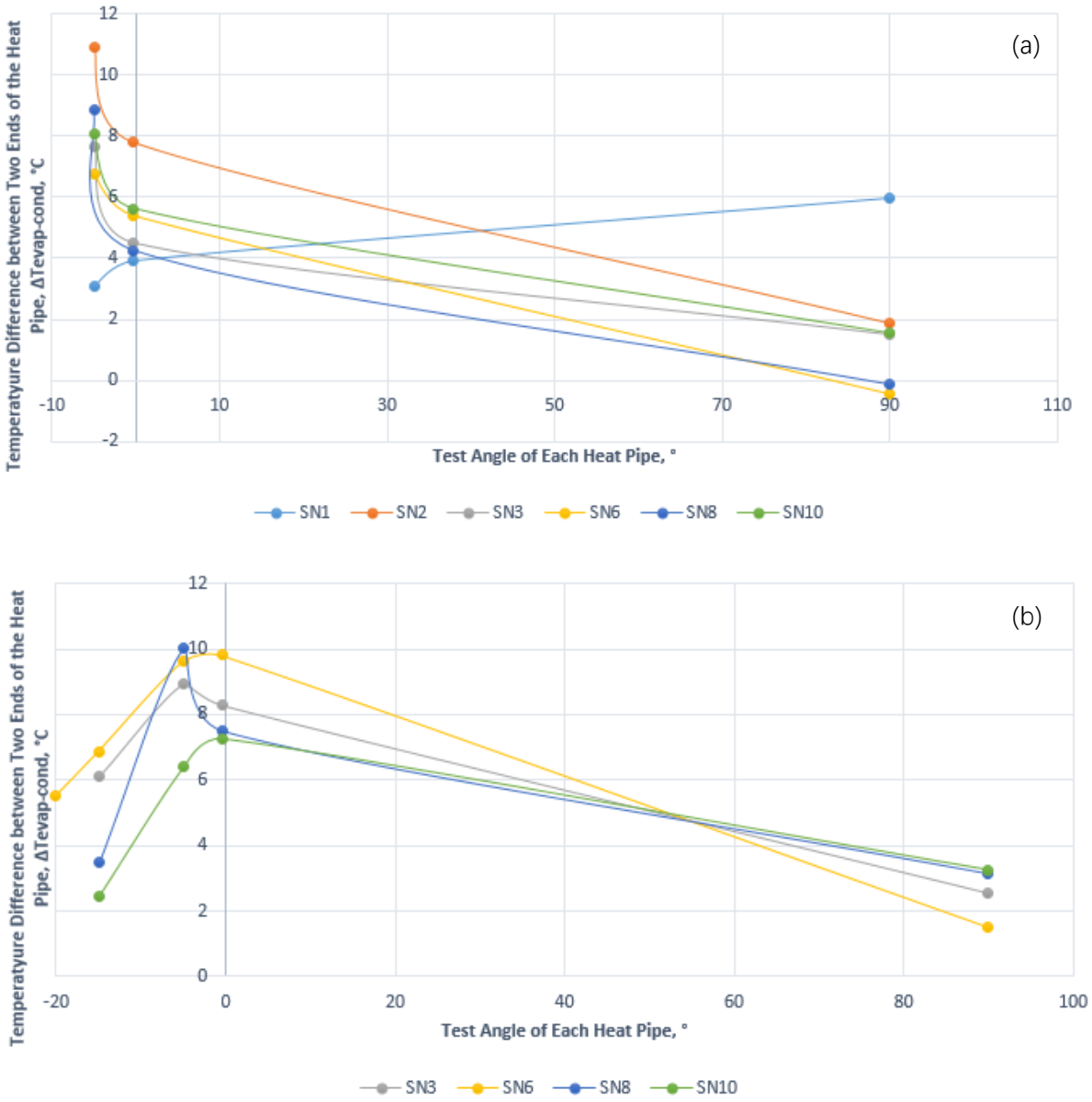

(b)

Figure 6-10 Temperature difference against operating angle (a) pre-crimping and (b) post-crimping

6.5.2 Power Test

Preliminary power tests were conducted on the individual SLM heat pipes after sealing (crimping and welding) of the fill tubes to investigate the effects of operating power and operating temperature on their thermal performance. Five heat pipes (Samples 2, 3, 4, 5 and 6) were tested at a fixed inclination angle of -0.3° at temperatures of 25°C and 60°C to simulate the conditions in space / zero gravity environment.

The power test results are summarised in Table 6-10. At the operating temperature of 25°C, all the heat pipes performed well. Only Sample 2 showed a temperature difference higher than 5°C at a transport power of 10W. At the operating temperature of 60°C, all the heat pipes showed a higher temperature difference.

Table 6- 10 Summary of preliminary power test results at -0.3° operating angle

Operating Temperature, *T*, °C	Serial Number		Operating Power, *P*, W		
			8	9	10
25	2	ΔT evap-cond, °C	4.56	4.90	5.68
	3		3.30	3.61	3.89
	4		2.83	3.26	3.59
	5		3.61	4.07	4.30
	6		3.35	3.69	4.43
60	2	ΔT evap-cond, °C	5.78	6.27	6.76
	3		4.95	6.75	8.44
	4		4.07	4.39	5.65
	5		7.44	8.70	9.63

6.6 Summary

The heat pipes manufactured by SLM have passed the relevant compatibility and thermal tests. The tests demonstrated the feasibility of producing full length heat pipes for space applications. The proof pressure tests indicated that the diameter of the heat pipe can be changed to achieve a thicker wick structure and a thinner solid wall to further improve the thermal performance of the heat pipe because of enhanced thermal convection, as long as the solid part can retain sufficient mechanical properties. The thermal tests showed that the heat pipes filled with the ammonia working fluid can work with an angle of 15°, beyond which dryout could occur at the evaporation part.

Chapter 7

Conclusions and Future Work

This research project involved developing the Selective Laser Melting process and defining an appropriate set of processing parameters to enable the manufacture of wick structure in a heat pipe application which can work against gravity. The relationship between the characteristics of the structure and the properties, including permeability, capillary force and heat transfer, has been investigated. The optimal structures based on the experimental results were used to manufacture full-length heat pipes. Compatibility and thermal tests were conducted on the heat pipes to assess their integral performance.

7.1 Porous Structures Manufactured by SLM

An octahedral unit cell approach has been designed and developed by the University of Liverpool. Structures based on this approach are preferable for the heat pipe application because the predicted unit cell size is larger than the others, so it is easier for SLM to produce parts meeting the relevant requirements.

The strut diameter, porosity and pore size of CpTi and Ti64 porous structures with various unit cells and process parameters were investigated. Strut diameter was highly dependent on laser energy density, especially laser power. Porosity and pore size normally changed with the unit cell size and laser parameters in a similar trend. Double scanning increased the strut diameter and decreased the porosity and pore size because of the enlargement of the melt pool. Double scanning worsened the strut surface quality because more powder in the low-sintered zone was exposed to the heat and then attached to the struts.

Pore size of the porous structures needs to be smaller than 60 μm to achieve a high capillary action. Both CpTi and Ti64 porous structures could be manufactured to meet the requirement by decreasing the unit cell size and increasing the laser energy density during the manufacturing process. However, small unit cells can increase the difficulty of SLM manufacturing and increasing laser energy density increases the existence of defects in the structure. The optimal structures were the 300 and 350 μm unit cells manufactured with a relatively high laser energy density.

7.2 Fluid and Thermal Properties of SLM Porous Structures

The pressure drops over the length of sample was measured for different porous structures. The pressure drops increased with flow rate and followed a quadratic function. Samples with larger unit cells had smaller pressure drops than samples with smaller unit cells because they have high porosities and large pore sizes and therefore less resistance to the fluid flow.

It was found that the fluid flow in the porous structure can be divided into three regimes based on the relationship between the reduced pressure drop and Darcy velocity. The regimes corresponded to laminar, transitional and turbulent flows. Permeability was determined using the Forchhermer equation for different porous structures, for both the transitional and turbulent flow regimes. It was found that permeability increased with the unit cell size. The permeability for the transitional flow was always larger than for the turbulent flow, because the interaction between the fluid and the solid structure in Darcy flow was weak, causing less energy dissipation. With increasing velocity, the flow changed into turbulent with irregular fluctuations, resulting in decreased mass transfer efficiency.

The lift height of water in the porous structures due to capillary force was measured using both the height-change and weight-change methods. Water rose rapidly at the

early stage of the capillary process due to small friction resistance and the rising rate decreased with time. The highest height was reached after about 1 hour for all the samples. The lift height decreased with the unit cell size because low porosity and small pore size offered limited valid path of flow and more considerable friction resistance. The lift heights in four typical mesh wicks and a copper sintered wick structure were also measured. The results showed that the sintered sample had the highest capillary force while no apparent lift was observed in the mesh structures, confirming that surface roughness had a positive effect on the capillary action. However, the mesh samples performed better than the sintered copper sample when mass, which has a significant influence on the cost in space applications, was taken into consideration. The porous structures manufactured by SLM could achieve higher lift heights than the other two types of wicks on per mass basis.

Heat transfer coefficients of the porous structures were measured. The heat transfer coefficient increases with flow rate for all samples. The rate of change became smaller for small unit cell samples because of limited thermal convection due to the low porosity. The heat transfer coefficient did not change proportionally with the unit cell size, or porosity and pore size. There was an optimum porosity and pore size for both CpTi and Ti64 samples to achieve the highest heat transfer coefficient by balancing the thermal conduction in the solid matrix and the heat removal by the fluid.

7.3 Manufacture and Compatibility Test of Heat Pipes

Full-length Ti64 heat pipes with a 350 μm cell size were designed and manufactured using the SLM process. Various tests, including helium leak, charge mass optimisation, proof- and burst-pressure, non-condensable gas and thermal tests, were conducted. The heat pipes successfully passed the criteria set in these tests. Ammonia shows the good compatibility with the Ti64 which means there is no condensable gas generating

during the operation process.

The thermal performance of the heat pipes was not affected by the mechanical tests. An assembly of three heat pipes with an overall transport length of 200 mm was able to dissipate a 30 W output heat load between the 40 mm x 40 mm evaporator and the 40 mm x 40 mm condenser. The functional angle against gravity was -15°.

7.4 Future Work

The heat pipe wick technology developed in this project offers a first-generation technology that has the potential to be developed further to create advanced additively manufactured wick structures. A follow-on development activity is recommended to advance the technology and initiate commercialisation in space applications.

Nowadays, more and more alloys can be used in the SLM manufacturing process. These alloys can overcome the shortcoming of single metal components with enhanced properties in many cases. As mass and high thermal conductivity are the main considerations in space applications of heat pipes, copper-titanium alloys seem to be a good solution. However, further study is necessary to deal with the various problems, for example, low efficiency of SLM using materials with a high reflectivity. . In order to improve the thermal performance of the heat pipe can be improved by using materials with high thermal conductivity, such as aluminium, to replace titanium. Additively manufactured aluminium heat pipes can offer several enhancements over conventional aluminium-ammonia axially grooved heat pipes: functionality against gravity, an increased level of integration into the electronics system, and a higher surface heat flux limit potentially enabling direct thermal management of high heat flux heat sources such as microprocessors.

The current experimental results showed that wall thickness reduction in AM heat pipes is possible. By maintaining the outside diameter, wall thickness reduction will

yield mass reduction and the increased inside diameter/wick volume may yield an increase in transport power and a heat transfer improvement due to increased mass flow rate of condensate. Heat pipes with different combinations of solid wall thickness and wick structure can be tried. More complex shapes can also be developed for specific applications.

Several additional characteristics of porous structures, such as surface roughness, specific surface area and the angle of the strut, may influence the fluid and thermal properties. Further studies are required to investigate their effects.

Chapter 8

Bibliography

AMELI, M., AGNEW, B., LEUNG, P. S., NG, B., SUTCLIFFE, C., SINGH, J. & MCGLEN, R. 2013. A novel method for manufacturing sintered aluminium heat pipes (SAHP). *Applied Thermal Engineering,* 52**,** 498-504.

ANDREAS, E. 2008 Pushing the Boundaries of Heat Pipe Operation. *Electronics Cooling* [Online]. [Accessed 1-11].

ANOVITZ, L. M. & COLE, D. R. 2015. Characterization and analysis of porosity and pore structures. *Reviews in Mineralogy and geochemistry,* 80**,** 61-164.

ARABNEJAD S, BURNETT JOHNSTON R, PURA JA, SINGH B, TANZER M, PASINI D. 2016. High-strength porous biomaterials for bone replacement: a strategy to assess the interplay between cell morphology, mechanical properties, bone ingrowth and manufacturing constraints. *Acta Biomater* 30:345–356.

AYAZ, M., SHAINA, K., CARLOS, T.V., MATTHEW, B. 2019. Capillary Trapping Following Imbibition in Porous Media: Microfluidic Quantification of the Impact of Pore-Scale Surface Roughness, *Water Resources Research*, 55, 9905-9925

BARR, D. W. 2001. Turbulent flow through porous media. *Groundwater,* 39**,** 646-650.

BATCHELOR, G. K. 2000. *An introduction to fluid dynamics*, Cambridge university press.

BEAR, J. 2013. *Dynamics of fluids in porous media*, Courier Corporation.

BELFORTE, G., RAPARELLI, T., VIKTOROV, V. & TRIVELLA, A. 2007. Permeability and inertial coefficients of porous media for air bearing feeding systems. *Journal of Tribology,* 129**,** 705-711.

BOOMSMA, K., POULIKAKOS, D. & ZWICK, F. 2003. Metal foams as compact high performance heat exchangers. *Mechanics of materials,* 35**,** 1161-1176.

BRENNE, F., NIENDORF, T. & MAIER, H. J. 2013. Additively manufactured cellular structures: Impact of microstructure and local strains on the monotonic and cyclic behavior under uniaxial and bending load. *Journal of Materials Processing Technology,* 213**,** 1558-1564.

BRUCE, D., MARCUSDONALD, K. & EDWARDS. 1979. *Graded pore size heat pipe wick*.

BUCKTON, G. & NEWTON, J. 1985. Assessment of the wettability and surface energy of a pharmaceutical powder by liquid penetration. *Journal of pharmacy and pharmacology,* 37**,** 605-609.

BUCKTON, G. & NEWTON, J. 1986. Assessment of the wettability of powders by use of compressed powder discs. *Powder technology,* 46**,** 201-208.

CAO, Y. & FAGHRI, A. 1992. Closed-form analytical solutions of high-temperature heat pipe startup and frozen startup limitation. *Journal of heat transfer,* 114**,** 1028-1035.

CELATA, G. P., CUMO, M. & FURRER, M. 2010. Experimental tests of a stainless steel loop heat pipe with flat evaporator. *Experimental Thermal and Fluid Science,* 34**,** 866-878.

CHALLIS, V. J., XU, X., ZHANG, L. C., ROBERTS, A. P., GROTOWSKI, J. F. & SERCOMBE, T. B. 2014. High specific strength and stiffness structures produced using selective laser melting. *Materials & Design,* 63**,** 783-788.

CHEMISTRY. 2017. *Capillary Action* [Online]. Available: https://chem.libretexts.org/Textbook_Maps/Physical_and_Theoretical_Chemistry_Textbook_Maps/Supplemental_Modules_(Physical_and_Theoretical_Chemistry)/Physical_Properties_of_Matter/States_of_Matter/Properties_of_Liquids/Capillary_Action [Accessed 15-10 2018].

CHEN, S.-W., HSIEH, J.-C., CHOU, C.-T., LIN, H.-H., SHEN, S.-C. & TSAI, M.-J. 2007. Experimental investigation and visualization on capillary and boiling limits of micro-grooves made by different processes. *Sensors and Actuators A: Physical,* 139**,** 78-87.

CHENG, BO, SUBIN SHRESTHA, and KEVIN CHOU. 2010. Stress and deformation evaluations of scanning strategy effect in selective laser melting. *Additive Manufacturing* 12

CHI, S. 1976. Heat pipe theory and practice. *Washington, DC, Hemisphere Publishing Corp.; New York, McGraw-Hill Book Co., 1976. 256 p.*

Choi, JOON-PHIL, et al. 2017. Densification and microstructural investigation of Inconel 718 parts fabricated by selective laser melting. *Powder technology* 310, 60-66.

COSTA, A. 2006. Permeability-porosity relationship: A reexamination of the Kozeny-Carman equation based on a fractal pore-space geometry assumption. *Geophysical research letters,* 33.

CUADRADO A, YANEZ A, MATKEL O, DEVIAENE S, MONOPOLI D. 2017. Influence of load orientation and of types of loads on the mechanical properties of porous Ti6Al4V biomaterials. *Mater Des* 135:309–318.

DAN, J. 2011. *The Characterisation and Biological Assessment of Novel Porous Structures for Orthopaedic Applications.* University of Liverpool.

DANIELS, T. & AL-JUMAILY, F. 1975. Investigations of the factors affecting the performance of a rotating heat pipe. *International Journal of Heat and Mass Transfer,* 18**,** 961-973.

DAS, S. 2003. Physical aspects of process control in selective laser sintering of metals. *Advanced Engineering Materials,* 5**,** 701-711.

DAVIS, P. A., OLAGUE, N. E. & GOODRICH, M. T. 1992. Application of a validation strategy to Darcy's experiment. *Advances in Water Resources,* 15**,** 175-180.

DEMIR, A. G. & PREVITALI, B. 2017. Investigation of remelting and preheating in SLM of 18Ni300 maraging steel as corrective and preventive measures for porosity reduction. *The International Journal of Advanced Manufacturing Technology,* 93**,** 2697-2709.

DING, X. R., LU, L. S., CHEN, C., HE, Z. S. & OU, D. S. Heat transfer enhancement by using four kinds of porous structures in a heat exchanger. Applied Mechanics and Materials, 2011. Trans Tech Publ, 1632-1637.

DOUGHERTY, R. & KUNZELMANN, K. H. 2007. Computing Local Thickness of 3D Structures with ImageJ. *Microscopy and Microanalysis,* 13**,** 1678-1679.

DROBOT, R. *Darcy's law* [Online]. Available: http://echo2.epfl.ch/VICAIRE/mod_3/chapt_5/main.htm [Accessed 08-11 2018].

DULLIEN, F. A. 2012. *Porous media: fluid transport and pore structure,* Academic press.

DUNN, P. D. & REAY, D. 2012. *Heat pipes,* Elsevier.

ECHETA IFEANYICHUKWU, XIAOBING FENG, DUTTON BEN, LEACH RICHARD, PIANO SAMANTA. 2020. Review of defects in lattice structures manufactured by powder bed fusion. *Int J Adv Manuf Technol* 106: 2649.

ELLISON, A. H., KLEMM, R., SCHWARTZ, A. M., GRUBB, L. & PETRASH, D. A. 1967. Contact angles of mercury on various surfaces and the effect of temperature. *Journal of Chemical and Engineering Data,* 12**,** 607-609.

ESHGHINEJADFARD, A., DARÓCZY, L., JANIGA, G. & THÉVENIN, D. 2016. Calculation of the permeability in porous media using the lattice Boltzmann method. *International Journal of Heat and Fluid Flow,* 62**,** 93-103.

EVANS, S., JONES, E., FOX, P. & SUTCLIFFE, C. 2017. Analysis of variability in additive manufactured open cell porous structures. *Proceedings of the Institution of Mechanical Engineers, Part H: Journal of Engineering in Medicine,* 231**,** 534-546.

FAGHRI, A. 1995. *Heat pipe science and technology,* Global Digital Press.

FAGHRI, A. 2012. Review and advances in heat pipe science and technology. *Journal of heat transfer,* 134**,** 123001.

FAGHRI, A. & THOMAS, S. 1989. Performance characteristics of a concentric annular heat pipe: Part I—Experimental prediction and analysis of the capillary limit. *Journal of heat transfer,* 111**,** 844-850.

FORCHHEIMER, P. 1901. Wasserbewegung durch Boden. *Zeitschrift des Vereins Deutscher Ingenieure,* 45**,** 6.

FRAZIER, W. E. 2014. Metal additive manufacturing: a review. *Journal of Materials Engineering and Performance,* 23**,** 1917-1928.

FRIES, N. & QUÉRÉ, D. 2010. *Capillary transport processes in porous materials-experiment and model,* Cuvillier.

GERMAN, R. M. 1996. Sintering theory and practice. *Solar-Terrestrial Physics***,** 568.

GERMAN, R. M., SURI, P. & PARK, S. J. 2009. Review: liquid phase sintering. *Journal of Materials Science,* 44**,** 1-39.

GROLL, M., SCHNEIDER, M., SARTRE, V., ZAGHDOUDI, M. C. & LALLEMAND, M. 1998. Thermal control of electronic equipment by heat pipes. *Revue générale de thermique,* 37**,** 323-352.

GU, D., SHEN, Y. & XIAO, J. 2008. Influence of processing parameters on particulate dispersion in direct laser sintered WC–Cop/Cu MMCs. *International Journal of Refractory Metals and Hard Materials,* 26**,** 411-422.

HEINL, P., MÜLLER, L., KÖRNER, C., SINGER, R. F. & MÜLLER, F. A. 2008. Cellular Ti–6Al–4V structures with interconnected macro porosity for bone implants fabricated by selective electron beam melting. *Acta Biomaterialia,* 4**,** 1536-1544.

HILDEBRAND, T. & RÜEGSEGGER, P. 1997. A New Method for the Model-Independent Assessment of Thickness in Three-Dimensional Images. *Journal of Microscopy,* 185**,** 67-75.

HOWARD, J. J. & KENYON, W. E. 1992. Determination of pore size distribution in sedimentary rocks by proton nuclear magnetic resonance. *Marine and Petroleum Geology,* 9**,** 139-145.

HUANG, Y., LEU, M. C., MAZUMDER, J. & DONMEZ, A. 2015. Additive manufacturing: current state, future potential, gaps and needs, and recommendations. *Journal of Manufacturing Science and Engineering,* 137**,** 014001.

HUL-CHUN, H. 2006. *Wick structure of heat pipe*.

HYUB, L., Lim, C.H.J., Low, M.J. et al. Int. J. of Precis. Eng. and Manuf.-Green Tech. (2017) 4: 307.

IVERSON, B. D., DAVIS, T. W., GARIMELLA, S. V., NORTH, M. T. & KANG, S. S. 2007. Heat and mass transport in heat pipe wick structures. *Journal of Thermophysics and Heat Transfer,* 21**,** 392-404.

JIANG, L.-L., TANG, Y., ZHOU, W., JIANG, L.-Z., XIAO, T., LI, Y. & GAO, J.-W. 2014. Design and fabrication of sintered wick for miniature cylindrical heat pipe. *Transactions of Nonferrous Metals Society of China,* 24**,** 292-301.

JIAO, A. J., MA, H. B. & CRITSER, J. K. 2007. Evaporation heat transfer characteristics of a grooved heat pipe with micro-trapezoidal grooves. *International Journal of Heat and Mass Transfer,* 50**,** 2905-2911.

KALMIKOV, I.V., Capillary action, [online]. Available: http://www.thermopedia.com/content/31/ [Accessed 14-01 2020]

KAVIANY, M. 2012. *Principles of heat transfer in porous media*, Springer Science & Business Media.

KHAYARGOLI, P., LOYA, V., LEFEBVRE, L. & MEDRAJ, M. The impact of microstructure on the permeability of metal foams. CSME forum, 2004. 220-228.

KIM, S., PAEK, J. & KANG, B. 2000. Flow and heat transfer correlations for porous fin in a plate-fin heat exchanger. *Journal of heat transfer,* 122**,** 572-578.

KLOCKE, F. & WIRTZ, H. 1997. Selective laser sintering of ceramics. *LASER ASSISTED NET SHAPE ENGINEERING.* Meisenbach GmbH.

KO, K.-H. & ANAND, N. 2003. Use of porous baffles to enhance heat transfer in a rectangular channel. *International Journal of Heat and Mass Transfer,* 46**,** 4191-4199.

KOCOVIC, P. 2017. *3D Printing and Its Impact on the Production of Fully Functional Components: Emerging Research and Opportunities: Emerging Research and Opportunities*, IGI Global.

KOPONEN, A., KATAJA, M. & TIMONEN, J. 1997. Permeability and effective porosity of porous media. *Physical Review E,* 56**,** 3319.

KOZENY, J. 1927. Uber kapillare leitung der wasser in boden. *Royal Academy of Science, Vienna, Proc. Class I,* 136**,** 271-306.

KRUTH, J.-P., LEVY, G., KLOCKE, F. & CHILDS, T. 2007. Consolidation phenomena in laser and powder-bed based layered manufacturing. *CIRP annals,* 56**,** 730-759.

KRUTH, J.-P., MERCELIS, P., VAN VAERENBERGH, J., FROYEN, L. & ROMBOUTS, M. 2005. Binding mechanisms in selective laser sintering and selective laser melting. *Rapid prototyping journal,* 11**,** 26-36.

KRUTH, J.-P., WANG, X., LAOUI, T. & FROYEN, L. 2003. Lasers and materials in selective laser sintering. *Assembly Automation,* 23**,** 357-371.

KUMAR, A., MAINI, B., BISHNOI, P., CLARKE, M., ZATSEPINA, O. & SRINIVASAN, S. 2010. Experimental determination of permeability in the presence of hydrates and its effect on the dissociation characteristics of gas hydrates in porous media. *Journal of Petroleum Science and Engineering,* 70**,** 114-122.

KURZYNOWSKI, TOMASZ & CHLEBUS, EDWARD & KUZNICKA, BOGUMILA & REINER, JACEK. 2012. Parameters in Selective Laser Melting for processing metallic powders. *Proceedings of SPIE*.

KUSUMA and CHANDRAKANTH. 2016. The Effect of Laser Power and Scan Speed on Melt Pool Characteristics of Pure Titanium and Ti-6Al-4V Alloy for Selective Laser Melting.

LANTHBR, J. E. B. 1892. *Manufacture of contour relief-maps*.

LAOUI, T., BONSE, J., KRUTH, J.-P. & FROYEN, L. Influence of powder parameters on selective laser sintering of tungsten-carbide cobalt. Proceedings of the 7th European Conf. on Rapid Prototyping and Manufacturing, 1998. 271-279.

LAWRENCE, M. & JIANG, Y. 2017. Porosity, pore size distribution, micro-structure. *Bio-aggregates Based Building Materials.* Springer.

LERK, C., LAGAS, M., BOELSTRA, J. & BROERSMA, P. 1977. Contact angles of pharmaceutical powders. *Journal of pharmaceutical sciences,* 66**,** 1480-1481.

LEVY, G. N., SCHINDEL, R. & KRUTH, J.-P. 2003. Rapid manufacturing and rapid tooling with layer manufacturing (LM) technologies, state of the art and future perspectives. *CIRP Annals-Manufacturing Technology,* 52**,** 589-609.

LI, D. & ENGLER, T. W. Literature review on correlations of the non-Darcy coefficient. SPE Permian Basin Oil and Gas Recovery Conference, 2001. Society of Petroleum Engineers.

LI, Y., HE, H.-F. & ZENG, Z.-X. 2013. Evaporation and condensation heat transfer in a heat pipe with a sintered-grooved composite wick. *Applied Thermal Engineering,* 50**,** 342-351.

LIU, P. S., X.M. Ma, Property relations based on the octahedral structure model with body-centered cubic mode for porous metal foams. 2020. *Materials & Design*, 188, 2020, 108413, 0264-1275.

LIU, S.-F., LI, A., REN, Y.-J., LI, D.-F. & ZHANG, Z.-H. 2017. Heat transfer performance of porous titanium. *Journal of Iron and Steel Research, International,* 24**,** 556-560.

LIU, Z., LI, H., CHEN, B., YANG, J. & LIU, W. 2012. Operational characteristics of flat type loop heat pipe with biporous wick. *International Journal of Thermal Sciences,* 58**,** 180-185.

LOUVIS, E. 2012. *Techniques for producing high relative density aluminium alloy components with selective laser melting.* University of Liverpool.

LÜ, L., FUH, J. & WONG, Y.-S. 2013. *Laser-induced materials and processes for rapid prototyping*, Springer Science & Business Media.

LU, X., ZHAO, Y. & DENNIS, D. J. 2018. Flow measurements in microporous media using micro-particle image velocimetry. *Physical Review Fluids,* 3**,** 104202.

MAJUMDAR, JYOTSNA DUTTA, and INDRANIL MANNA. 2012. *Laser-assisted fabrication of materials*. Vol. 161. Springer Science & Business Media.

MANIKANDAN, K. & SENTHILKUMAR, R. 2016. Performance Analysis of Heat Pipe using Different Screen Mesh Sizes. *International Journal of Engineering Trends and Technology (IJETT),* 40.

MARCUS, B. D. 1972. Theory and design of variable conductance heat pipes.

MATSUBARA, K. 1974. Molding Method of Casting Using Photocurable Substance. *Japanese Kokai Patent Application, Sho 51 [1976]-10813*.

Matthews, M, J., Guss, G., Khairallah, S, A., Rubenchik, A, M., Depond, P, J. 2016, Denudation of metal powder layes in laser powder bed fusion processes, Acta Materialia, 114, 33-42.

MAVKO, G. & NUR, A. 1997. The effect of a percolation threshold in the Kozeny-Carman relation. *Geophysics,* 62**,** 1480-1482.

MAZUMDER, J., DUTTA, D., KIKUCHI, N., & GHOSH, A. 2000. Closed loop direct metal deposition: Art to part. *Optics and Lasers in Engineering*, 34(4-6), 397- 414.

MERCELIS, P. & KRUTH, J.-P. 2006. Residual stresses in selective laser sintering and selective laser melting. *Rapid prototyping journal,* 12**,** 254-265.

MICHAEL, R. K., ALEXANDER R, F., ROBERT T, H. & HILLARD R, H. 1991. *Graded-groove heat pipe*.

MOHAMMED, R. A., C, R. H. T., SYED, M. S. S. & C, Y. 2015. A Review on Diverse Materials Applied For Additive Manufacturing. *International Journal for Research in Applied Science & Engineering*

MULLEN, L., STAMP, R. C., BROOKS, W. K., JONES, E. & SUTCLIFFE, C. J. 2009a. Selective Laser Melting: A regular unit cell approach for the manufacture of porous, titanium, bone in-growth constructs, suitable for orthopedic applications. *Journal of Biomedical Materials Research Part B: Applied Biomaterials,* 89**,** 325-334.

MULLEN, L., STAMP, R. C., BROOKS, W. K., JONES, E. & SUTCLIFFE, C. J. 2009b. Selective Laser Melting: A regular unit cell approach for the manufacture of porous, titanium, bone in-growth constructs, suitable for orthopedic applications. *Journal of Biomedical Materials Research Part B: Applied Biomaterials: An Official Journal of The Society for Biomaterials, The Japanese Society for Biomaterials, and The Australian Society for Biomaterials and the Korean Society for Biomaterials,* 89**,** 325-334.

MWABA, M. G., HUANG, X. & GU, J. 2006. Influence of wick characteristics on heat pipe performance. *International journal of energy research,* 30**,** 489-499.

NEMEC, P. 2018. Gravity in Heat Pipe Technology. *Gravity-Geoscience Applications, Industrial Technology and Quantum Aspect.* InTech.

NEMEC, P., CAJA, A. & MALCHO, M. 2011. Thermal performance measurement of heat pipe. *Global journal of technology and optimization,* 2.

NEMEC, P., ČAJA, A. & MALCHO, M. 2013. Mathematical model for heat transfer limitations of heat pipe. *Mathematical and Computer Modelling,* 57**,** 126-136.

NEUTRIUM. 2012. *HYDRAULIC DIAMETER* [Online]. Available: https://neutrium.net/fluid_flow/hydraulic-diameter/ [Accessed 17-09 2018].

NGUYEN, Q. B., et al. 2018. The role of powder layer thickness on the quality of SLM printed parts. *Archives of Civil and Mechanical Engineering* 18.3: 948-955.

NISHIKAWARA, M. & NAGANO, H. 2014. Parametric experiments on a miniature loop heat pipe with PTFE wicks. *International Journal of Thermal Sciences,* 85**,** 29-39.

NOIE-BAGHBAN, S. H. & MAJIDEIAN, G. 2000. Waste heat recovery using heat pipe heat exchanger (HPHE) for surgery rooms in hospitals. *Applied thermal engineering,* 20**,** 1271-1282.

OLAKANMI, E., COCHRANE, R. & DALGARNO, K. Spheroidisation and oxide disruption phenomena in direct Selective Laser Melting (SLM) of pre-alloyed Al-Mg and Al-Si powders. Proceedings: TMS Annual Meetings and Exhibition, 2009. 371-380.

PALERMO, E. 2013. *What is Selective Laser Sintering?* [Online]. Available: https://www.livescience.com/38862-selective-laser-sintering.html [Accessed 17-09 2018].

PANNETON, R. & GROS, E. 2005. A missing mass method to measure the open porosity of porous solids. *ACTA Acustica united with Acustica,* 91**,** 342-348.

PRASHANTH and KONDA GOLILDOSS. 2014. Selective laser melting of Al-12Si.

PUJADO, P., HUH, C. & SCRIVEN, L. 1972. On the Attribution of an Equation of Capillarity to Young and Laplace. *Journal of Colloid and Interface Science,* 38**,** 662-663.

REAY, D. 1981. A review of gas-gas heat recovery systems. *Journal of Heat Recovery Systems,* 1**,** 3-41.

REAY, D., MCGLEN, R. & KEW, P. 2013. *Heat pipes: Theory, design and applications,* Butterworth-Heinemann.

REN, C., WU, Q.-S. & HU, M.-B. 2007. Heat transfer in loop heat pipe's wick: Effect of porous structure parameters. *Journal of Thermophysics and Heat Transfer,* 21**,** 702-711.

RIDGWAY, C. J., SCHOELKOPF, J. & GANE, P. A. 2003. A new method for measuring the liquid permeability of coated and uncoated papers and boards. *Nordic Pulp & Paper Research Journal,* 18**,** 377-381.

RIEHL, R. R. & DOS SANTOS, N. 2008. Loop heat pipe performance enhancement using primary wick with circumferential grooves. *Applied Thermal Engineering,* 28**,** 1745-1755.

SALISSOU, Y. & PANNETON, R. 2007. Pressure/mass method to measure open porosity of porous solids. *Journal of applied physics,* 101**,** 124913.

SCHLEIFENBAUM, H., MEINERS, W., WISSENBACH, K. & HINKE, C. 2010. Individualized production by means of high power Selective Laser Melting. *CIRP Journal of manufacturing science and technology,* 2**,** 161-169.

SEIDENBERG, B. & SWANSON, T. D. 1989. Ceramic heat pipe wick. Google Patents.
SHIN, C. 2017. Tortuosity correction of Kozeny's hydraulic diameter of a porous medium. *Physics of Fluids,* 29**,** 023104.

SINGH, R., AKBARZADEH, A. & MOCHIZUKI, M. 2009. Effect of wick characteristics on the thermal performance of the miniature loop heat pipe. *Journal of Heat transfer,* 131**,** 082601.

SINGH, R., MOCHIZUKI, M., MASHIKO, K. & NGUYEN, T. 2011. Heat pipe based cold energy storage systems for datacenter energy conservation. *Energy,* 36**,** 2802-2811.

SPEDDING, T. A. & WANG, Z. Q. 1997. Study on modeling of wire EDM process. *Journal of Materials Processing Technology,* 69**,** 18-28.

STAMP, R., FOX, P., O'NEILL, W., JONES, E. & SUTCLIFFE, C. 2009. The development of a scanning strategy for the manufacture of porous biomaterials by selective laser melting. *Journal of Materials Science: Materials in Medicine,* 20**,** 1839.

STAVER, C. 2015. *Grooved Wick Structures* [Online]. Available: https://www.columbia-staver.co.uk/technologies/heat-pipes/grooved-wick-structures/ [Accessed 01-09 2018].

SUN, S., Brandt, M., Easton, M. 2017. 2 - Powder bed fusion processes: An overview, L*aser Additive Manufacturing*, Woodhead Publishing, 55-77.

TANG, Y., DENG, D., LU, L., PAN, M. & WANG, Q. 2010. Experimental investigation on capillary force of composite wick structure by IR thermal imaging camera. *Experimental Thermal and Fluid Science,* 34**,** 190-196.

THANKI, ADITI, et al. 2019. Study of keyhole-porosities in selective laser melting using X-ray computed tomography. *Proceedings of iCT 2019.*

THIJS, L., KEMPEN, K., KRUTH, J.-P. & VAN HUMBEECK, J. 2013. Fine-structured aluminium products with controllable texture by selective laser melting of pre-alloyed AlSi10Mg powder. *Acta Materialia,* 61**,** 1809-1819.

THIJS, L., VERHAEGHE, F., CRAEGHS, T., VAN HUMBEECK, J. & KRUTH, J.-P. 2010. A study of the microstructural evolution during selective laser melting of Ti–6Al–4V. *Acta materialia,* 58**,** 3303-3312.

THOMPSON, S. M., ASPIN, Z. S., SHAMSAEI, N., ELWANY, A. & BIAN, L. 2015. Additive manufacturing of heat exchangers: A case study on a multi-layered Ti–6Al–4V oscillating heat pipe. *Additive Manufacturing,* 8**,** 163-174.

TOLOCHKO, N. K., ARSHINOV, M. K., GUSAROV, A. V., TITOV, V. I., LAOUI, T. & FROYEN, L. 2003. Mechanisms of selective laser sintering and heat transfer in Ti powder. *Rapid prototyping journal,* 9**,** 314-326.

TOLOCHKO, N. K., KHLOPKOV, Y. V., MOZZHAROV, S. E., IGNATIEV, M. B., LAOUI, T. & TITOV, V. I. 2000. Absorptance of powder materials suitable for laser sintering. *Rapid Prototyping Journal,* 6**,** 155-161.

UDELL, K. S. 1985. Heat transfer in porous media considering phase change and capillarity—the heat pipe effect. *International Journal of Heat and Mass Transfer,* 28**,** 485-495.

VAN NGUYEN, C., SISTLA, S. K., VAN KEMPEN, S., GIANG, N. A., BEZOLD, A., BROECKMANN, C. & LANGE, F. 2016. A comparative study of different sintering models for Al2O3. *Journal of the Ceramic Society of Japan,* 124**,** 301-312.

VASILIEV, L. 2008. Heat pipes in fuel cell technology. *Mini-Micro Fuel Cells.* Springer.

VIDAL, C. & COOPER, J. 1969. Heat Pipe Oven: A New, Well Defined Metal Vapor Device for Spectroscopic Measurements. *Journal of Applied Physics,* 40**,** 3370-3374.

VINCENT, K. K., MUTHAMA, M. N. & MUOKI, S. N. 2014. Darcy¡ s Law Equation with Application to Underground Seepage in Earth Dams in Calculation of the Amount of Seepage. *American Journal of Applied Mathematics and Statistics,* 2**,** 143-149.

WANG, DI, YONGQIANG YANG, RUICHENG LIU, DONGMING XIAO, JIANFENG SUN. 2013. Study on the designing rules and processability of porous structure based on selective laser melting (SLM), *Journal of Materials Processing Technology,* 213, 10, 1734-1742.

WANG, X., LAOUI, T., BONSE, J., KRUTH, J.-P., LAUWERS, B. & FROYEN, L. 2002. Direct selective laser sintering of hard metal powders: experimental study and simulation. *The International Journal of Advanced Manufacturing Technology,* 19**,** 351-357.

WEN-CHEN, W. 2003. *Flexible heat pipe*.

WOHLERS, T. & GORNET, T. 2014. History of additive manufacturing. *Wohlers report,* 24**,** 118.

YADROITSEV, I., et al. 2010. Single track formation in selective laser melting of metal powders. *Journal of Materials Processing Technology* 210.12: 1624-1631.

YANG, B.-H., WU, A.-X., MIAO, X.-X. & LIU, J.-Z. 2014. 3D characterization and analysis of pore structure of packed ore particle beds based on computed tomography images. *Transactions of Nonferrous Metals Society of China,* 24**,** 833-838.

YASA, E., DECKERS, J. & KRUTH, J.-P. 2011. The investigation of the influence of laser re-melting on density, surface quality and microstructure of selective laser melting parts. *Rapid Prototyping Journal,* 17**,** 312-327.

YASA, E. & KRUTH, J.-P. 2011. Application of laser re-melting on selective laser melting parts. *Advances in Production engineering and Management,* 6**,** 259-270.

YUAN, Y. & LEE, T. R. 2013. Contact angle and wetting properties. *Surface science techniques.* Springer.

ZENG, Z. & GRIGG, R. 2006. A criterion for non-Darcy flow in porous media. *Transport in porous media,* 63**,** 57-69.

ZHANG, L., MULLEN, D., LYNN, K. & ZHAO, Y. 2009. Heat Transfer Performance of Porous Copper Fabricated by Lost Carbonate Sintering Process. *MRS Online Proceedings Library Archive,* 1188.

ZHU, H., FUH, J., & Lu, L. 2007. The influence of powder apparent density on the density in direct laser-sintered metallic parts. *International Journal of Machine Tools and Manufacture*, 47(2), 294-298.

ZOGRAFI, G. & TAM, S. S. 1976. Wettability of pharmaceutical solids: estimates of solid surface polarity. *Journal of pharmaceutical sciences,* 65**,** 1145-1149.

ZOHURI, B. 2016. Other Types of Heat Pipes. *Heat Pipe Design and Technology.* Springer.

ZUO, L., KREVOR, S., FALTA, R. W. & BENSON, S. M. 2012. An experimental study of CO2 exsolution and relative permeability measurements during CO2 saturated water depressurization. *Transport in porous media,* 91**,** 459-478.

ZUO, Z. J., NORTH, M. T. & WERT, K. L. 2001. High heat flux heat pipe mechanism for cooling of electronics. *IEEE Transactions on Components and Packaging Technologies,* 24**,** 220-225.